INFORMATION TO USERS

This manuscript has been reproduced from the microfilm master. UMI films the text directly from the original or copy submitted. Thus, some thesis and dissertation copies are in typewriter face, while others may be from any type of computer printer.

The quality of this reproduction is dependent upon the quality of the copy submitted. Broken or indistinct print, colored or poor quality illustrations and photographs, print bleedthrough, substandard margins, and improper alignment can adversely affect reproduction.

In the unlikely event that the author did not send UMI a complete manuscript and there are missing pages, these will be noted. Also, if unauthorized copyright material had to be removed, a note will indicate the deletion.

Oversize materials (e.g., maps, drawings, charts) are reproduced by sectioning the original, beginning at the upper left-hand corner and continuing from left to right in equal sections with small overlaps. Each original is also photographed in one exposure and is included in reduced form at the back of the book.

Photographs included in the original manuscript have been reproduced xerographically in this copy. Higher quality 6" x 9" black and white photographic prints are available for any photographs or illustrations appearing in this copy for an additional charge. Contact UMI directly to order.

UMI

A Bell & Howell Information Company
300 North Zeeb Road, Ann Arbor MI 48106-1346 USA
313/761-4700 800/521-0600

Development of Line-Imaging Raman Spectroscopy for use with Electrochemical Systems

by

Scott Michael Haight

A dissertation submitted in partial fulfillment of the
requirements for the degree of

Doctor of Philosophy

University of Washington

1997

Approved by Daniel T Schwartz

Chairperson of Supervisory Committee

Program Authorized
to Offer Degree CHEMICAL ENGINEERING

Date MARCH 14, 1997

In presenting this dissertation in partial fulfillment of the requirements for the Doctoral degree at the University of Washington, I agree that the Library shall make its copies freely available for inspection. I further agree that extensive copying of this dissertation is allowable only for scholarly purposes, consistent with "fair use" as prescribed in the U.S. Copyright Law. Requests for copying or reproduction of this dissertation may be referred to University Microfilms, 1490 Eisenhower Place, P.O. Box 975, Ann Arbor, MI 48106, to whom the author has granted "the right to reproduce and sell (a) copies of the manuscript in microform and/or (b) printed copies of the manuscript made from microform."

Signature Scott Haight

Date 3/14/97

University of Washington

Abstract

Development of Line-Imaging Raman Spectroscopy for use with Electrochemical Systems

by Scott Michael Haight

Chairperson of the Supervisory Committee: Associate Professor Daniel T. Schwartz

Department of Chemical Engineering

This work presents the construction and application of a line-imaging Raman spectroscopy instrument for use with electrochemical systems. Line-imaging spectroscopy is able to collect spatially resolved spectra along a contiguous imaging line. Specifically studied was an electrodeposited thin film of CuSCN for possible use in solar cell applications, copper plating as a model electrodeposition system, and nickel hexacyanoferrate derivatized electrodes for possible applications as an electrically controlled cation exchange material. Both solution phase and surface imaging studies were performed. For solution studies, line-imaging Raman spectroscopy was used to simultaneously probe solution and surface chemistry of a thin film of electrodeposited CuSCN. It is shown that the instrument is able to spectrally and spatially identify CuSCN on a wire electrode surface, and $Cu(SCN)^+$ species in solution. Images were collected with 5 μm spatial resolution and 8 cm^{-1} spectral slitwidth under the experimental conditions used. The ability to directly image concentration boundary layers during plating is also shown using a copper electrodeposition system. The concentration boundary layer resulting from deposition on a wire electrode was directly imaged *in situ* at several

deposition rates. It is shown that the concentration boundary layer thickness increases, and the surface concentration decreases with deposition rate, as expected. Concentration boundary layer thicknesses of less than 100 μm were reproducibly resolved.

In situ Raman line-images acquired along the surface of nickel hexacyanoferrate derivatized electrodes were used to probe the oxidation and reduction of the thin (ca. 80 nm) surface film. The CN Raman modes of this material are sensitive to oxidation state of the iron-centers in the lattice. A multivariate principle component regression model was developed that predicts the oxidation state in the film lattice based on spectral features in the line-images. The combination of line-imaging Raman spectroscopy and multivariate modeling was used to produce spatial profiles of oxidation state in the film with 5 μm resolution. Repeated redox cycling of the derivatized surface is shown to cause a loss in the ability of iron centers in the lattice to reversibly switch between Fe^{II} and Fe^{III}, causing the derivatized layer to lose ion exchange capacity. Moreover, the oxidation state of the derivatized electrodes was found to switch nonuniformly across the surface as potential was modulated. As the redox activity of the derivatized electrodes declines, the nickel hexacyanoferrate ultimately reaches a spatially uniform mixed valence state with Fe^{II}:Fe^{III} in a ratio of 4:1. The photoresponse of nickel hexacyanoferrate to 647.1 nm illumination was found to complicate the interpretation of Raman line-images.

TABLE OF CONTENTS

LIST OF FIGURES

LIST OF TABLES

ACKNOWLEDGMENTS

I would like to express my appreciation to Dan Schwartz, my advisor and friend for over four years. His constant energy and insistence on a high standard of work has challenged and educated me. I thank him for providing me with the opportunity to work in his group. I would also like to thank my committee members for their time, thoughts, and general support.

This acknowledgment would not be complete without mentioning the many friends and colleagues with whom I have shared a great deal of time personally and professionally. I would especially like to mention my good friend and former group member, Antonio Medina, and acknowledge my incoming classmates. My most sincere acknowledgment, however, goes to Kari. I am truly lucky to have such a wonderful person as my wife.

Finally, I would like to acknowledge the Intel Foundation for providing fellowship support during 1995, the Drowley Fellowship for support during 1992, and the Electrochemical Society for the Abner Brenner travel grant in 1995.

CHAPTER 1: INTRODUCTION

As the demand for high performance electronic displays, precision optics, integrated circuits, and energy storage, conversion, and delivery systems grows, the need to precisely control the properties of the underlying materials and structures grows ever greater. Increasingly this necessitates simultaneously considering not only lengthscales from meters to sub-nanometers, but also the relationship between structure and properties of the underlying material. Because thin films can exhibit precisely engineered optical, magnetic, and mechanical properties, they are being used more and more to meet society's performance demands.

Whether used as a homogeneous surface coating for optics, or multiple layers in an electronic or magnetic device, thin films are normally formed by deposition onto a substrate. For electrochemically deposited films, the subject of this dissertation, the substrate generally is an electrode, and reactions that lead to film formation occur at the surface or in the concentration boundary layer near the surface. A film may be formed by a heterogeneous reaction, where electrons from the electrode react directly with solution species within Ångstroms of the surface. Alternatively, electrons from the electrode may only generate an intermediate species which then reacts homogeneously in solution to form the final material.

Due to the coupling between the boundary layer and the final film, we are motivated to achieve a better understanding of chemical interactions that occur at or very near electrode surfaces. A traditional approach for understanding electrochemical systems measures the average response of the electrochemical system such as the current/potential and bulk species concentrations, and relates these measurements to the final film character or properties. In some cases these average-property probes sometimes provide mechanistic insight into the deposition process. However, these average measures have a much more difficult time providing definitive insight into deposition systems where the important

chemistry occurs in a boundary layer with electrode-generated intermediates.[1,2] Here the identification and quantification of species that exist within approximately 100 μm of the growing film may provide key insight into the deposition process and result in improved processing-property relationships.

New tools and methods must be developed to *simultaneously* probe molecular processes occurring over macroscopic lengthscales in order to provide greater insight into processes occurring at or near interfaces.

1.1 Some electrodeposition systems involving coupled homogeneous-heterogeneous chemistry

1.1.1 Metal hexacyanoferrate derivatized surfaces

Metal hexacyanoferrate derivatized surfaces are useful materials because they have the ability to reside in one or more oxidation states. Compounds such as Prussian Blue (iron hexacyanoferrate), and its nickel and cobalt analogs have electrochemically reversible iron-centers, which can be switched between the ferrous and ferric oxidation states *via* an applied potential. When a conductive substrate is derivatized with a metal hexacyanoferrate to form a thin film, the film's oxidation state can be directly controlled and therefore the material properties can be controlled as well.

There are a number of possible technological applications for electrochemically switched metal hexacyanoferrate compounds. Prussian Blue is electrochromic and has been demonstrated as suitable for display devices.[3] Recently, cobalt hexacyanoferrate has been shown to be a molecular magnet with properties that can be modulated by illumination with red and blue light,[4,5] suggesting possible applications in magneto-optical data storage devices. Nickel hexacyanoferrate compounds have an affinity for the intercalation of Cs^+

over all other group 1A cations, suggesting possible applications as an ion exchange material.[6] This last property may prove to be important for removing radioactive $^{137}Cs^{+}$ from sodium-containing tank and basin wastes at sites such as the Department of Energy's Hanford Nuclear Reservation in Richland, Washington.

Figure 1.1 shows schematically the deposition of a thin film of nickel hexacyanoferrate. Generally a deposition bath is prepared from sodium or potassium hexacyanoferrate salt (≈5 mM) with additional sodium or potassium nitrate added (≈100 mM). The reactive bulk species are shown at the top of the figure. A^{+} represents the counterion (Na^{+} or K^{+}), and the dashed line represents the concentration boundary layer thickness. Typically concentration boundary layers are ≤100 μm, depending upon the mixing strength and the rate of homogeneous reaction.

The first step in the surface derivatization is an electrochemical step where a nickel atom is oxidized from the electrode surface into the surrounding solution according to

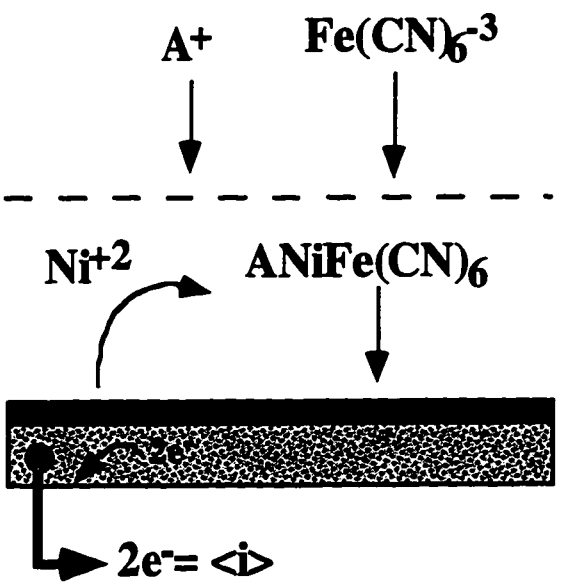

Figure 1.1. Surface derivatization by nickel hexacyanoferrate. A denotes a cation, and the dashed line represents the concentration boundary layer thickness.

eq. 1.1.

$$Ni \rightarrow Ni^{+2} + 2e^{-} \qquad (1.1)$$

This heterogeneous charge transfer reaction is followed by a homogeneous chemical step in solution shown in eq. 1.2.

$$Ni^{+2} + A^{+} + Fe(CN)_6^{-3} \rightarrow ANiFe(CN)_6 \qquad (1.2)$$

Due to this homogeneous reaction in the boundary layer, stirring or agitation causes a marked decrease in film formation rate.[7] The nickel hexacyanoferrate product is insoluble and precipitates back onto the electrode surface, derivatizing it. The precipitate has been shown to be chemisorbed to the surface, rather than held by mechanical or electrostatic forces.[8,9] As the surface is increasingly derivatized, the oxidation of nickel cations is hindered, and the derivatization stops.

Traditional spectroscopic and electrochemical methods have been applied to understand the chemistry of nickel hexacyanoferrate films. For example, optical absorption spectroscopy has been used to study the deposition solution,[9] and diffuse reflection FTIR and photoacoustic spectroscopies[10,11] and electrochemical methods[7,10,12] have been used to study the nature of the film.

Since the mechanism for the formation of hexacyanoferrate films involves the intimate coupling of a growing film on the electrode surface and reaction happening within the electrochemical boundary layer, both regions must be sampled for a full understanding of the derivatization step. A technique is desired that is able to *simultaneously* probe chemical information across this macroscopic distance.

Once deposited on the electrode, nickel hexacyanoferrate can be used as an electrically controlled ion separation material. When the iron-centers in the film are reduced, cations from the surrounding solution are intercalated into the lattice. Upon oxidation the cations are expelled from the film. This reversible electrochemical modulation proceeds according to the reaction given by eq. (1.3),

$$A_{2-x}Ni^{II}Fe^{II+x}(CN)_6 + xA^+ + xe^- \rightleftharpoons A_2Ni^{II}Fe^{II}(CN)_6, \qquad (1.3)$$

where A denotes a cation and x is the fractional oxidation state of the nickel hexacyanoferrate ($0 \leq x \leq 1$).

Figure 1.2 shows the cubic structure of nickel hexacyanoferrate during the reduction of the lattice.[12] Ni and Fe atoms form the corners, CN groups bridge them with Ni being exclusively bound to N, and Fe being bound to C. The cage-like structure has an internal site of radius 0.180 nm and a face-centered bottleneck of radius 0.077 nm. When solvating water molecules are included, Cs^+ has the smallest ionic radius of the group 1A metals, which has been used to describe the selective adsorption characteristics for Cs^+.

To a great degree, the use of metal hexacyanoferrates rests on the stability of these materials over many redox cycles. Previous work has studied several factors affecting the

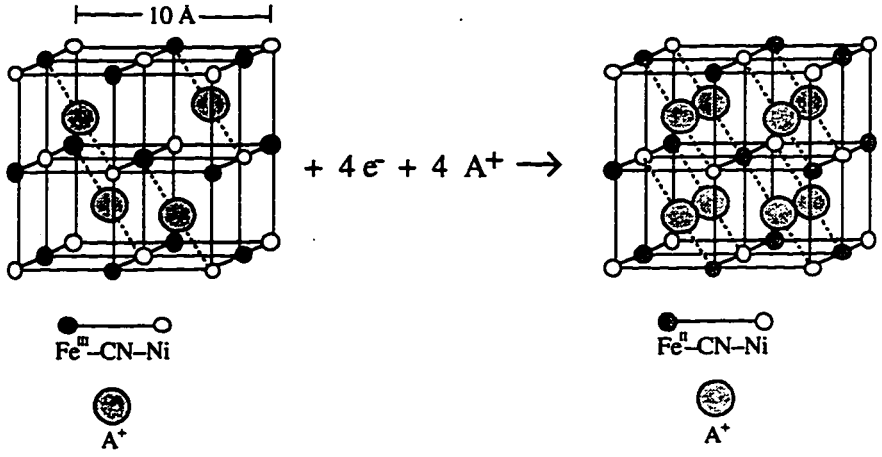

Figure 1.2. Electrically controlled ion exchange with nickel hexacyanoferrate.

cycle-decay and response of Prussian Blue films for use as display devices, including pH and film deposition protocol.[13,14] It was found that Prussian Blue films are much more stable in acidic environments than in neutral baths over many redox cycles, and that Prussian Blue films can be susceptible to inhomogeneous response as indicated by local film regions that do not respond to an applied potential (i.e. regions that do not electrochromically modulate). Precise knowledge of the degree of chemical homogeneity and the uniformity of oxidation state modulation is important for understanding the behavior of these films as ion exchange materials.

Relatively little work has appeared concerning the decay of nickel hexacyanoferrate as an ion exchange material. Although the cation exchange properties and general stability have been demonstrated,[8,9] more work is needed for the direct identification of the mode(s) of decay. Ion capacity may decrease due to physical film loss, (i.e. sloughing or dissolution of the film). Capacity loss may also be due to hindrances in ion or electron transport, preventing regions of the film from being fully accessed (i.e. redox activity loss).

Having a spectroscopic tool able to probe the molecular properties of the nickel hexacyanoferrate thin film over macroscopic lengthscales would provide tremendous new insights into the cycle life degradation of the film. Thus, developing an imaging spectroscopy would shed new light into the deposition of these materials, as well as properties of the deposit. For commercial applications to be realized, the relationship of the processing parameters during film formation to the final surface morphology, stability, cation-exchange ability, and other properties must be thoroughly studied.

1.1.2 Dye-sensitized heterojunctions

Another area that may benefit from a precise understanding of the spatial variation of chemical information near an electrode surface is in the fabrication of dye-sensitized heterojunctions. These junctions have shown promise in possible solar cell applications.[15,16] These devices are multilayered materials, where the dye-sensitized layer collects photons, one adjoining layer accepts electrons (n-type semiconductor), and the other accepts electron vacancies or holes (p-type semiconductor). One particular combination of semiconducting materials currently under investigation is TiO_2 (n-type) and CuSCN (p-type).[15,16] The TiO_2 layer is deposited by organo-metallic chemical vapor deposition (OMCVD) followed by the dye-layer, and then CuSCN. Figure 1.3 shows this structure schematically. The dye-layer is generally temperature sensitive, which can be degraded by temperatures usually found in CVD processes, requiring that the deposition of the subsequent CuSCN layer be performed at moderate temperatures. In addition, this outer layer must be optically transparent, and the deposition must yield a reproducible phase. Electrodeposition meets these fabrication constraints. In the specific case of CuSCN deposition, the deposition of this layer takes place through a homogeneous chemical step followed by a heterogeneous electrochemical step. It is believed that cupric cations (Cu^{+2}) first combine with thiocyanate anions (SCN^-) to form the intermediate

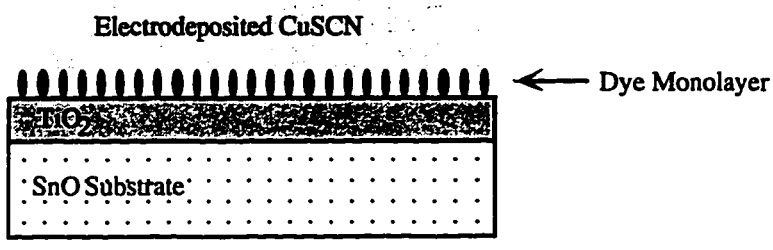

Figure 1.3. Structure of a dye-sensitized heterojunction.

($CuSCN^+$), which is then reduced at the surface to form the deposited layer. Again, since the nature of the deposit crucially affects the device performance, precise knowledge of the electrodeposition process and the effect on processing parameters in the region very near the surface is desired.

1.1.3 NiFe anomalous codeposition

A well known example of the intimate coupling between the boundary layer and the deposited thin film is the anomalous codeposition of nickel-iron alloys, which are used extensively in the magnetic recording industry.[2] Anomalous codeposition is the phenomenon where the less noble of two metals deposits at a faster rate than if it were depositing by itself.[17] When nickel and iron are codeposited, the resulting film contains much more iron than is predicted using individual deposition rates.

Figure 1.4 shows schematically a proposed mechanism for this metal deposition, where Me^+ denotes a metal cation. At sufficiently high deposition overpotentials, hydrogen evolution accompanies metal deposition. This causes a local pH rise in the vicinity of the electrode surface shifting the deposition mechanism. Metal cations are thought to react with the hydroxide ions and form intermediate metal hydroxide cations. It is these intermediate species found within $\approx$100 μm of the surface, that react with the surface to ultimately form the deposited film. To date however, there is no direct evidence to confirm or deny the existence of these intermediate species. A tool that is able to *simultaneously* probe from the bulk solution, through the boundary layer, and the deposited film with chemical specificity would provide valuable insight into this important deposition mechanism.

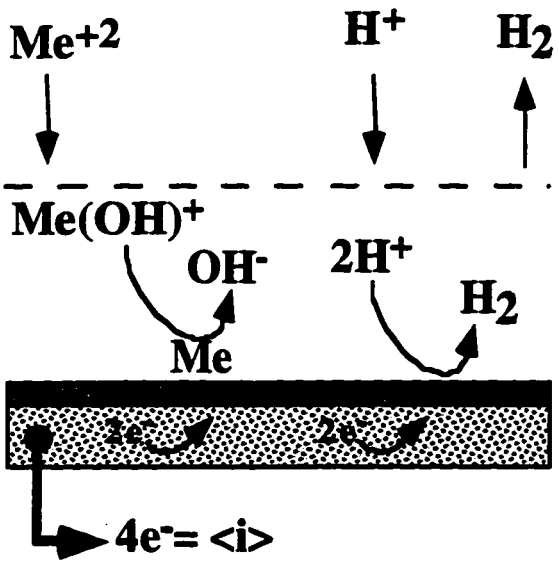

Figure 1.4. A proposed mechanism for anomalous metal codeposition.

1.2 Current techniques for studying electrochemical boundary layers and surfaces

In the aforementioned and other electrochemical systems it is desired to develop a precise understanding of the relationship between processing variables and the resulting properties of the electrochemical system. Generally it is difficult due to probe important interactions occurring near the electrode surfaces and relate those interactions with the properties of the electrode surface or depositing film. In recent years a number of new *in situ* experimental techniques have been developed that are well-suited for probing various aspects of processing/property relationships in electrodeposition and anodization. For example, scanning probe microscopies[18] and X-ray-based techniques[19] have emerged as outstanding tools for understanding the atomic/molecular processes associated with nucleation on surfaces, and ellipsometry is a proven *in situ* tool for probing the growth and merging of nuclei.[20] Once the film has grown to a few nanometers (i.e., bulk film growth),

one finds experimental tools that probe either the nature of the deposited film (e.g. ellipsometry, [21] Raman spectroscopy[22,23]) or the concentration boundary layer region that forms near the surface during the deposition (e.g. interferometry,[24] UV-Vis absorption spectroscopy,[25] luminescence techniques[26,27]).

For the case of bulk film growth, tools are needed to measure both the film properties and the concentration boundary layer because there is often a coupling between the two regions. In fact, it is during bulk film growth where processing parameters like electrolyte agitation often take on their greatest importance. However, to the best of our knowledge, there are presently no experimental techniques available that can *simultaneously* probe the solution chemistry within tens of microns from the electrode surface and the properties of the growing thin film, and do so with molecular-specificity. Similarly, measuring molecular properties along a deposit is also needed to understand how the use of the thin film affects its performance and ultimate degradation (*e.g.* nickel hexacyanoferrate).

1.3 Present Work

The work presented in this dissertation includes the design, characterization and use of a line-imaging Raman spectroscopy instrument for use in electrochemical systems. This spectroelectrochemical imaging system is able to collect chemically specific information over appropriate macroscopic lengthscales. The instrument's ability to directly image electrochemical systems in a way that *simultaneously* probes bulk, boundary layer, and surface regions is demonstrated by identifying surface and solution species in reactive and nonreactive systems. It is also shown that line-imaging Raman in conjunction with multivariate models can be used as an *in situ* surface profiling tool. Since the usefulness of

the images is directly tied to image quality, several important image processing techniques appropriate to Raman line-images are also discussed.

Chapter 2 discusses the concept and previous uses of line-imaging Raman spectroscopy, as well as the construction of the instrument used for this dissertation work. Line-imaging spectroscopy is explained and compared to traditional point spectroscopy, followed by a review of the engineering systems this technique has been applied to in the past. Chapter 3 focuses on the characterization of the instrument with simple electrochemical systems. The electrodeposition of CuSCN is used to assess the instrument's imaging capability, and the ability to directly image concentration boundary layers during electrodeposition is shown with a simple copper system. Chapter 4 addresses the necessity of routine automated image background removal. It is shown that image usefulness is greatly improved by the removal of the image's background signal, but that traditional techniques may not be appropriate, or properly correct Raman line-images. An automated routine for this purpose is described here. Chapters 5 and 6 demonstrate how line-imaging Raman can be used as a surface profiling tool. Chapter 5 addresses the use of multivariate models coupled with line-imaging Raman to probe the oxidation state of nickel hexacyanoferrate thin films *in situ*. Chapter 6 uses this combination to investigate the cycle life decay of these multivalent films over many reduction-oxidation cycles. Chapter 7 gives some concluding remarks and suggestions for future direction based on the results obtained in this work.

CHAPTER 2: LINE-IMAGING RAMAN SPECTROSCOPY AND RECENT DEVELOPMENTS OF THE TECHNIQUE

2.1 Chapter Overview

In this chapter line-imaging is first explained by comparing the technique to a traditional point spectroscopy. This is followed by a discussion of the progression of spectroscopic line-imaging hardware, and of the types of physical systems that have been previously studied. The application of line-imaging Raman spectroscopy to electrochemistry is addressed, and the hardware and software aspects of the instrumentation used in this dissertation are presented.

2.2 Line-Imaging Raman Spectroscopy

Figure 2.1 compares a traditional (point) spectroscopy, to line-imaging spectroscopy. Line-imaging spectroscopy differs from traditional, or point, spectroscopies in that a dimension of spatial information is collected simultaneously with spectroscopic information. In a traditional spectroscopy, an excitation beam is focused to a point on a sample. The scattered light at that point is collected and spectrally dispersed into a single spectrum. If information from another sample location is desired, either the sample or focused excitation beam must be translated. Spectra may be collected at several points in order to discern changes as a function of distance. Although this method yields chemical information over some distance, it is hindered by the ability to accurately translate the sample and/or excitation beam, and also the ability to exactly duplicate experimental conditions from one point to the next.

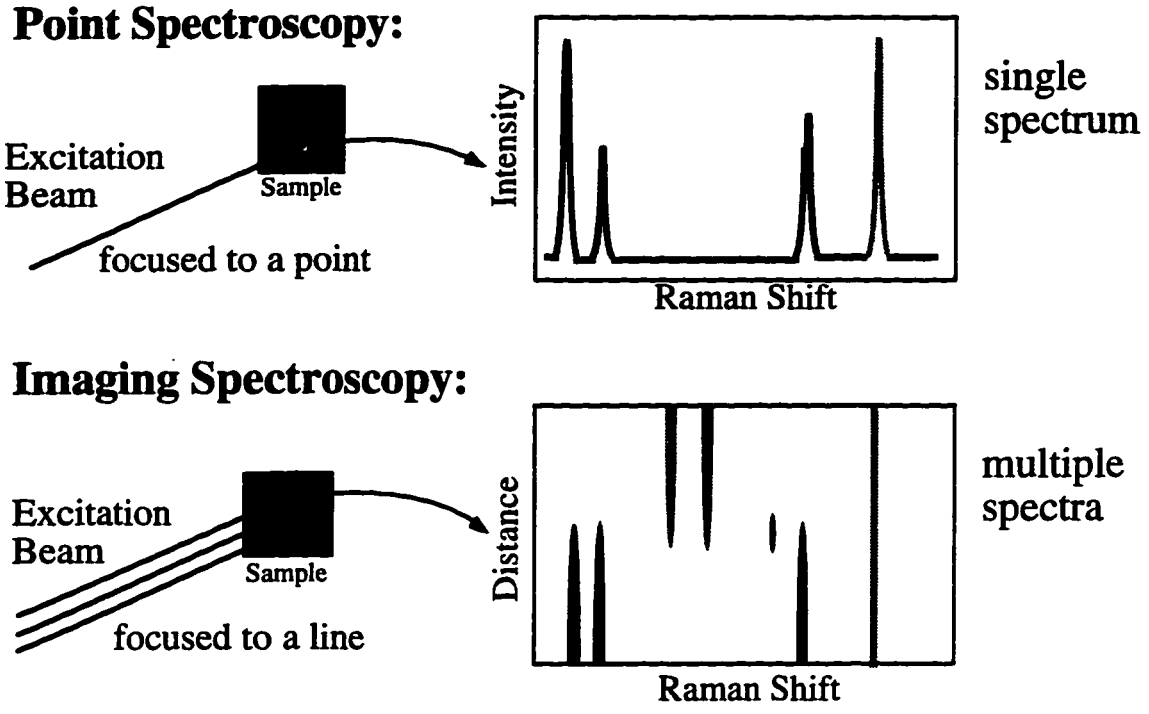

Figure 2.1. Schematic comparison of imaging versus point spectroscopy

With line-imaging spectroscopy, a spatial dimension is added to traditional spectroscopic information. In the top portion of Figure 2.1, a spectrum from a two-part sample is shown schematically. The point spectroscopy shows four vibrational modes coming from the bottom half of the sample, where the excitation beam is focused. If the top half of the sample is to be investigated, the excitation point must be moved into that region. Similarly, if the interface between the two materials is of interest, the excitation point must be located there. The bottom of Figure 2.1 shows a spectroscopic line-image taken from the sample. With line-imaging spectroscopy, the excitation beam is focused to a line that crosses the interface in the material. The horizontal axis of the image still shows Raman shift (as in the spectrum above it), but the vertical axis now shows spatial position. The intensity of various vibrational modes comes out of the page and is represented by a grayscale. The lower half of the line-image provides spectroscopic data from the lower half of the sample, whereas the top half of the image corresponds to the top half of the sample.

The four vibrational modes seen in the point spectrum, which came from the bottom half of the sample, can be identified in the bottom half of the line-image. The top half of the line-image shows there are three vibrational modes arising from material in the top half of the sample.

One immediately notices several features revealed by the image that are not discernible in the single spectrum. The line-image shows how sharp of an interface exists between the two halves of the sample by noting (spatially) where the signal from each half becomes undetectable. One also notices that the rightmost vibrational mode is common to both the top and bottom of the sample, indicating that it is not specific to either half. This piece of information may make peak assignments easier than if only a single spectrum were available. Also noticeable in the image is a vibrational mode which is only present at the sample interface. This indicates the adhesive mechanism may not solely be a mechanical bond, but rather has some chemical nature. The spatial length of this vibrational mode also helps define the thickness of the interface.

Unlike successively moving a point across a sample, an image is continuous in the spatial dimension. The spatial resolution is set by a combination of optical magnification and detector geometry, but theoretically only limited by the wavelength of light. Also, all the information in the image is collected under the same experimental conditions, thus avoiding problems associated with relocating the excitation spot in traditional point spectroscopies. This comparison of point spectroscopy and line-imaging spectroscopy clearly illustrates that imaging not only allows collection of spectra, but adds an entire dimension of complementary information.

2.3 Recent developments in line-imaging Raman spectroscopy

Since Raman spectroscopy is a vibrational spectroscopy, it can quantitatively identify species based on their molecular "fingerprint". When used in a line-imaging

system, spectroscopic information from both an electrode surface and solution may be gathered simultaneously in a continuous image that contains one dimension of spatial information and one dimension of spectral information, making line-imaging Raman well-suited for electrochemical studies of thin film deposits and electrolyte chemistry.

Line-imaging Raman spectroscopy has recently emerged as a powerful tool for materials science studies,[28-30] combustion research,[31-33] and mass transfer in microparticles,[34] but until very recently affordable high-performance imaging spectrographs, holographic optical elements, and 2-D detectors have not been available that allowed construction of a line-imaging system applicable to electrochemistry.

Dauskardt and coworkers used line-imaging Raman spectroscopy to study solid phase transitions during crack propagation in zirconia.[30,35] Two phases of zirconia, tetragonal and monoclinic, can be distinguished by their Raman spectra. A mechanical load was applied to a sample of zirconia causing a crack to form. When the load was removed, crack propagation ceased. By imaging along the axis of the crack, it was shown that a local solid phase change can extend up to 1300 μm ahead of the crack tip.

Instruments of this generation (*ca.* 1990) had a number of limitations related to acquisition time, flat-field optics and spatial resolution. In this study the time scale of the experiment was essentially infinite. After removing the applied load, crack propagation stopped and did not resume until the load was reapplied, allowing extreme flexibility of image exposure time. Monochromatic emissions from an Ar^+ laser focused to a line illuminated the region of interest. Images were collected with a two-dimensional photomultiplier tube (PMT), which had an effective spatial resolution of 28 μm. Resolution of roughly one fifth of this (≈5 μm) is required for electrochemical systems. A single spectrometer was used that did not provide a uniform focused zone resulting in

warped images which had to be corrected. Clearly there exists the need for further instrument refinement.

Line-imaging Raman spectroscopy has also been used to investigate flame chemistry as demonstrated by Reckers and colleagues who report on their ability to resolve the spatial density variation of individual gaseous species (H_2, O_2, N_2, H_2O and $OH^{\bullet}$) and the local temperature in a laminar H_2 flame.[31] The excitation beam from a pulsed, tunable KrF excimer laser focused with a long (2m) focal length lens was aligned perpendicular to the axis of the flame at various heights from 2 mm to 8 mm above the burner. By imaging along a 4 mm range centered at the flame center, the density and temperature of combustion species were probed. Temperature was calculated using two different methods from the spectral data at each spatial location.

The length scales and spatial resolution of the flame system studied by Reckers are much greater than in typical electrochemical systems. The length scales of the combustion zones are on the order of 500 μm. The Schmidt (Sc) number, the ratio of momentum diffusivity to molecular diffusivity, is usually ≈0.2-5.0 for gases,[36] but in electrochemical systems, the Schmidt number is ≈1000. Laminar concentration boundary layer thickness scales as $Sc^{-1/3}$, indicating length scales of ≈50 μm for a comparable electrochemical reaction-diffusion system.

Reckers et al. used an uncooled charge coupled device (CCD) detector, preceded by an image intensifier to collect the images rather than the older style 2D PMT used by Dauskardt et al.. The devices were fiber-optically connected. A CCD detector greatly decreases the dark signal during image acquisition, increasing the allowable exposure time, and thus, instrument sensitivity. Reckers reports a theoretical spatial resolution of 12 μm, although the quality of the optics and the detector limit the resolution to an empirical value of, "at least 150 μm." He concludes by stating that, "Further improvements of the shown

results should be possible by using a cooled CCD camera with at least 12 bit resolution." Further instrument development is needed to use line-imaging Raman spectroscopy in electrochemical systems. Addressed specifically by Reckers is the general need for a low-noise detector, greater bit-depth and better spatial resolution in order for line-imaging Raman to mature as a technique.

Recently Vehring et al. have used line-imaging Raman spectroscopy to explore absorption, dissociation, and isomerization in the SO_2-H_2O system, as well as desorption of CO_2 from water droplets.[34] In this study, microparticle droplets emitted from a vibrating particle generator react with the surrounding gas phase. By imaging perpendicular to the droplet stream, concentration profiles of water and carbon dioxide can be seen from the center of the reacting particle into the gas phase. From this, it was determined that the limiting mass-transfer step during desorption is liquid phase diffusion. From the gradients of the concentration profiles, mass transport in the gas phase can be estimated and applied to a model of transient diffusion from a sphere without convection. Since the speed of the droplet chain is known, specific spatial locations correspond to specific times during the CO_2 desorption process. Taking images at several downstream distances and watching the CO_2 ν_1 mode at 1384 cm^{-1}, Vehring determines the temporal concentration of CO_2 in the microparticle. When this profile is compared with the diffusion model, the two agree qualitatively, but not quantitatively. The diffusion model predicts higher concentrations than are actually found. This is attributed to mass transfer that takes place during the initial stages of droplet stream formation before discrete microparticles have been formed.

Vehring's ability to image concentration profiles allowed the identification of important mass transport steps in the study of microparticles, but it also represents one of the first (besides our own) mature line-imaging Raman spectroscopy systems. This system uses a cooled CCD detector, which produces essentially no dark signal, and has very good

resolution and range. Vehring reports a spatial range of 1.4 mm, along with a theoretical spatial resolution of 2.4 μm, but due to stability of the droplet chain, has an effective spatial resolution of 50 μm.

In an effort to achieve the best possible spatial resolution, line-imaging Raman has been coupled with microscopy. Here, a microscope objective lens is used as the collection lens allowing spatial resolutions to approach the theoretical resolution of visible light (≈1 μm). Drumm *et al.* report using this approach to image polystyrene and polyethylene blends, with a spatial resolution of 1.4 μm.[37] In this work, rather than collecting a single image and investigating the chemical variation along a line positioned across a region of particular interest, the focused line is rastered across a sample and an image taken at each location. This collection of images is then used to produce spatial-spatial images highlighting a particular Raman mode. In this way, spatial regions of one chemical constituent (polystyrene or polyethylene) can be mapped. Drumm shows images 250 μm long with a spatial resolution of 1.4 μm. The line-imaging method used by Drumm *et al.* has very high spatial resolution, but one of the major drawbacks is the need for a very short optical working distance, which limits the type of electrochemical systems that can be investigated with this configuration.

The previous examples illustrate the attributes of line-imaging Raman, but also show a progression of available technology and refinement of instrumental performance. The prototype instrument used a PMT array which was limited by dark signal and read-out noise. Minimal dark signal is crucial for the collection of Raman signal with acceptable signal to noise ratio. This effect becomes especially pronounced in imaging applications where the collected light is spread in an additional dimension. With the advent of liquid nitrogen cooled CCD technology, dark signal is drastically reduced and spatial resolution is also improved. Dark signal is all but eliminated with cooled CCD detectors, affording

16-bit image depth with many hour exposure times. Along with the ever increasing availability of imaging spectrographs, which provide a non-distorted focal plane, it has only recently become possible to construct a line-imaging Raman spectroscopy system applicable for use in electrochemical systems.

2.4 Applying Line-Imaging Raman to Electrochemical Systems

Line-imaging Raman spectroscopy has yet to be used for the study of electrochemical systems. As discussed above, in many electrochemical systems it is desirable to obtain detailed chemical information continuously from the electrode surface into the solution above it, or to obtain chemical information across the surface of an electrode or electroactive thin film. Line-imaging Raman spectroscopy seems particularly well-suited to study these systems since the technique is able to collect information along the appropriate length scales (*e.g.* electrochemical concentration boundary layer) with appropriate spatial resolution. The cases where line-imaging Raman has been used previously, and the applicability to current electrochemical problems show great promise, and are the basis of our motivation to design and construct such an instrument in our laboratory for use in electrochemical systems.

2.4.1 Instrumentation

2.4.1.1 Hardware

Our imaging Raman system is based on a traditional Raman spectroscopy system. The excitation beam is provided by either Ar^+ or Kr^+ lasers (Laser Ionics, 1401.4A/1400-1K) with main lines at 488 nm, 514.5 nm, and 647.1 nm used. Plasma emissions from the laser are removed with a narrow bandpass filter (Omega Optical). The

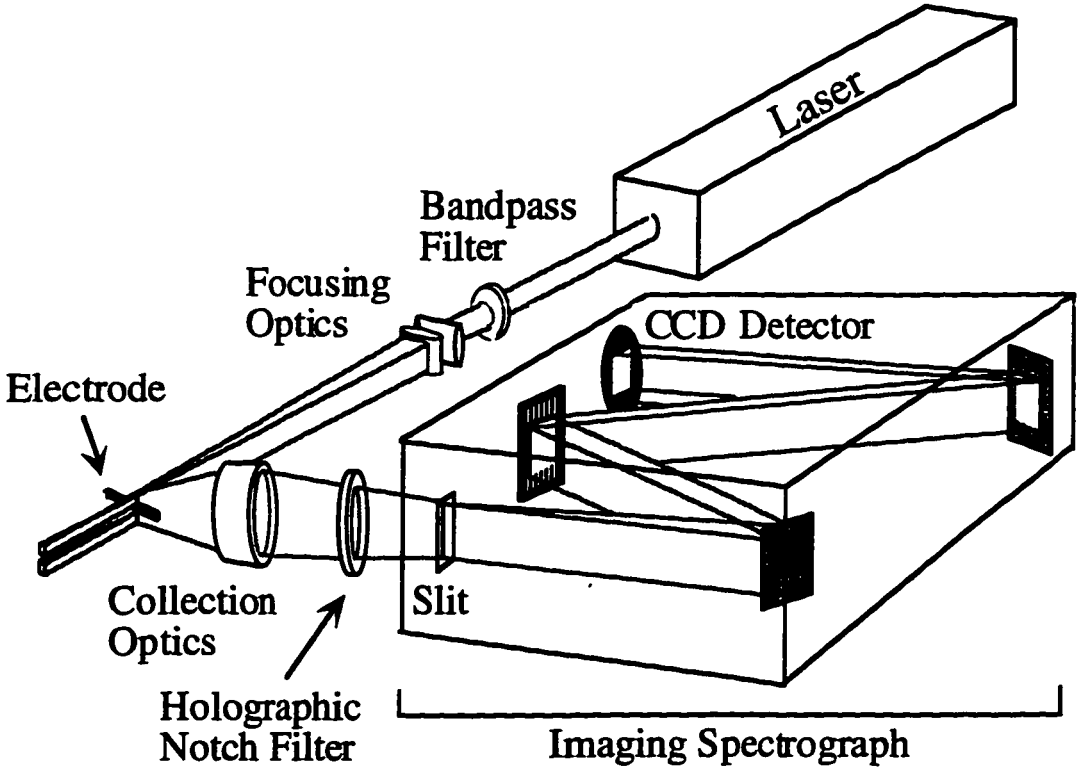

Figure 2.2. Schematic of imaging Raman system components and optical train

laser is focused to a line using an f/10 cylindrical lens set, or a combination of one cylindrical lens and one spherical lens. Scattered light is collected at 90° from the incident beam by an f/1.2 Nikon camera lens. The elastically scattered portion of the light is attenuated by an OD6 holographic notch filter (Kaiser Optical) prior to entering the spectrograph. A 270 cm, f/4 imaging spectrograph (Spex Industries model 270M)

equipped with 600 and 1800 gr/mm gratings disperses the inelastically scattered light onto a liquid nitrogen cooled two-dimensional CCD array containing 1024 pixels of spectral information and 256 pixels of spatial information (Princeton Instruments model LN/CCD-1024E). For electrochemical measurements a PAR 273 or 273A is interfaced with the Raman system and controlled in either potentiostatic or galvanostatic mode. See Figure 2.2 for a schematic of the optical arrangement.

2.4.1.2 Software and instrument control

The spectroscopic and electrochemical instrumentation is controlled by a Macintosh Centris 650 computer running LabView over a GPIB interface. All software was custom written, including simultaneous multiple instrument control, data acquisition, post-collection spectral, spatial and full-image display, calibrated spectral axis, automated baseline removal, flat-field correction, image notation, noise and cosmic spike filtering, and file compression. Although the body of controlling and processing software is extensive, it is written in a very modular fashion to allow powerful, experiment-specific routines to be easily interfaced with the instrument in a short amount of time. All instruments are GPIB (general purpose interface bus) devices, which allow for fast, reliable data and command transfer, and are platform independent giving the instrument an additional degree of modularity. Appendix A describes this body of software.

2.4.2 Line-image of a ruled target

Figure 2.3 below shows a simple line-image of krypton laser plasma emissions reflected off a ruled target with bar spacing of 15 lines/mm, or ≈34 μm/line. The lines are lithographed chromium deposited on a glass substrate. The abscissa consists of 1024 pixels in the spectral dimension, and the ordinate consists of 256 pixels in the spatial dimension. The left side of the line-image shows the ruled target. White horizontal lines symbolize highly reflective chromium lines, and the black locations symbolize the less

reflective glass substrate. In this grayscale line-image, black is most intense, and white is least intense. Regions of high intensity (dark dots) are positioned on the image spectrally where a plasma emission occurs, and spatially where a reflective chromium deposit occurs.

At the top portion of the ruled target there are no lithographed lines. Correspondingly, in the same spatial region of the image (directly to the right) there are no regions of high intensity. Likewise, at spectral regions where there are no plasma emissions, there are no regions of high intensity in the image. Lower on the target the lithographed lines reflect the plasma emissions giving rise to dark dots on the image at the spatial location of the lithographed line and at the spectral location of the plasma emission. Only at spatial-spectral locations where a plasma emission reflects off of a lithographed line does a region of high intensity exist in the line-image.

At the top of the image is the "spatially binned" or average spectrum of the image. This spectrum is the sum total of all the rows (spectra at a particular spatial location) that comprise the image. It shows the spectral locations of the krypton plasma emissions of the laser that reflect off of the lines on the target. Similarly, to the right of the image is the "spectrally binned" or total intensity profile across the image. This profile is the sum total of all the columns (intensity profiles at a particular wavelength) that comprise the image. This profile shows where the lithographed lines are spatially located. Notice that there are spatial peaks only at line locations on the target. The image demonstrates how spectroscopic information varying over space is displayed in a line-image.

The intensity profile of the laser excitation line has a definite influence on the

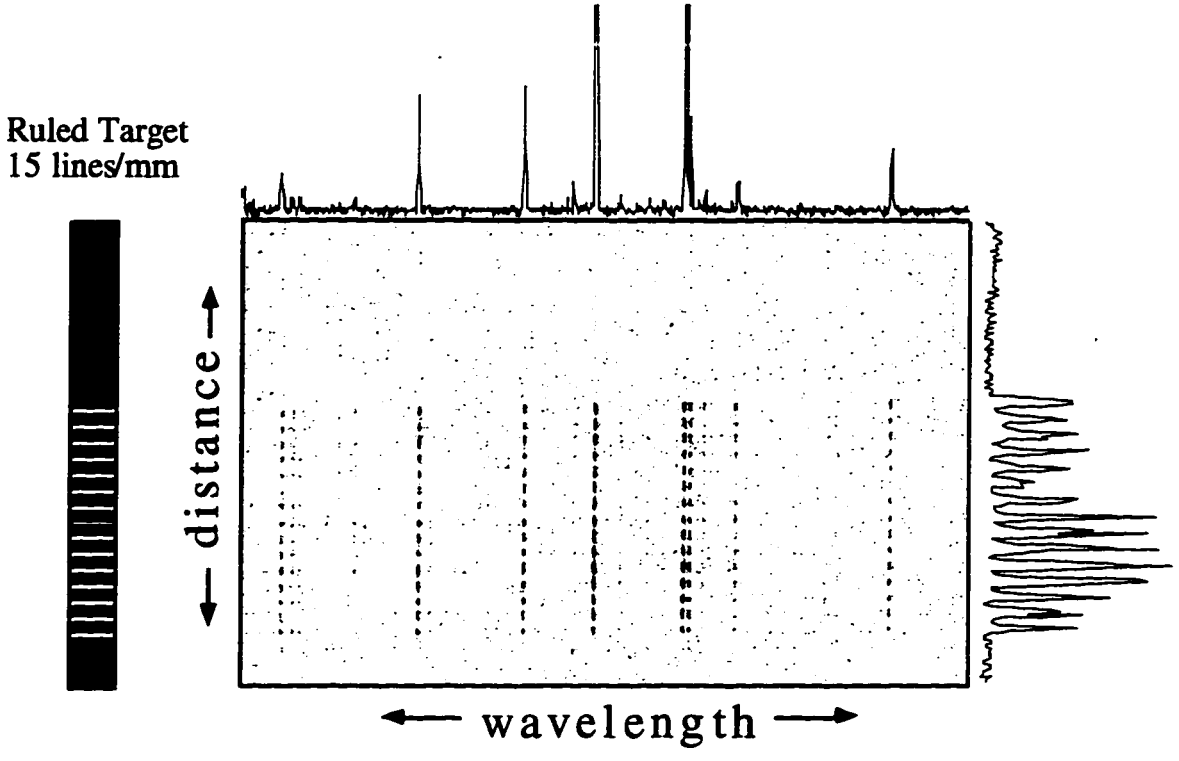

Figure 2.3. Line-image of a ruled target. At the top of the image is the "spatially binned" or average spectrum of the image. To the right of the image is the "spectrally binned" or total intensity profile across the image.

line-image. If the laser excitation line has a Gaussian profile, the spatial intensity variation in the image that results will also generally follow a Gaussian profile. When a surface is imaged, this profile is perturbed, however, by the local surface morphology of the sample. When a solution or boundary layer is imaged, the overall Gaussian shape can be perturbed by local differences in the solution's index of refraction. The intensity profile of the plasma emissions shown above are essentially uniform over the distance imaged here, however in the peak intensities in the total intensity profile shown to the right of the image in Figure 2.3, a degree of nonuniform intensity can be seen. The nonuniformity of the reflected light can be caused by dust on the target, nonuniform surface morphology of the lithographed lines, or some other surface imperfection. In later chapters, examples of these common line-image features will be presented.

The spectral resolution and spectral slitwidth are set by the characteristics and settings of the spectrometer. Our system can be calibrated to be accurate to within 3 cm^{-1}, and is normally operated with a spectral slitwidth of 8 cm^{-1}. The spatial resolution, on the other hand, is ultimately determined by the wavelength of light and the number of pixels in the spatial dimension of the CCD chip. With visible light, $\approx$1 μm is the highest possible resolution. Spatial range is sacrificed in exchange for spatial resolution however.

2.5 Conclusions

In this chapter, it is shown how the line-imaging technique produces an image possessing one spatial and one spectral dimension. The progression of equipment performance has reached a stage where a line-imaging system that is able to collect information with the appropriate spatial length scales and resolution for electrochemical systems. The instrumentation used for the custom-built line-imaging Raman system used in this dissertation work is presented, along with an illustration of a line-image from a ruled target.

CHAPTER 3: IN-SITU IMAGING OF ELECTROCHEMICALLY-DEPOSITED CUSCN AND $CUSO_4$ BOUNDARY LAYERS

3.1 Chapter Overview

Imaging Raman spectroscopy is explored as a new tool for *in-situ* studies of electrochemical systems. The technique provides a spatially resolved view of molecular species present along a focused laser line. The capabilities of our system are demonstrated using an electrodeposited thin film of CuSCN plated on a cylindrical platinum electrode, and by directly imaging concentration boundary layers during the electrodeposition of copper from a binary electrolyte. It is shown that line-imaging Raman spectroscopy is able to measure the properties of the CuSCN thin film deposit while simultaneously monitoring the concentration of solution species within a 1 mm region of the surface. For the copper deposition case, it is shown how the instrument is able to monitor changes in the concentration boundary layer at different rates of deposition continuously from the bulk solution to the electrode surface.

3.2 Characterization of the Line-Imaging Raman System

3.2.1 CuSCN system

After design and construction of the imaging Raman spectrometer, two experimental systems were analyzed to verify proper instrument operation. We initially investigated the electrodeposition of copper thiocyanate (CuSCN), a p-type semiconductor of interest in our laboratory for its possible use in solar-cell applications.[15,16]

3.2.1.1 Experimental Setup

A spectroelectrochemical cell was constructed using a four-sided clear UV-Vis cuvette. A horizontal 500 μm platinum wire electrode was used as the working electrode. CuSCN was electrodeposited from an aqueous solution of 25 mM KSCN and

100 mM $CuSO_4$ onto the 500 μm diameter cylindrical platinum electrode. The axis of the cylindrical electrode was parallel to the optical table plane, and rotated ≈22° away from the optical axis formed by the collection lens. Figure 3.1 shows a schematic the geometry of the excitation and collection optics, and the optical sampling volume which results from this arrangement. The laser power at 488 nm was 1.0 W.

In the line-imaging Raman spectrometer described above, a line of scattered light was imaged onto the spectrograph slit and then dispersed to create a two-dimensional map of spectral and spatial information which was acquired on the two-dimensional CCD array detector. The light that made it into the spectrograph originated from the region we refer to as the optical sampling volume. The slit-width of the imaging spectrograph provided a long, thin (in width and depth) optical sampling volume viewed by the CCD detector. The width (W) of the optical sampling volume was approximately 30 μm, as dictated by the width of the spectrograph entrance slit. The height (H) of the sampling volume was approximately 1.5 mm, as dictated by the vertical dimension of the CCD array and optical magnification. The diffraction limited beam waist of the focused laser was 6.2 μm, although we assigned the depth (D) of the sampling volume to approximately 150 μm, as

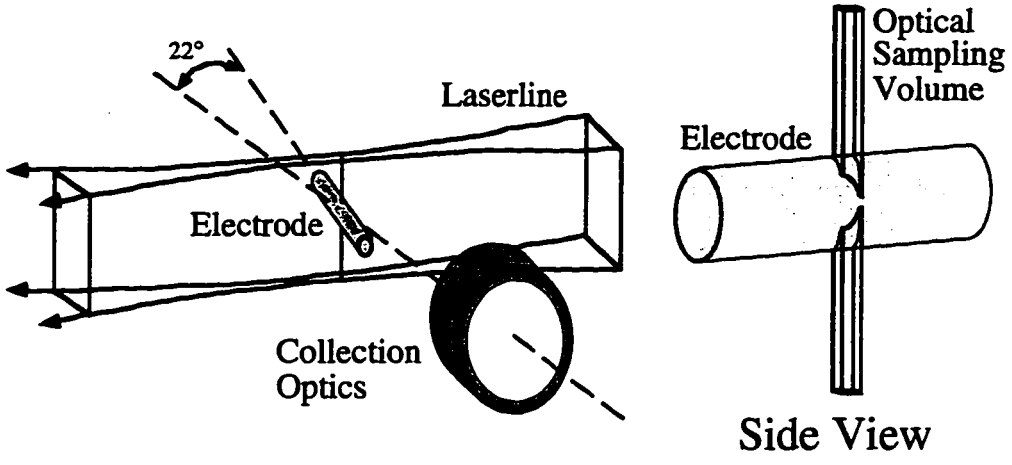

Figure 3.1. Schematic of the excitation and collection optics geometry, and the optical sampling volume.

described later. Thus, with a W:D:H aspect ratio of 1:5:50, the imaging Raman spectrometer provided a spectroscopic "snapshot" of the chemistry occurring along a (nearly) one-dimensional laser-illuminated line placed within the electrochemical cell.

The size, geometry and orientation of the electrode were chosen for several reasons. A 500 μm diameter wire was used because this diameter corresponded to roughly one-third of the 1.5 mm effective spatial range of the detector. This allowed for the analysis of surface films on the electrode as well as collection of Raman signal in the boundary layer and bulk solution above and below the wire. A cylindrical geometry was selected because we intend to use acoustic mixing in the future, and this flow is especially well-characterized for this geometry. Finally, the electrode's axis was offset 22° from the axis of the collection optics to avoid possible "self-shadowing" effects from portions of the electrode located between the illumination point and the collection optics.

3.2.1.2 Verification of Imaging Capabilities

Shown in Figure 3.2 is a Raman image of electrodeposited β-CuSCN. The exposure time was 9000 s. Usable images can be acquired with much shorter exposure times (~30 s), but this long exposure time was chosen to produce an image with an extremely high signal to noise ratio.

The horizontal axis of this image is the spectral axis shown in Raman shift, and the vertical axis is the spatial axis shown in micrometers. The horizontal wire and the focused excitation beam are shown on the left side of the figure. The dotted region corresponds to the optical sampling volume. Three main features of the image are apparent: broad Raman signal from water, comprised of the ν_1 stretch at 3450 cm^{-1}, the $2\nu_2$ asymmetric stretch at 3225 cm^{-1}, and the ν_3 stretch at 3630 cm^{-1} spanning the entire image vertically, Raman

signal from the CN stretch of β-CuSCN† (2175 cm^{-1}) appearing as two vertically-aligned spots, and an attenuated band crossing horizontally through the middle of the water band and β-CuSCN Raman spots. The horizontal attenuated band is from the portion of the optical sampling volume that is blocked by (or located "within") the cylindrical electrode (see Figure 3.1). For example, the water concentration does not vary through the electrolyte, so its signal strength should remain spatially uniform. However, since the optical sampling volume is placed (deliberately) in such a manner that it passes through the center of the cylinder, a portion of the optical sampling volume (related to the electrode diameter) is eclipsed by the electrode, leading to the 500 μm wide attenuated band passing horizontally through the water (and β-CuSCN) signal.

---

† There is some discrepancy in the literature as to the proper phase assignment (α or β) based on the wavenumber of the CN stretch.[38,39] We have determined through X-ray diffraction, that the CN stretch at 2175 cm^{-1} corresponds to the β phase.

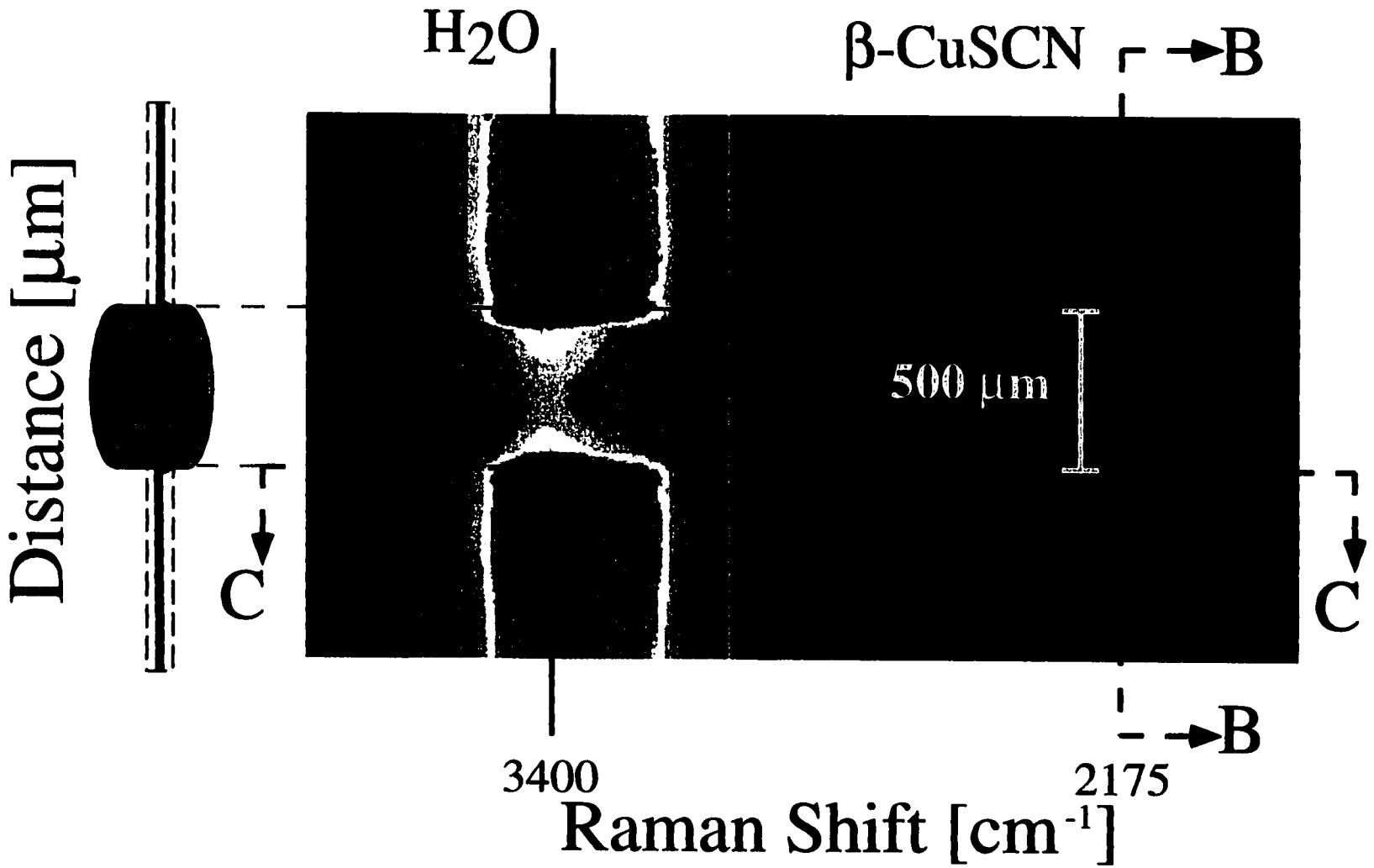

Figure 3.2. Raman image of electrodeposited β-CuSCN.

Figure 3.3 shows the BB vertical slice (2175 cm^{-1}) from Figure 3.2. The BB vertical slice shows the spatial intensity variation of the CN stretch in β-CuSCN. Raman signal is seen most intensely near the top (+250 μm) and bottom (-250 μm) of the electrode because these are the regions of the optical sample volume that sample the most electrode surface. The spatial separation of the peaks corresponds to the 500 μm diameter of the electrode. The data in Figure 3.3 show the depth of the optical sampling volume must be considerably less than the electrode radius (250 μm). From the spatial width of the β-CuSCN spots and the attenuated region in the water signal, we have tentatively assigned a sample volume depth of 150 μm. The spatial resolution of this figure is ≈5 μm.

Figure 3.3 also shows the CC horizontal slice from Figure 3.2. The CC horizontal slice shows the Raman spectrum at the electrode surface. The water band is clearly seen with a maximum at 3450 cm^{-1}, and the CN stretch from CuSCN appears at 2175 cm^{-1}. Also evident is the ν_2 asymmetric stretch of water centered at 1645 cm^{-1} (shown as inset),

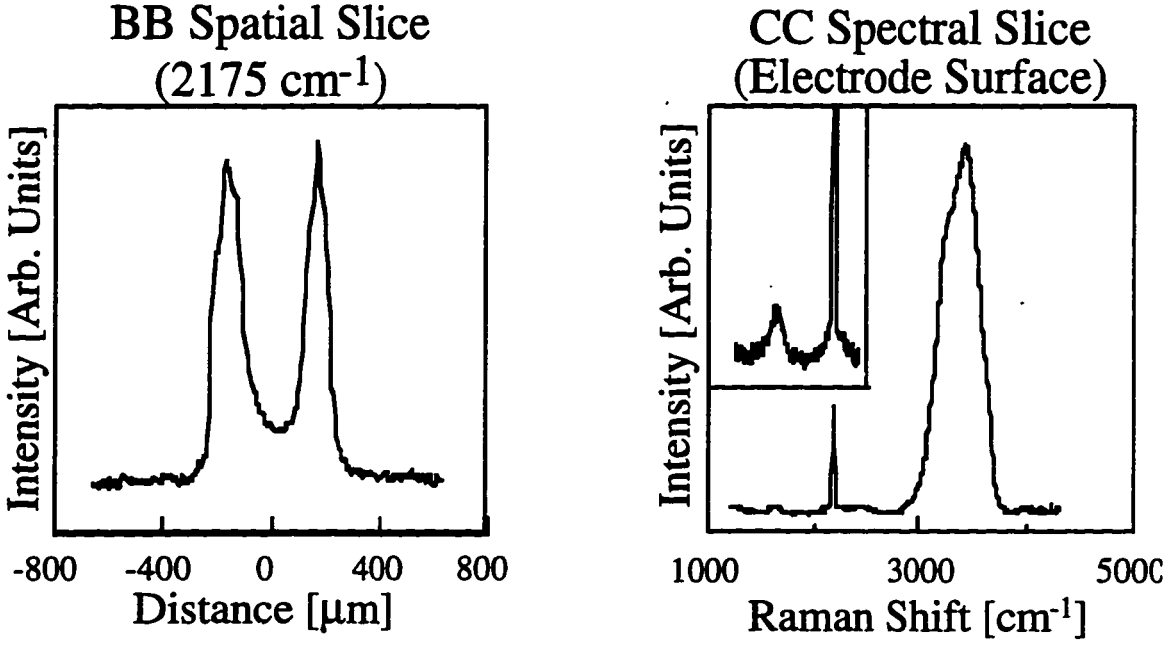

Figure 3.3. Spatial and Spectral cross-section of the β-CuSCN Raman Image

which cannot be seen in Figure 3.2 due to the 8-bit depth of the image presented here (the data are acquired with 16-bit depth). The ν_2 peak (1645 cm^{-1}) has a similar spatial cross section to that of the water signal at higher wavenumbers, although with a much lower signal-to-noise ratio.

3.2.1.3 Detection of $Cu(SCN)^+$ Solution Species and β-CuSCN Deposit

In addition to the surface species (β-CuSCN) we also detected what we believe to be copper (II) thiocyanate in solution, $Cu(SCN)^+$. A shift in electronic structure can shift the location of vibrational bands. It has been shown in the literature that the wavenumber of the CN stretch can be highly affected by the local environment.[40,41] Figure 3.4 is an image taken with the 1800 gr/mm grating. The image has a spectral slitwidth of 10 cm^{-1}, a spatial resolution of 5 μm, and was acquired in 900 s. With this increased spectral resolution and elimination of the large water Raman bands, one can see the Raman signal from the complex form in solution at a lower wavenumber shift (2127 cm^{-1}) than the surface species (2175 cm^{-1}). The optical sampling volume was not directly centered on the wire electrode; therefore, more electrode surface is sampled than in the previous image. The relative signal intensity from the solid surface species, CuSCN, is approximately 300 times that of the aqueous solution species, $Cu(SCN)^+$. To visualize the solution species in this image required color-table expansion at the lower signal levels, thus making the surface species' signal appear "overexposed".

These two images (Figure 3.2 and Figure 3.4) show that our imaging Raman system is functional and able to discriminate between species spatially and spectrally. This implies we have constructed an instrument that should be able to locate and identify solution and surface species, and do so with appropriate lengthscales and resolution.

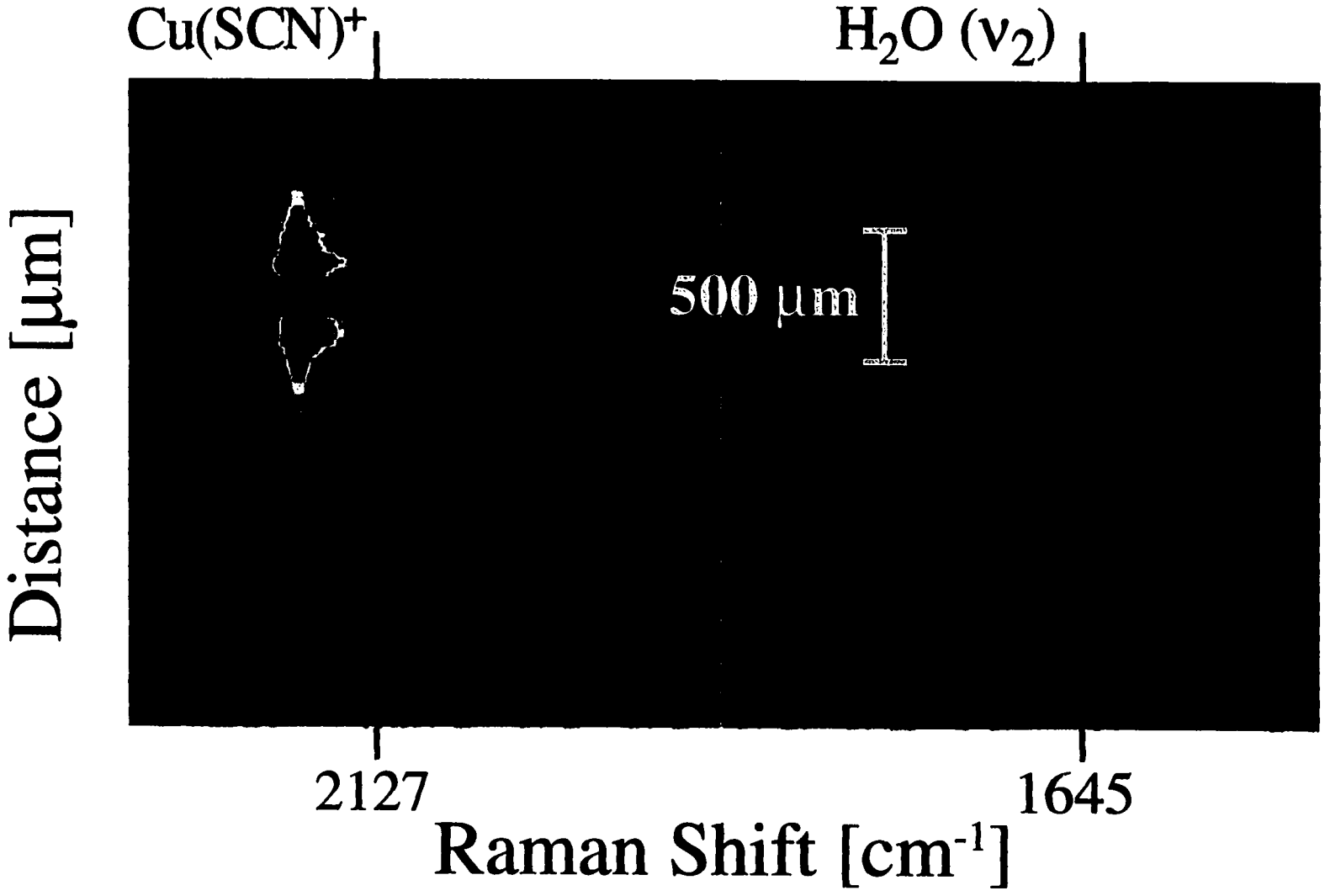

Figure 3.4. Presence of $Cu(SCN)^+$ in solution.

3.2.2 $CuSO_4$ system

The second system we looked at to assess imaging capabilities was the electrodeposition of copper from a binary electrolyte. With the $CuSO_4$ system, the goal was to assess the ability to measure concentration changes during deposition very near the electrode surface, within the concentration boundary layer. Since we used a binary electrolyte, electroneutrality requires the Cu^{+2} concentration to equal that of SO_4^{-2} everywhere in solution except in the electrical double layer. Therefore Raman signal from the sulfate can be used to follow the concentration of Cu^{+2} (which has no Raman bands). The totally symmetric stretching mode of the sulfate anion at 983 cm^{-1} was used to probe the concentration of the Cu^{+2} species.

3.2.2.1 Experimental setup

Copper was deposited from a binary electrolyte of 0.5M $CuSO_4$ onto a 500 μm diameter horizontal cylindrical platinum wire electrode (area=0.055 cm^2) positioned in the spectroelectrochemical cell as described in §3.2.1.1. The copper deposition was performed at three different overpotentials: -50 mV, -80 mV, and -300 mV, which yielded average current densities of 60.3, 94.8, and 125.5 mA/cm^2, respectively. An image was also taken at zero overpotential, the nonreacting case. All other experimental factors were identical to those described in §3.2.1.1.

3.2.2.2 Free-Convection Flow Field

During the electrodeposition, solution very near the horizontal electrode wire becomes depleted in Cu^{+2} and its density decreases from the bulk solution value of ρ=1.077 g/cm^3. This density difference gives rise to a laminar free-convective flow field. This problem has been solved numerically for the analogous free-convection system in heat

transfer with a particularly clear visualization of the fields shown in Figure 3.5†. Fluid impinging on the bottom side of the wire compresses the hydrodynamic and concentration boundary layers. Fluid rising from the top of the wire expands the boundary layer.

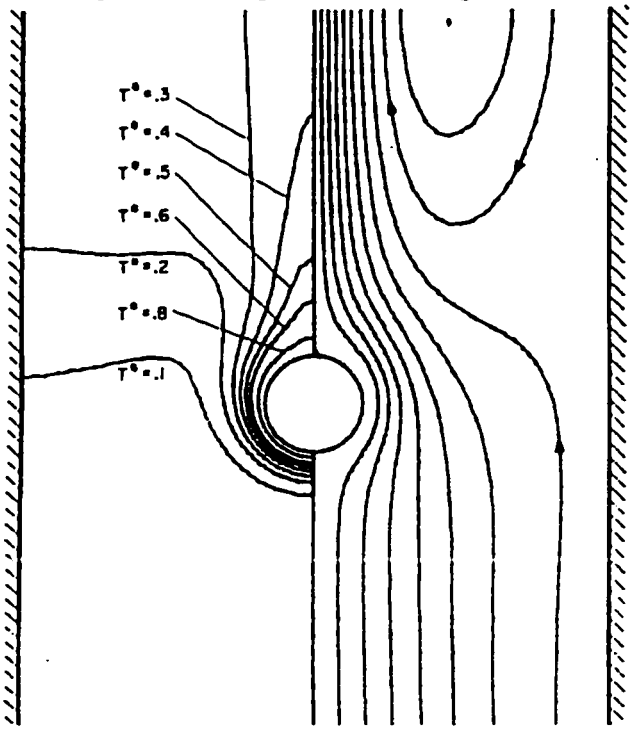

Figure 3.5. Numerical solution for free-convective flow and temperature fields from an isothermal horizontal rod. The left side of the figure shows lines of constant temperature (T*=nondimensional temperature). The right side of the figure shows streamlines of the flowfield.

† The figure shown here is taken from Kakaç et al., which shows the temperature and flow fields arising from a free-convective flow around an isothermal horizontal cylinder between confining walls.[42] This figure is qualitatively similar to the electrodeposition-induced convective flow of interest, but not quantitatively since different physical parameters were used.

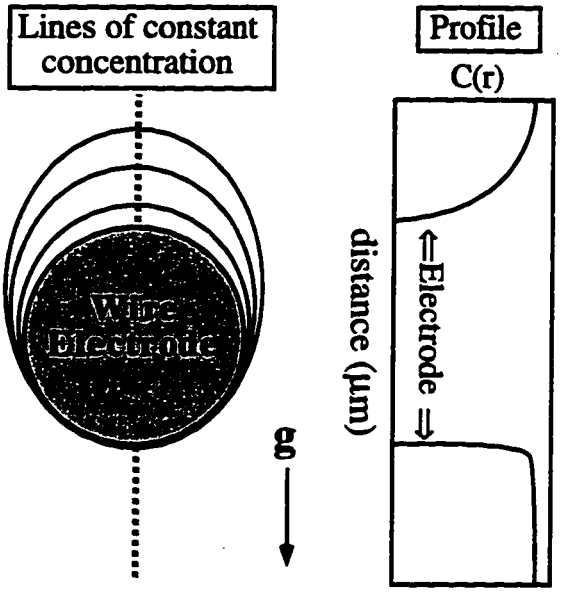

Figure 3.6. Concentration Field and Centerline Concentration Profile

Looking schematically at the concentration field, Figure 3.6, the expected concentration profile along the vertical centerline is compressed to a very thin layer below the electrode, and is expanded above the electrode.

3.2.2.3 Imaging of Concentration Boundary Layer

Figure 3.7 shows a Raman line-image during the electrodeposition of copper at 300 mV cathodic overpotential. The wire electrode and optical sampling volume region is shown to the left of the image. Since the Gaussian laser intensity profile is superimposed on a Raman line-image, this influence must be removed before spatial variations due to concentration can be determined. This is accomplished by normalizing the profile of a reactive image by the profile of a nonreactive image. The image shown in Figure 3.7 has been normalized using the ν_1 stretching mode (983 cm^{-1}) of SO_4^{-2} from a non-reacting case. Exposure time for this image was 100 s.

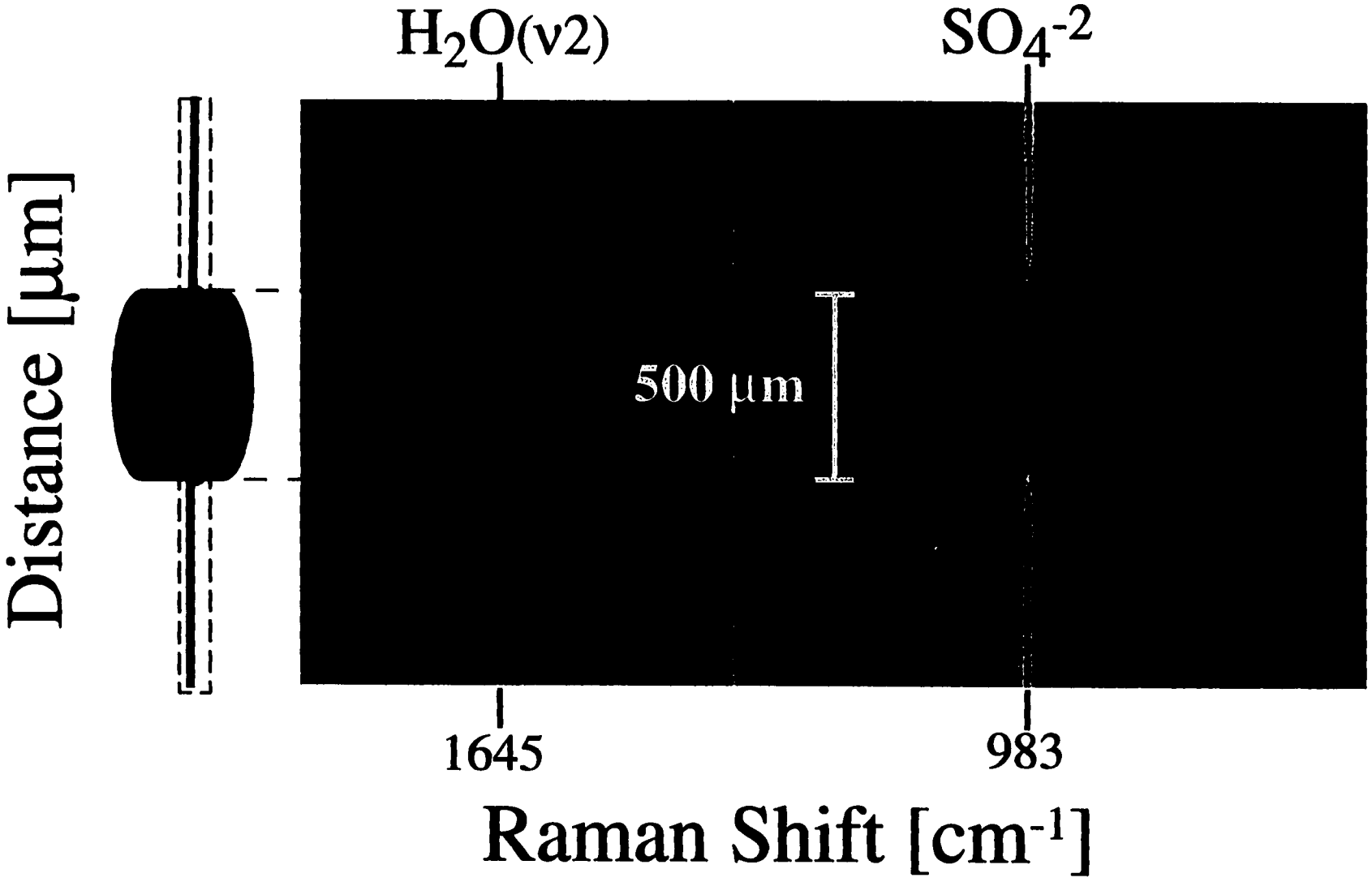

Figure 3.7. Raman image acquired during the electrodeposition of copper at -300 mV overpotential.

Four features are readily apparent in this image: the vertical line from the symmetric sulfate stretching mode (983 cm^{-1}), several dot pairs appearing at the top and bottom of the electrode, the Raman signal from the ν_2 water band (1645 cm^{-1}), and the horizontal region of attenuated signal spanning the image where the electrode is located. The latter two features have been discussed previously.

During the acquisition of Figure 3.7, the plasma-line filter (optical narrow bandpass) was removed from the optical train allowing elastically scattering plasma lines to strike the sample. Since laser plasma emissions are very weak, only elastically scattered light from the surface regions in the optical sampling volume are detected. This elastic scattering gives rise to "surrogate" surface species seen as dot pairs in the image. These plasma lines can be used to precisely determine the boundary between surface and solution, as well as for spectral calibration points.

The intensity of the vertical Raman line at 983 cm^{-1}, from the SO_4^{-2} anion is an indication of the Cu^{+2} cation concentration during the deposition. No appreciable intensity variation is seen in the image at locations below the wire, indicating uniform concentration. Right above the electrode surface a slight intensity drop can be noticed compared to the bulk solution present well above the electrode. The spatial variation of the Cu^{+2} can be better seen by looking at a spatial slice through the 983 cm^{-1} band, where the Raman signal is proportional to the concentration of SO_4^{-2} in solution.

Figure 3.8 shows the imaged concentration profiles above and below the wire electrode at several deposition overpotentials. Lines represent smooth curves drawn through the data points. Positive distances denote spatial positions below the wire, and negative distances denote spatial positions above the wire. The rate of deposition reaction at the electrode surface is driven by the overpotential of the electrode (η). When η=0,

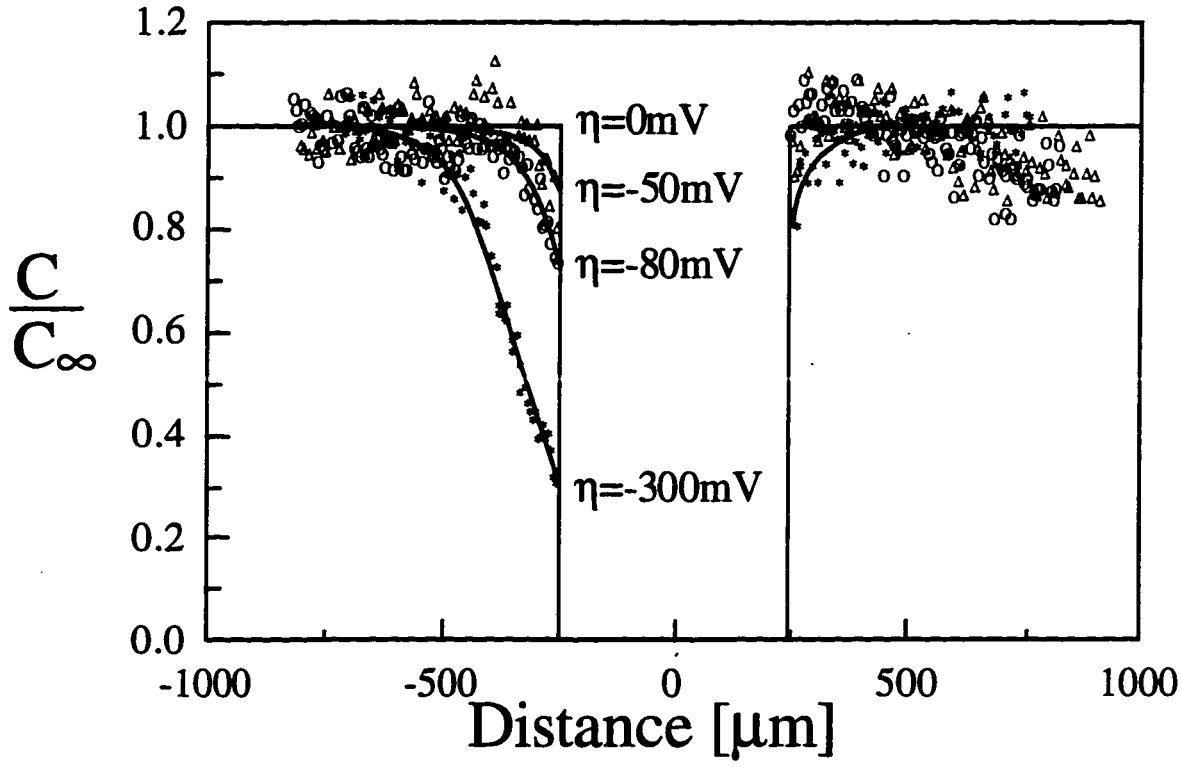

Figure 3.8. Imaged concentration boundary layers for four different deposition overpotentials (η).

there is no reaction and there is no current. As η becomes more negative, the deposition current increases. So for η=-50, -80, and -300 mV, the current goes from about 10.2, 16.1, and 21.3 mA, respectively. Above the wire, where the concentration boundary layer (δc) is expanded by the flow, one observes a region depleted of reactant for all overpotentials (except 0). The depleted region grows as the deposition increases. Below

the wire electrode the flow compresses the boundary layer so that appreciable concentration variation is visible only at the highest deposition rate.

Figure 3.8 shows that with increasing driving force, the thickness of the concentration boundary layer increases, the surface concentration decreases, and the surface flux increases. Figure 3.9 quantifies the boundary layer thickness above the wire as a function of total current through the cell for several experiments. The concentration boundary layer thickness (δc) is defined as the distance above the electrode at which $C/C_\infty=0.90$. As the total current increases, the boundary layer thickness increases. For a free-convective flow field, the thickness of the boundary layer should be on the order of the wire diameter, as observed. Most importantly however, Figure 3.9 shows that the instrument is able to image reproducibly to within less than 100 μm of the electrode

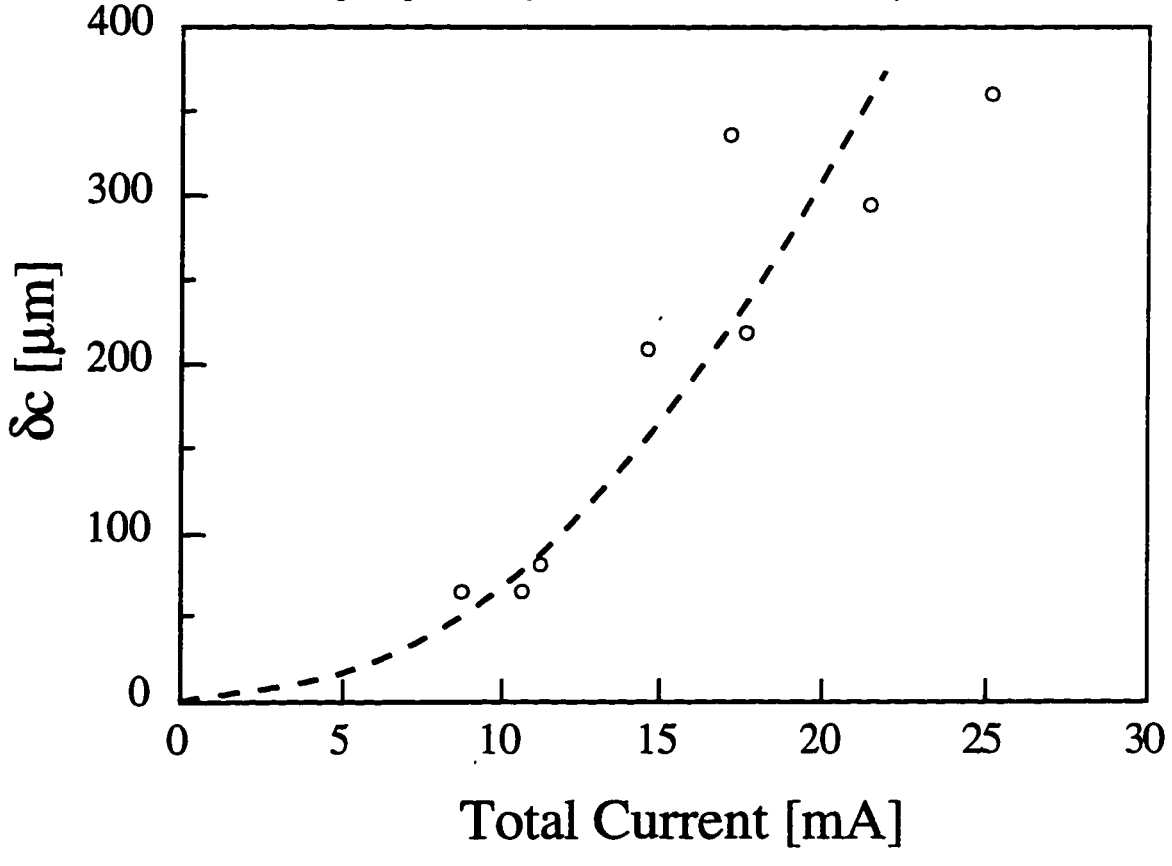

Figure 3.9. Concentration boundary layer thickness as a function of total cell current.

surface. The ability to image accurately within this lengthscale is necessary for the study of electrochemical systems in general.

Figure 3.10 shows how surface concentration at the top of the wire electrode is affected by total current passed through the cell. As expected, Figure 3.10 shows that the surface concentration decreases with increasing total current. Due to the fact that the surface concentration does not go to zero, we notice that even at the highest total current, the free-convection flow is not strong enough to place the cell into a mass-transfer limited regime.

These images are not corrected for optical refraction effects caused by a nonuniform index of refraction in the concentration boundary layer, a well known phenomenon in electrochemistry.[24,43-46] A completely quantitative profiling of solution species must account for this effect of index variation.

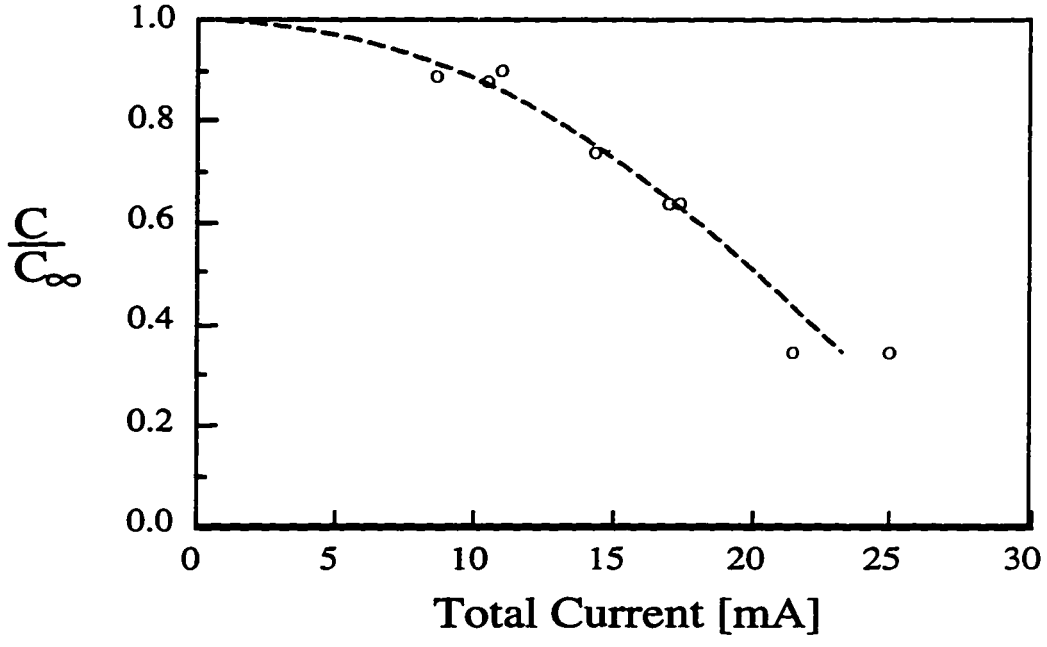

Figure 3.10. Surface concentration as a function of total cell current

3.3 Conclusions

From the above description of the design, construction and testing of our custom-built line-imaging Raman spectroscopy system we have shown that the instrument is able to resolve samples into one spectral dimension, and one spatial dimension with adequate resolution for studying electrochemical systems.

CHAPTER 4: AUTOMATED IMAGE BACKGROUND REMOVAL IN LINE-IMAGING RAMAN SPECTROSCOPY

4.1 Chapter Overview

Several automated image background removal schemes for use with line-imaging Raman spectroscopy are compared. An image of electrodeposited β-CuSCN produced by line-imaging Raman spectroscopy (one spectral dimension, one spatial dimension) is background-corrected by Adapted Pearson's Method (APM), a Fourier filtering method, and the mathematical morphology method of the rolling cylinder. APM is shown to perform best overall, but is the most computationally taxing due to the iterative nature of the algorithm. The effects of the APM parameters are discussed.

4.2 Introduction

Experimental techniques for imaging samples have become pervasive as array detectors, scanning probe microscopes, DSP hardware, and other technologies continue to improve and become more affordable. By adding one or two dimensions of spatial information to a Raman spectrum, for example, one can explore many more physical phenomena than with a point spectroscopy.[28-31,34,35,47] However, gaining the full value of an image normally requires careful analysis and manipulation of a large data matrix. Because of the matrix size, it is desirable to develop routine data analysis procedures (such as background removal) that are automated, and require little input from the experimentalist. Automated routines also tend to be more objective than those that require a high degree of user interaction, which is desirable when comparing processed images. The topic of image background removal or correction has recently been addressed for multispectral Auger microscopy,[48,49] electron energy loss spectroscopy and electron spectroscopic imaging,[50] scintigraphic imaging,[51] single-photon emission computed tomography,[52] scanning probe microscopy,[53-55] nuclear magnetic resonance,[56-58] X-ray

absorption fine structure,[59,60] and Raman spectroscopy.[61] Others report on general background correction schemes which may be applied to a number of spectroscopy types.[62-66]

Line-imaging Raman spectroscopy (LIRS) is emerging as a valuable spectroscopic tool for spatially probing the chemical state or composition of a sample along a focused laser line.[28-32,34,35,47,67] LIRS produces 2-D images in which one dimension represents spatial information and the orthogonal dimension represents spectral information. Because of the distinctly different information displayed in each dimension of a typical LIRS image, one normally observes structure within the image; this intrinsic image structure results from the orientation of the spectrograph slit (which defines the spatial direction) relative to the axes of the detector array. Since LIRS routinely produces images with very different characteristic lengths in each dimension, and obvious orientation, we call these anisotropic images. While any imaging technique can produce images with very different characteristic lengthscales, it is uncommon for the disparate lengthscales to be dictated by traits of the instrument (e.g., orientation of slits with respect to the detector) rather than characteristics of the sample itself. Anisotropic images that are processed by routines that do not accommodate anisotropy may distort the image in one dimension, or fail to properly correct one dimension for fear of distorting the other. Since anisotropic images are a routine feature of LIRS, we have found the need for a reliable, automated background removal scheme.

4.3 Image Acquisition, Characteristics, and Processing

The *in situ* images that we use to test various background removal schemes were acquired for our studies of thin film electrodeposition. The main image used in Figs. 4.1-5 was acquired immediately after electrodepositing a thin film of β-CuSCN onto a horizontal 500 μm diameter cylindrical electrode that was immersed in an aqueous-based electrolyte.

Raman scattered light from a vertical line bisecting the horizontal electrode was imaged onto the 100 μm entrance slit of an imaging spectrograph (SPEX model 270M). The vertical line of Raman scattered light (*i.e.*, the optical sampling volume) was then dispersed onto a 1024 x 256 (horizontal × vertical) pixel cryogenically cooled CCD array (Princeton Instruments). Image acquisition time was 9000s to achieve a very high signal to noise ratio. (Images can be collected with exposure times of 100s or less in some cases). The spectrograph slit was parallel to the 256 pixel dimension of the detector. Details of the experimental setup and instrument performance are reported in §3.2.1. We also present an image (Figure 4.6) acquired during the electrodeposition of copper from a binary copper sulfate electrolyte. The imaging geometry was identical to that described above, but in this case an electrolyte flow was impinging on the bottom of the electrode, leading to an asymmetric copper(II) and sulfate electrolyte composition profile. In this case the image acquisition time was 90s. Both "raw" images had signal from cosmic rays (which can saturate individual CCD array elements) extracted using a 2nd rank median filter, but no dark signal was removed. A 2nd rank median filter is analogous to a 5-point moving average filter except the median rather than the mean is used.

Figure 4.1(a) is the image that results from the β-CuSCN electrodeposition experiments outlined above and detailed in Chapter 3. In Figure 4.1, the abscissa is the spectral dimension with prominent vibrational modes labeled underneath. The ordinate is the spatial dimension. The optical sampling volume includes electrolyte solution above and below the wire, as well as the wire itself. The dimensions of the optical sampling volume are dictated by the slit width, detector height, and depth of field of the collection optics. The diameter of the wire is marked by horizontal dotted lines across the image. The spatial resolution of this image is approximately 5 μm, and has a spectral slitwidth of 8 cm^{-1}.

The image in Figure 4.1 was chosen because it contains a variety of spectroscopic and spatially varying features, thus providing a good test image for various background removal schemes. The spatial range includes positions above and below the wire where Raman signal mainly from water is present and regions of wire surface where Raman signal originates mainly from β-CuSCN. The spectral range encompasses both the strong Raman water band centered near the symmetric ν_1 stretch (3450 cm^{-1}), and the much weaker asymmetric ν_2 stretch (1645 cm^{-1}). The weak ν_2 peak is located near the edge of the image adding an additional degree of difficulty to the removal methods. These signals offer a wide dynamic range in intensity and wavenumber shift. In addition to having nearly three hundred times the intensity of the ν_2 mode, the band centered near the ν_1 mode has a FWHM of roughly three and a half times that of the ν_2 mode.

Three methods of background removal were compared: high-pass Fourier filtering (1-D method),[68] rolling cylinder method,[55,65,68] and an adapted version of a single-spectrum baseline removal method originally suggested by Pearson,[66] which we refer to as Adapted Pearson's Method (APM). The methods can be broken down into two classes, those that operate on the 2-D image data matrix directly (rolling cylinder) and those that perform consecutive 1-D row-by-row processing (FFT and APM). All background subtraction routines were implemented on a Macintosh Centris 650 (25 MHz 68040) computer. For the Adapted Pearson's Method (APM) and Fourier background subtraction schemes, custom programs were written in LabView.™ The rolling cylinder method was implemented using NIH-Image 1.59.† The image dimensions are 256 rows (spatial dimension) and 614 columns (spectral dimension); 205 columns were removed from each edge of the original 1024 column image because there was no useful spectroscopic

† This widely used image processing and visualization program is in the public domain and available via anonymous ftp at ftp://zippy.nimh.gov.

information contained in those locations. Each spectral row was zero-padded to 2048 pixels for the Fourier method.

4.4 Results and Discussion

4.4.1 Image comparison.

Figure 4.1 shows a comparison of the image with background removed by the methods noted above. The color scale is linear and the same for all images. The abscissa in all images is Raman shift (cm^{-1}) and the ordinate is spatial position (μm). The strong signal spanning the image vertically on the left side is the Raman band of water centered near the ν_1 stretch at 3450 cm^{-1}. To the right are two vertically aligned dots at the top and bottom of the wire surface originating from the CN stretch (2175 cm^{-1}) of the electrodeposited β-CuSCN. The ν_2 bending mode of water at 1645 cm^{-1} is visible to varying degrees as a thin faint vertical line on the right-hand side of the images. The region of low intensity spanning the image horizontally is due to the portion of the optical sampling volume located "within" the wire electrode. (*c.f.* Chapter 3).

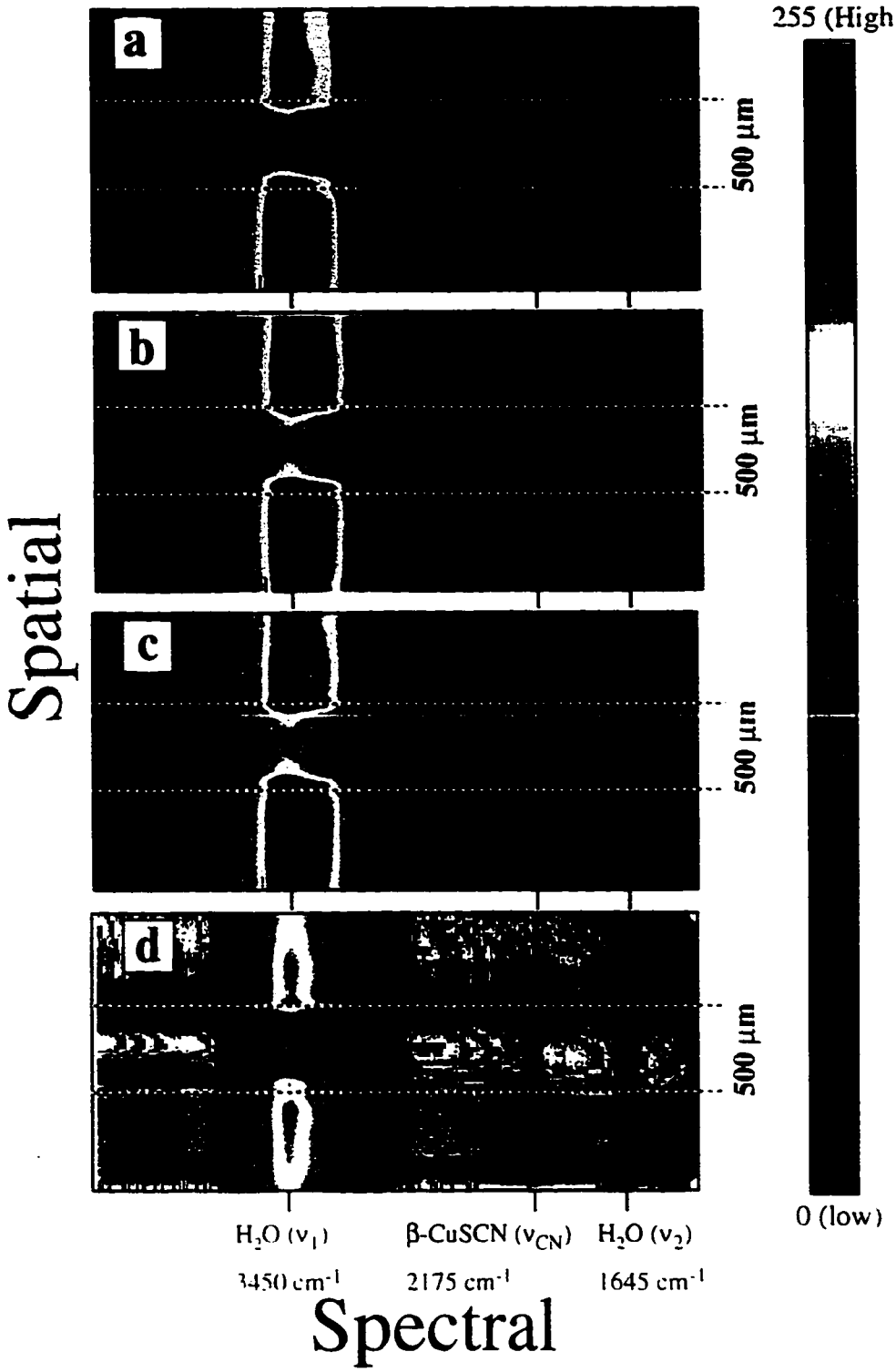

Figure 4.1. A comparison of processed images (all with identical color maps). The different baseline removal schemes used to flatten the image are: (a) raw image, (b) adapted Pearson's method (APM), (c) Fourier high pass cut-off filter, and (d) rolling cylinder method. The abscissa in all images is Raman shift (cm^{-1}), and the ordinate is spatial position (5 µm spatial resolution).

In Figure 4.1(a), the uncorrected image, the top half of the image is seen to have a slightly lower intensity than the bottom half, especially in the strong water band, and slight background aberrations can be seen. The weak Raman ν_2 water mode can be seen, but this signal is of the same order as the background, so this feature appears distorted. Background variation is greatest in all the corners of the image but the upper left. The image as a whole has a high signal-to-noise ratio; therefore, background variations are not due to noise, but rather to other sources such as stray light, nonuniform detector efficiency, aberrations in the optical train, fluorescence or others. Properly corrected, this image should show a uniform background intensity (color) with spectral features retained and undistorted. The specific color of the background is not as important as its uniformity.

Figure 4.1(b) shows the image background corrected with APM. APM is our adaptation of Pearson's algorithm for separating background points from spectral features. The basic approach taken by Pearson can be summarized as follows.[66]

> "A point in a digitized spectrum, $Y(x_i)$, is considered to be part of the baseline if and only if it lies within $\pm v\sigma$ of the X-axis, where **v** is a positive constant and σ is a 'baseline standard deviation.' A 'baseline standard deviation' is the self-consistent limit obtained by iteratively calculating the standard deviation of the Y values of all data points which lie within $\pm u\sigma$ of the X-axis, where **u** is another positive constant which need not be equal to **v**."

A smooth curve, g(x), is drawn using the selected "baseline" points found using the algorithm outlined above. The function g(x) is then subtracted from the spectrum, and the next iteration begins. The only requirement of the baseline basis function, g(x), is that it not be capable of describing wanted signal. As the algorithm iterates, the processed spectrum becomes flattened because only points within a certain standard deviation from

the baseline are used to draw the smooth curve. Here, the idea is essentially to iteratively throw out the outliers (Raman signal) of a smooth curve (background) drawn through dynamically defined points ($\pm v\sigma$) taken from a dynamically defined set of points ($\pm u\sigma$), where the smooth curve is incapable of describing wanted signal. Our laboratory uses a third-order basis function (first four Legendre polynomials) as the basis function, g(x). Our convergence criteria follow that of Pearson, namely a negligible correction is when $|g(x)|<0.12\sigma$ for all x.

The routine as laid out by Pearson can be used sequentially on each spectrum (*i.e.*, each row in the 2-D image matrix) of a Raman image with good results, but treating each spectrum as independent is not the best use of computational resources. In fact doing so can lead to image background correction times on the order of several hours. To increase efficiency, information gained in the previously processed spectrum should be applied to the current spectrum being processed. Therefore, the converged baseline determined from the previous spectrum is initially subtracted from the current spectrum being processed; this normally is a very good guess for the baseline of the current spectrum. In addition, the baseline standard deviation (σ) from the most recently converged row is also passed to the next spectrum. For spectra where the previous baseline is an excellent first guess, only one or two iterations are required before convergence. However, passing a previous value of σ introduces the possibility of passing too small of a σ, and the routine is not able to find a suitable number of points from which to draw a smooth curve, *i.e.* fails. To overcome this problem, all of the points in a given spectrum are used if the algorithm fails in this manner. Using all the points after a failed first iteration provides as much stability as would be achieved if each spectrum were processed independently, but results in fewer iterations overall. This is the current implementation of the APM background removal scheme. See Diagram 1 for a schematic of the APM algorithm.

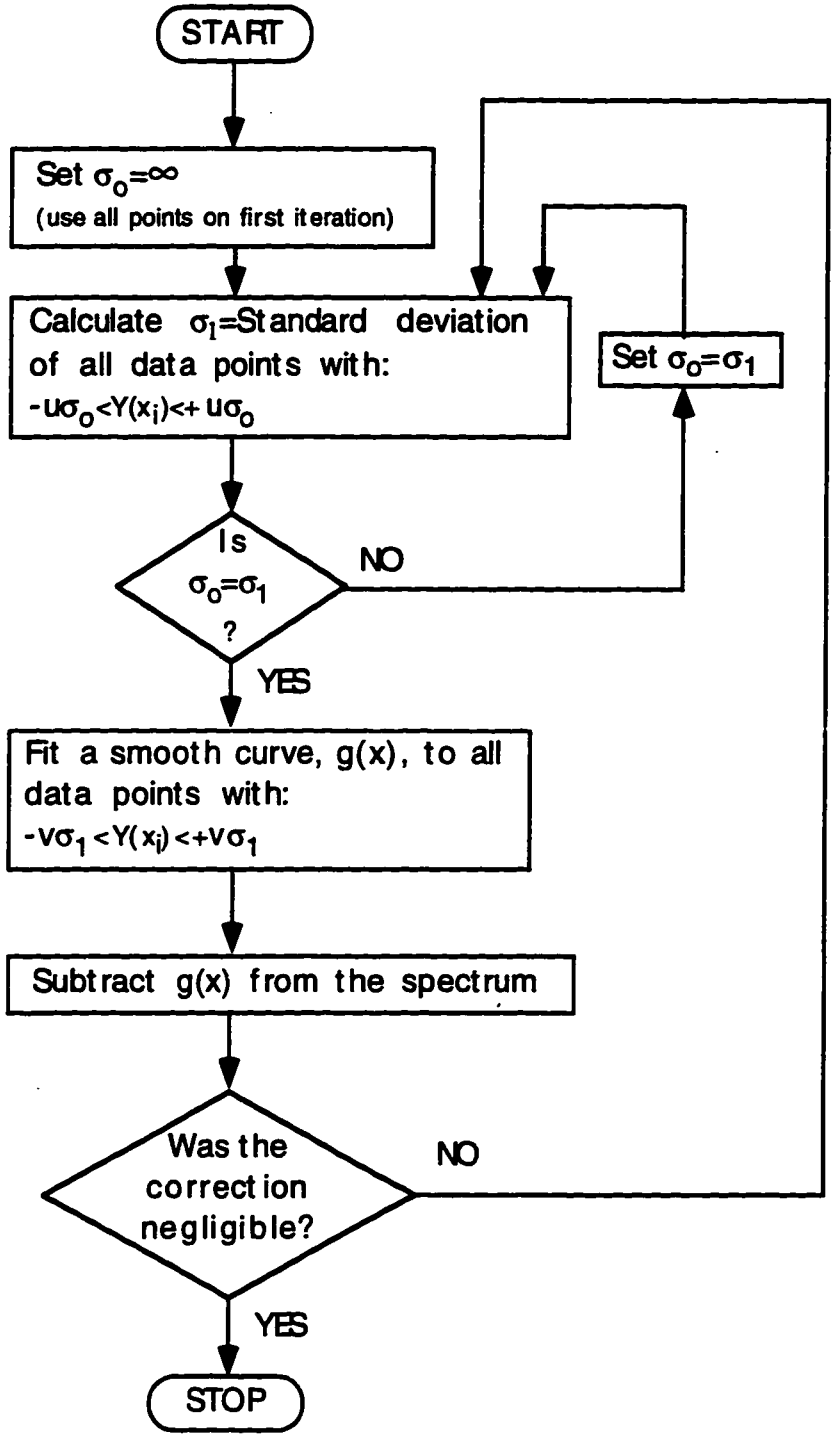

Diagram 1. Schematic of the APM algorithm. Where: $Y_k(x_i)$ is a point in a digitized spectrum at the kth iteration, v and u are positive constants, and σ is a baseline standard deviation.

Under the optimized conditions shown in Figure 4.1(b) (**u**=2.75, **v**=1.25), the background displays a uniform color, and the corner aberrations have been nearly completely eliminated. Only in the extreme right-hand corners can slight residual background fluctuations be seen. Also visible due to background removal, is the weak ν_2 Raman mode of water appearing as a uniform light blue vertical band on the right side of the image. To use APM, the operator must define the basis function g(x) and assign appropriate values for the parameters **u** and **v**; we have found this to be straightforward and leads to a robust algorithm with minimal intervention from the operator. Figure 4.1(b) took 746 seconds to process.

Figure 4.1(c) shows the image background corrected using a Fourier filtering method. Fourier transform methods are used extensively in image processing. A thorough discussion can be found in the text by Russ.[68] One dimensional Fourier filtering requires the operator to define a filter mask that is appropriate for the spectral dimension of the image. The Fourier filter is then run sequentially row-by-row through the image. Since Fourier transforms are linear operations, the filtering procedure is noniterative and fast. In Figure 4.1(c), we used a high pass cut-off filter that set the DC and lowest frequency component of the transformed image to zero. Rather than being flattened, some variations have been added to the image. Fluctuation can be seen in both the spectral and spatial directions. In fact, the low intensity horizontal band has been raised slightly relative to the surrounding areas. The right-hand side of the image shows this side has also been raised. This fluctuation is caused by our use of a sharp cut-off filter rather than a gradual filter mask, and as a consequence, the filter overcompensates in removing low frequency fluctuations. One could probably determine a better FFT high-pass filter that would not overcorrect the baseline, but this procedure is fairly image specific and requires significant operator input. Figure 4.1(c) took 101 seconds to process.

Figure 4.1(d) shows the image corrected by the rolling cylinder method. The rolling cylinder method, unlike Fourier methods, is nonlinear and cannot be described as a convolution operation. Instead of processing the image in terms of component frequencies, this algorithm uses the mathematical morphology opening operation using a cylindrical structuring element. More detailed explanations and applications are given elsewhere.[53,55,65] In descriptive terms, the rolling cylinder operation can be thought of as rolling a cylinder of specified radius along the underside of an image.[53] The background is mapped by the top of the cylinder as it rolls under every point in the original image. With the proper choice of radius, features which are too sharp for the structuring element to enter (Raman peaks) are retained, while smooth background fluctuations are traced by the structuring element, and removed. In the case shown here, the axis of the cylinder is parallel to the spatial direction of the image, so the spectral background is removed and relative intensity differences in the spatial direction are left intact.

A radius of 200 pixels was used for the cylinder element, which is roughly 25% larger than the ≈150 pixel wide spectral base of the strong water band. This prevents the structuring element from entering the large water feature and corrupting it, but allows smooth background fluctuations to be removed. Figure 4.1(d) shows uniform residual background with no distortion of the spectral features. The image rests on the bottom of the color scale, and the white specks are indicative of only a single count variation in the color table from 0 (white) to 1 (purple). As is the case with the other images, some

Table I: Image background removal times in seconds for the rolling cylinder method as a function of radius in pixels.

Rolling Cylinder	11	22	34	47
radius	50	100	150	200

background distortion still exists in the right-hand corners. These distortions are smaller than in the Fourier method, but not as small as with APM. Table I summarizes the time required to process the image with this method as a function of cylinder radius.

4.4.2 Spatial and spectral cross-sections

Although images allow one to capture many features that can lead to a greater understanding of the underlying phenomena, looking at image cross-sections provides a more quantitative perspective. Three separate cross-sections, one spectral and two spatial, were taken of each of the background-corrected images. The image was acquired with 16 bits and all processing retained this level of information. The image display and analysis software, NIH-Image, only displays the image in 8 bit depth however. Cross-sections taken from the image processed with this software (rolling cylinder) show the resulting 8-bit discretization.

Figure 4.2 shows spectral cross-sections taken from the electrode surface showing a traditional Raman spectrum of the water modes and the CN stretch of the electrodeposited β-CuSCN thin film. Figure 4.2(a) is the uncorrected spectrum shown full scale with peak assignments. Figure 4.2 (b) and Figure 4.2 (c) are enlarged near the baseline so differences in correction may be noted. Figure 4.2 (b) shows the performance of APM. The method retains spectral information and allows the ν_2 water peak to emerge from the background. On the left side, the baseline has been flattened, although the right side has not been completely corrected. Taking the large dynamic range of the spectrum into account though, this deviation is small.

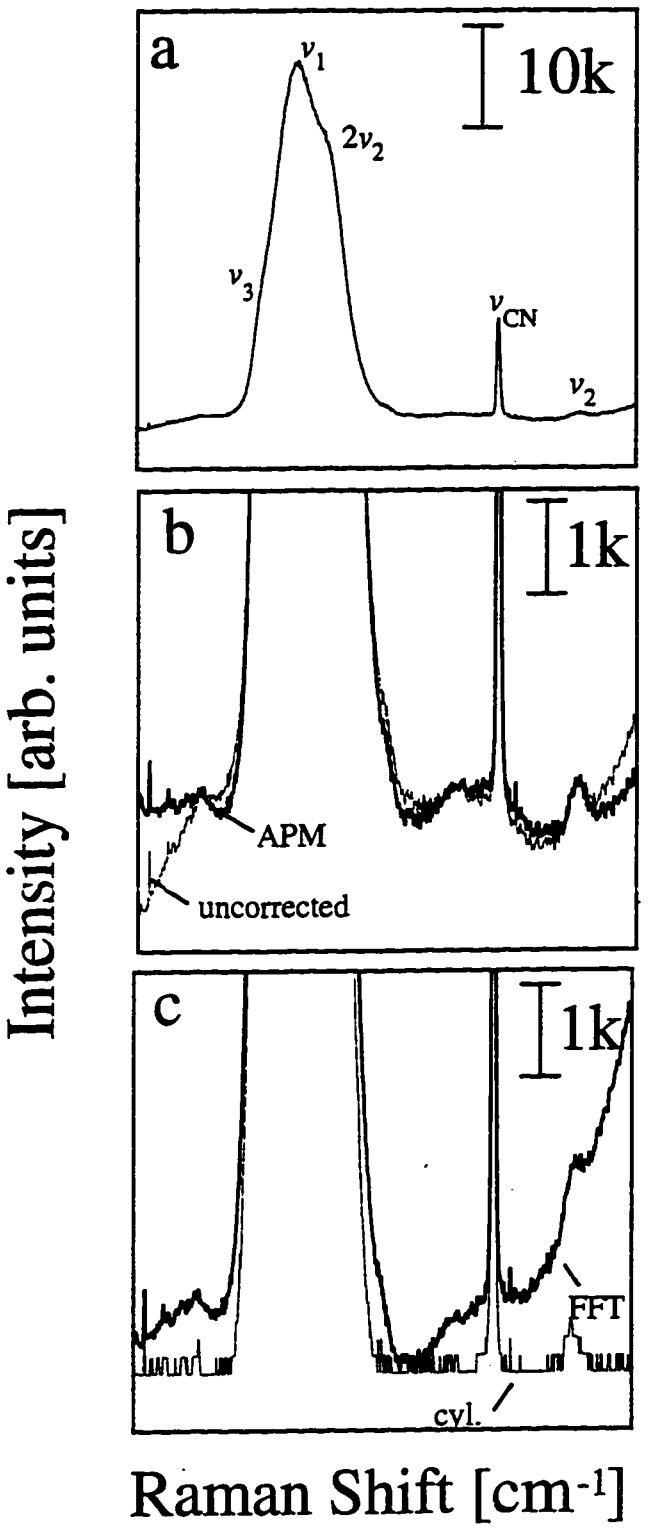

Figure 4.2. Comparison of spectral cross-sections taken from Figure 4.1 at the electrode surface. The spectra show the Raman modes $\nu 3$, $\nu 1$, $2\nu 2$, and $\nu 2$ of water at 3630, 3450, 3225 and 1645 cm^{-1}, respectively. The peak labeled νCN corresponds to the CN stretch (2175 cm^{-1}) of the electrochemically deposited β-CuSCN thin film. Labels on each curve denote the baseline removal method used.

Figure 4.2 (c) shows the results of the Fourier and rolling cylinder methods. As seen in the Fourier corrected image (Figure 4.1 (c)), the right side has been over-corrected and diverges sharply upward concealing the ν_2 signal. The rolling cylinder method performs very well as a baseline removal algorithm, even near the edge where the ν_2 water mode has emerged and rests on a flat baseline. The method still shows slight divergence in the corners of the image.

A successful background removal method for anisotropic LIRS images must perform well in both the spatial and spectral dimensions of the image. Figure 4.3 shows a comparison of spatial cross-sections through the strong ν_1 Raman mode of water located at 3450 cm^{-1}. The abscissa in these cross-sections is spatial distance with the left side corresponding to the top of the images as shown in Figure 4.1. Since water concentration is spatially uniform, the Raman intensity should be uniform as well. Deviations from a uniform spatial signal occur due to background variations, Gaussian laser intensity profile along the imaging line, shape of the optical sampling volume and optical effects at the edge of the wire due to the coherent light source. The most obvious feature is the center region where the signal drops off sharply due to the portion of the optical sampling volume that bisects the wire electrode. To either side of this center trough is a local rise and fall in intensity that is likely due to optical interference effects near the electrode surface.[30] The focused imaging line is centered at the center of the wire, and the Gaussian intensity profile can be seen as a general intensity decrease moving away from the center of the cross-sections. Background fluctuation causes the right-hand side to be higher than the left, perhaps due to stray light.

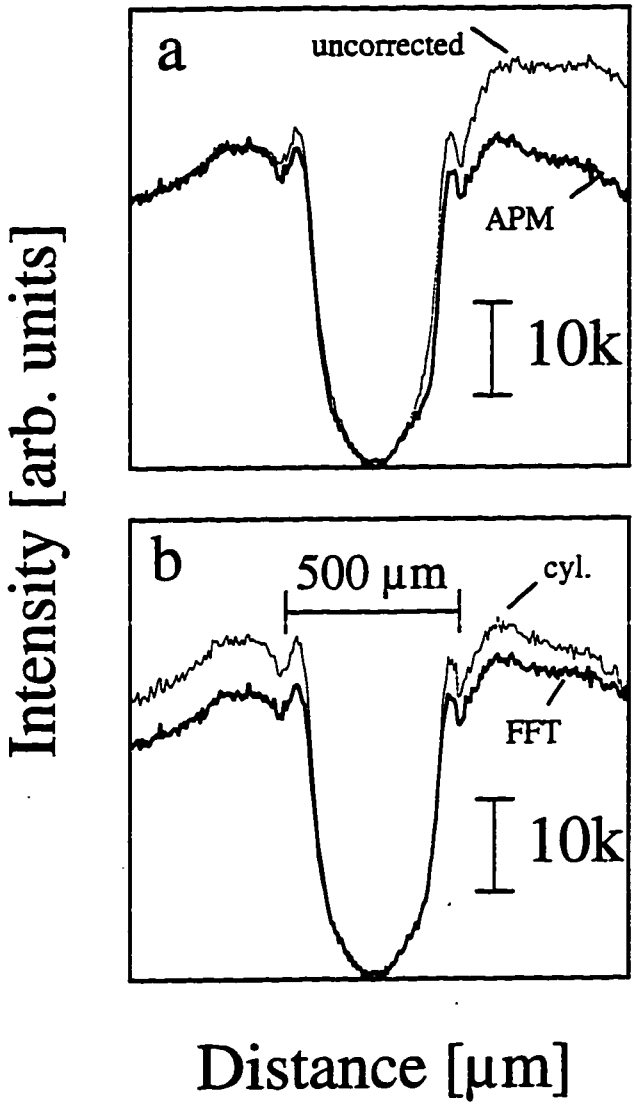

Figure 4.3. Comparison of spatial cross-sections taken from Figure 4.1 at the strong ν_1 (3450 cm^{-1}) Raman mode of water. Labels on each curve denote the baseline removal method used.

Figure 4.3(a) compares the ν_1 spatial cross-section of the uncorrected image to the APM-corrected image cross-section. On the left, APM correctly follows the original signal. On the right, APM has flattened the background yielding a symmetric cross-section while maintaining the Gaussian intensity profile, center trough and coherence ripples. The Fourier curve (Figure 4.3 (b)) shows similar correction as the APM curve; however, below it is shown that this method performs poorly at the much weaker water ν_2 Raman signal cross-section. The rolling cylinder method also performs rather well in the spatial direction. Similar to the APM correction, the desired spatial features are retained, and the background fluctuations removed. Only slight differences between the two curves can be seen.

Figure 4.4 shows spatial cross-sections through the weak ν_2 Raman mode of water at 1645 cm^{-1}. This Raman mode is roughly two orders of magnitude weaker than the ν_1 mode as shown in these images. With this signal, removing the background while retaining spectral features becomes more of a challenge, and is a revealing measure of background removal method performance. Figure 4.4 (a) shows the uncorrected and APM corrected cross-sections. The ν_2 spatial profile should be identical to the stronger ν_1 profile, but before background removal, Raman features are concealed by the background. Notice the intensity scale is fifty times greater than the corrected ν_1 cross-section. It can be seen that APM does a very good job of removing the background fluctuation without corrupting the true spatial features. The Gaussian laser profile is seen, as well as a small trough and coherence ripples.

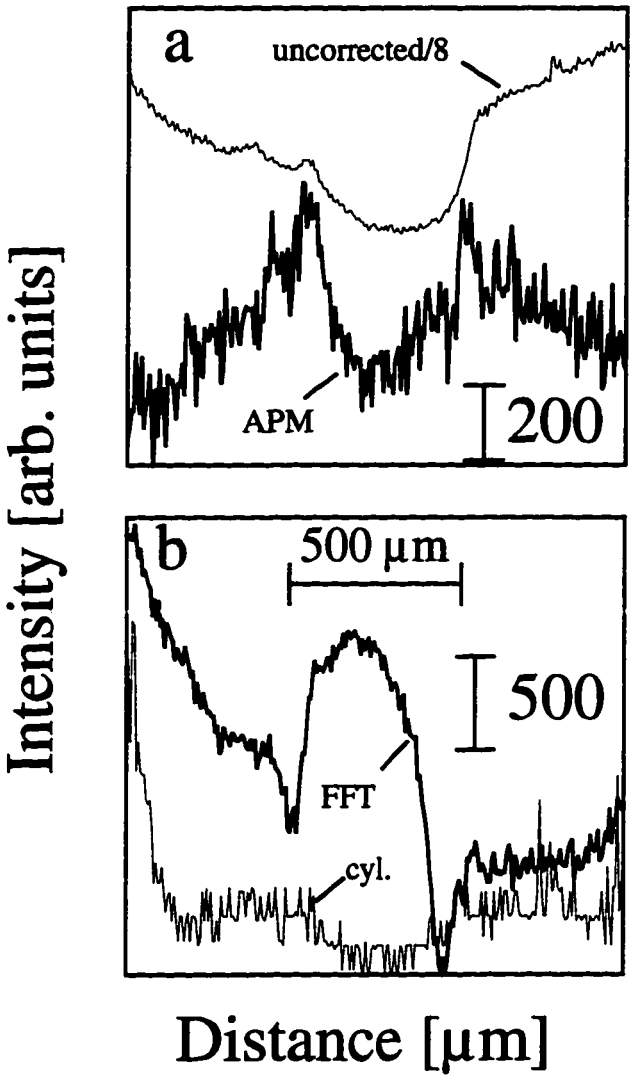

Figure 4.4. Comparison of spatial cross-sections taken from Figure 4.1 at the weak v2 (1645 cm^{-1}) Raman mode of water. Labels on each curve denote the baseline removal method used.

The Fourier method is seen to perform rather poorly. The center trough appears to actually have been inverted, and no authentic spatial features can be seen. Without the self-correcting nature of an iterative method (as in APM), the Fourier filter mask must be good enough to correct the entire image in a single pass. Although this is obviously desirable from a computational standpoint, satisfying this constraint in a general automated routine is formidable.

The rolling cylinder method performs well, although diverges upward on the left side of the cross-section. Spatial features are nevertheless seen, including a shallow low-intensity trough. If not for the divergence at the edges, this method would be comparable to APM.

4.4.3 Effect of the APM parameters u and v.

The adapted Pearson method described above is the best performing technique we have found for removing background from anisotropic LIRS images in an automated fashion. Because of this, we now discuss the role of the parameters **u** and **v** on the performance and robustness of this method. The specific values of the APM parameters have two main effects: convergence time and stiffness of the baseline fit. The effect on convergence can be viewed in two main ways: total time to remove the background, and total number of iterations required to remove the background. The total time metric is dependent on the particular computational resources used, and absolute values are not as meaningful as the relative time between combinations.

Table II shows the total time required to correct the image for various combinations of **u** and **v**. For most combinations, correction times were on the order of 700 or 800 seconds. Although when **u** was lowered to 2.0 or less, for all values of **v**, APM failed to converge within 20 iterations, and is marked as a failure (F) in the table. The exception is the case of both **u** and **v** equal to 1.0, which took an excessive amount of time and many iterations. Although it did not technically fail, its background removal performance can be achieved with other combinations having better time and iterations scores. Its convergence is most likely due to the particular attributes of this image. This **u**, **v** combination is not a stable combination. Along the **u=v** diagonal, where the baseline fit is the stiffest, performance is poorest. The specific case of **u=v=2.5** will be discussed below.

Table II: APM background removal time in seconds as a function of the parameters **u** and **v**. "F" indicates failure of any one spectral row to converge within 20 iterations.

u \ **v**	1.0	1.5	2.0	2.5	3.0	3.5
4.0	711	738	770	821	833	832
3.5	712	739	772	822	836	
3.0	784	757	786	822		
2.5	755	773	875	3733		
2.0	F	F	F			
1.5	F	F				
1.0	1214					

APM necessarily requires at least one iteration per spectral row (i.e. at least a single pass). It is more revealing to look at correction performance in terms of the number of iterations in excess of this base number. Table III shows the number of excess iterations for the same parameter combinations as in Table II. For most combinations of the parameters, all the excess iterations occur in the first spectral row. After the baseline of the first spectral row has been determined, only a single pass is required for subsequent spectral rows in the rest of the image. For other combinations of the parameters with

Table III: APM background removal excess iterations as a function of the parameters **u** and **v**. "F" indicates failure of any one spectral row to converge within 20 iterations.

u \ **v**	1.0	1.5	2.0	2.5	3.0	3.5
4.0	4	3	4	2	1	1
3.5	4	3	4	2	1	
3.0	12	12	11	2		
2.5	15	13	50	1229		
2.0	F	F	F			
1.5	F	F				
1.0	492					

mostly smaller, similar-valued combinations (e.g. 1:1, 2.5:2.5), the highest number of excess iterations can be found. Smaller values of **u** and **v** lead to poorer performance due to the fact that fewer points are chosen per iteration than for greater values. Especially for spectra with low signal to noise ratios, a smaller sampling of points leads to greater variance in the baseline fit, and causes APM to require more iterations.

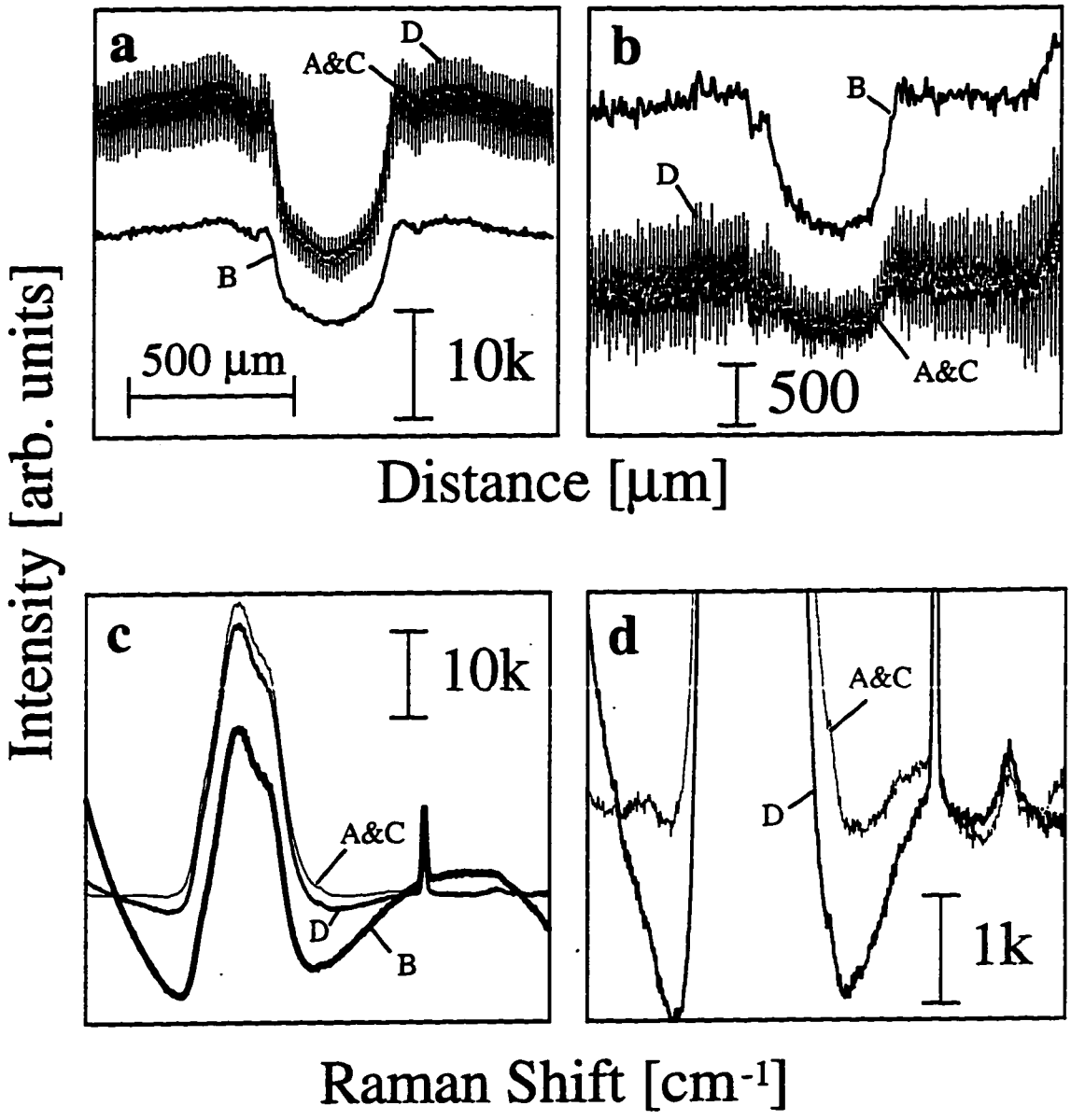

Figure 4.5. Spatial and spectral image cross-sections showing the effect of the APM parameters **u** and **v** on the processing of Figure 4.1(a) **A**:u=4.0, v=1.0; **B**:u=4.0, v=3.5; **C**:u=2.5, v=1.0; **D**:u=2.5, v=2.5.

4.4.4 APM cross-sections.

Figure 4.5 shows the effect of the APM parameters on the cross-sections of the image. Four combinations of **u** and **v** are shown. Values roughly map out the extremes of Table II and Table III. Figure 4.5(a) and Figure 4.5(b) show the spatial cross-sections through the ν_1 and ν_2 Raman modes of water, respectively. Figure 4.5(c) shows the complete Raman spectral cross-section at the electrode surface, and Figure 4.5(d) shows the spectra enlarged near the baseline.

In the spatial cross-sections, all the curves (A-D) qualitatively have the same shape. Curves A and C are essentially identical. These curves share the value of **v**=1.0 in common. Curve D is the case where **u**=**v**=2.5, and can be seen to follow the same general trend, but oscillates about curves A and C. This oscillatory behavior is a result of making the point-finding routine in APM rather stiff. As a direct result of this oscillatory behavior, the measures of performance shown in Table II and Table III for this are also very poor. The spatial cross-sections of curve B qualitatively appear good, although in Figure 4.5(a), curve B appears below the other curves while in Figure 4.5(b), it appears above. The reason for this is seen in Figure 4.5(c). Here, **v** is set too high (**v**=3.5), and the spectral correction diverges. If **v** is set too high, many points (including Raman features) are selected as baseline points, causing the fitted curve to pull the spectral features down, and the overall correction to diverge. Curves A, C, and D all have smaller values of **v**. Curve D, whose **v** is only slightly lower (**v**=2.5), diverges slightly on the left-hand side, but performs better than curves A and C do on the right-hand side. This difference can more easily be seen in Figure 4.5(d). We have found values of **u**=2.75 and **v**=1.25 to be good APM parameters.

To consider the robustness of using APM parameters set to **u**=2.75 and **v**=1.25, we show results for a rather different image from our research. Figure 4.6(a) is the raw

image that results from using LIRS to monitor the electrodeposition of copper from a binary copper sulfate bath flowing around a 500 μm diameter wire electrode (*c.f.* Chapter 3). Several features are apparent in the uncorrected image: the vertical line of the symmetric sulfate stretching mode (983cm^{-1}), the weak Raman signal from the ν_2 water band (1645 cm^{-1}), and the attenuated band spanning the image horizontally. The darker regions on the left-hand side of the image indicate a gradual rise in the background, which obscures the ν_2 water band.

Figure 4.6(b) shows the background-corrected image using APM with **u**=2.75 and **v**=1.25. We see the image is flat, and has a smooth background without any further optimization of the parameters. The background slope has been removed, allowing the ν_2 water band to be seen.

A feature not readily seen in the uncorrected image but revealed in the corrected image is a series of dot pairs appearing at the top and bottom wire surfaces. The plasma-line filter (optical narrow bandpass) was removed from the optical train allowing plasma lines to strike the sample. Since laser plasma emissions are very weak, only elastically scattered light from the surface regions in the optical sampling volume are detected. This elastic scattering gives rise to "surrogate" surface species seen as dot pairs at the wire surface. (These plasma lines can be used to precisely determine the boundary between surface and solution, as well as spectral calibration points.) Although the plasma emissions can be seen in the uncorrected image when one looks at each spectral row individually, only after background removal are they visible in the image.

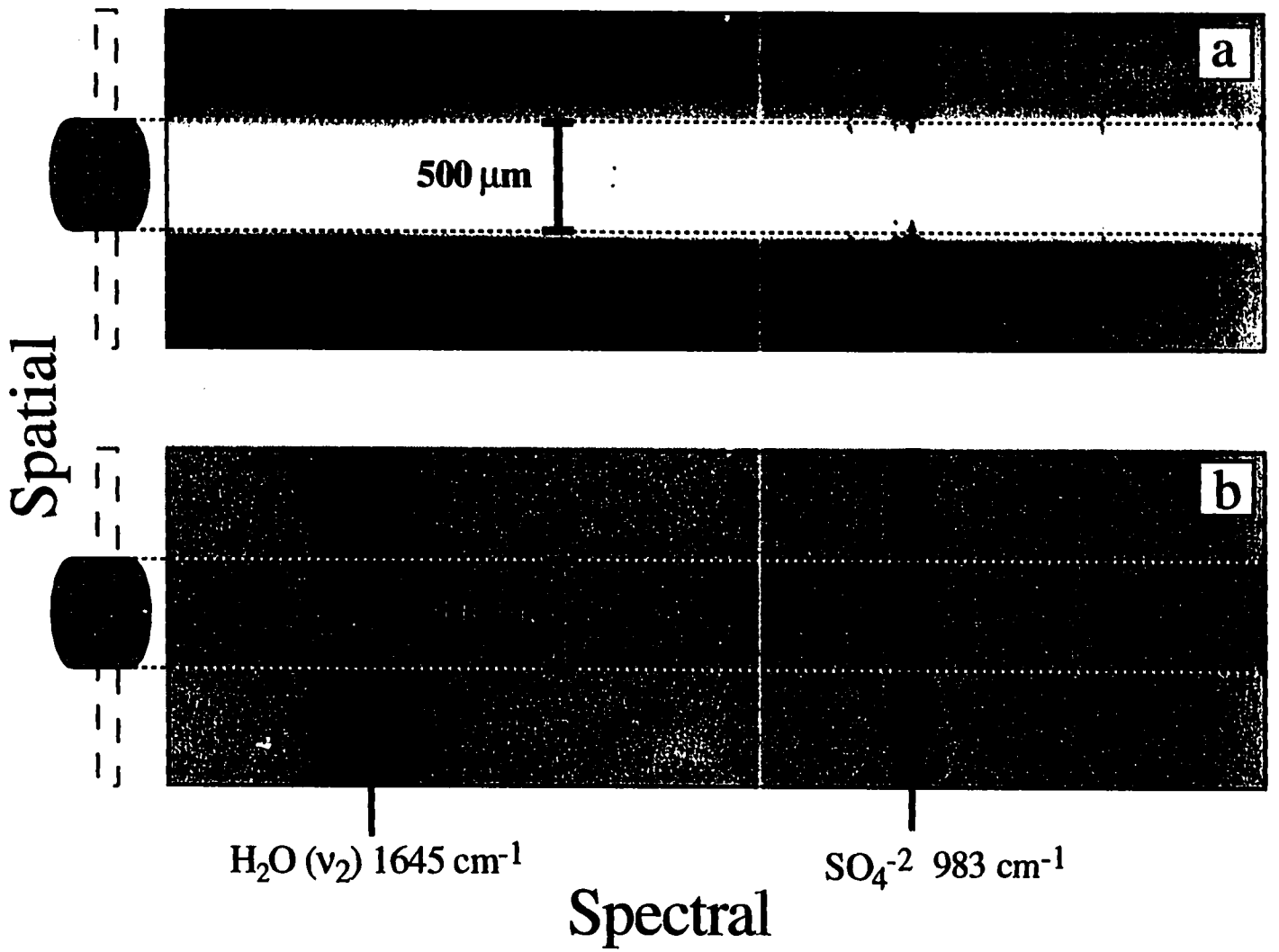

Figure 4.6. The raw (a) and processed (b) LIRS images acquired during the electrodeposition of copper from a copper sulfate binary electrolyte. Baseline removal was performed with APM using **u**=2.75 and **v**=1.25. The electrode location and imaging region are shown schematically on the left hand side of each image.

Small spatial intensity variations in the sulfate mode are present above and below the electrode surface in the corrected image. This image, like the previous images, has not been corrected for nonuniform laser intensity, coherent optical effects, or other aspects along the imaging line. Using standards such as the spatial profile of the strong ν_1 water mode, or the sulfate in an unreacting case, we have been able to normalize corrected images and directly image concentration profiles during copper electrodeposition.

4.5 Conclusions

We have compared three baseline removal routines, and evaluated their use in automated image background removal for anisotropic images acquired using line-imaging Raman spectroscopy. Since the characteristic lengths of the features in each dimension of the image are different, an automated method must be able to remove underlying baseline variation while preserving the anisotropic features. Adapted Pearson's Method, APM, is described and shown to behave very well in an automated background removal scheme. A commonly available mathematical morphological operation (rolling cylinder) performs very well also, but tends to have slight divergence problems at the image corners. APM does not show deviations at the corners, but it is the most computationally intensive routine tested. A basic Fourier filtering method is shown to be fast, but not especially effective for dimensionally anisotropic images, at least in the simple form tested here. We currently use APM as our routine, automated method of background removal from images generated using LIRS to study thin film electrodeposition. In general, we have found for the anisotropic LIRS images we generate, the values of **u**=2.75 and **v**=1.25 lead to a robust method for performing automated baseline removal.

CHAPTER 5: USING LINE-IMAGING RAMAN SPECTROSCOPY WITH MULTIVARIATE CALIBRATION FOR *IN SITU* OXIDATION STATE PROFILING

5.1 Chapter Overview

Reported is the use of line-imaging Raman spectroscopy for the *in situ* determination of oxidation state profiles in nickel hexacyanoferrate derivatized electrodes under potential control in an electrochemical cell. Line-imaging Raman spectroscopy is used to collect 256 contiguous Raman spectra every ≈5 μm from thin films (*ca.* 80 nm) formed by electrochemical derivatization of nickel electrodes. The cyanide stretching region of the Raman spectrum of the film is shown to be sensitive to iron oxidation state and is modeled by both univariate and multivariate correlations. Although both correlations fit the calibration set well, the multivariate (principal component regression or PCR) model's predictions of oxidation state are less sensitive to noise in the spectrum, yielding a much smoother oxidation state profile than the univariate model. Oxidation state profiles with spatial resolution of approximately 5 μm are shown for a nickel hexacyanoferrate derivatized electrode in reduced, intermediate, and oxidized states.

5.2 Introduction

Metal hexacyanoferrate compounds show promise as electrochemically switchable ion exchange materials for use in the clean-up of radioactive wastes such as those found in storage basins and underground tanks at the Department of Energy's Hanford Nuclear Reservation.[6] The selectivity of nickel hexacyanoferrate for reversibly absorbing Cs^+ over other group 1A cations[9,12,69] is of particular importance because separating $^{137}Cs^+$ from these wastes is an essential step in a cost-effective clean-up strategy. Nickel electrodes derivatized in the presence of ferricyanide form a thin film of nickel hexacyanoferrate on the surface.[8] Nickel hexacyanoferrate is the nickel analog of Prussian blue (iron

hexacyanoferrate). Cationic exchange takes place in the film electrochemically via the solid-state redox reaction

$$A_{2-x}Ni^{II}Fe^{II+x}(CN)_6 + xA^+ + xe^- \rightleftharpoons A_2Ni^{II}Fe^{II}(CN)_6 \qquad (5.1)$$

where A is the cation and x is the fractional oxidation state (or degree of oxidation) of the derivatized film ($0 \leq x \leq 1$).

Although the stability and cation exchange properties of nickel hexacyanoferrate have been demonstrated,[8,9,12] more work is needed to determine the relationships between the formation, structure, cation exchange capacity and process cycle life of the material. In particular, the cation exchange capacity of the film decreases over many oxidation and reduction cycles, but the exact mechanism for this degradation is unclear. Sinha *et al.* note that the cycle life of these materials can extend to >18000 cycles with only a 10% capacity loss when a small amount of $Fe(CN)_6^{-3}$ is added to the electrolyte.[7] Without this addition, the film can lose ≈50% of its capacity after 3000 cycles. This degradation behavior is attributed to a competition between ferricyanide ion and oxide formation, suggesting that capacity loss is in part chemical in nature. Since the ion exchange properties are directly linked to the oxidation state of the iron in the material, profiles of oxidation state in these films may lead to a greater understanding of ion exchange behavior. The thrust of the work reported here is the characterization of line-imaging Raman spectroscopy as an *in situ* tool for spatially profiling the oxidation state of nickel hexacyanoferrate derivatized electrodes.

Non-destructive *in situ* profiling of oxidation state of thin films is generally difficult for electrochemical systems where the film is immersed in an aqueous medium. Electron spectroscopies are not suitable for use as *in situ* probes of oxidation state because of the immersed interface, so one normally relies on optical probes of vibrational,[70,71] electronic,[3,11,72,73] and core level states.[74] Raman spectroscopy is particularly well suited for *in situ* studies of nickel hexacyanoferrate derivatized surfaces because cyanide (CN)

stretching modes have large Raman scattering cross-sections and the vibrational frequency of CN is known to increase appreciably with the oxidation state of a coordinating metal atom.[75,76] To obtain a spatially resolved oxidation state profile of a derivatized surface, one must analyze Raman spectra from different regions of the surface. Line-imaging Raman spectroscopy is a technique that simultaneously collects a contiguous series of Raman spectra from a long, thin laser line used to illuminate the sample, thereby providing spectroscopic and spatial information in a single exposure. The data set acquired in a line-imaging Raman spectroscopy experiment contains spectroscopic and spatial information that is conveniently displayed as a two dimensional image possessing one spectral axis and one spatial axis, and a gray or color scale that indicates signal intensity. Recently line-imaging Raman has been used to study mass transfer in microdroplet streams,[34] to spatially profile temperature and chemical species in hydrogen flames,[31] to create spatial maps of chemical variation in composite materials,[37,77] and to identify surface and solution species in an electrochemical system.[47]

One method of efficiently utilizing the large dataset contained in a Raman line-image is to apply chemometric analysis techniques. Principal components analysis (PCA) has been used with line-imaging Raman spectroscopy to reconstruct images that show regions of independent chemical or physical variation in the sample.[37,67,77] Predictive multivariate calibration methods such as principal component regression (PCR) and partial least squares (PLS) have also demonstrated their usefulness with traditional Raman spectra acquired at a single point. With multivariate calibration methods, the goal is to use a spectrum to predict a specific quantity (*e.g.* concentration) rather than to decompose a spectrum or image into independent components. For example, PLS models have been used with Raman spectra to predict concentration,[78] polymer density and orientation,[79,80] fuel mixture weight percentages,[81] and degree of polymer cure.[82] Multivariate calibrations differ from

traditional, or univariate calibrations, in that an entire spectrum, rather than selected peak or peaks, is correlated with some known quantity. Multivariate calibrations have proven to be relatively less sensitive to spectral noise and other uncorrelated sources of variation than univariate calibrations, and are thus generally more robust predictors. To date however, multivariate calibrations have not been used with line-imaging Raman spectroscopy.

Described in this chapter is the use of line-imaging Raman spectroscopy with both univariate and multivariate calibration models to obtain *in situ* oxidation state profiles of nickel hexacyanoferrate derivatized electrodes held at various potentials in an electrochemical cell. Combining the spatial-spectral images of line-imaging Raman with a multivariate calibration provides a powerful and robust tool for determining profiles in chemical systems. In this chapter, the analysis of Raman line-images to obtain quantitative oxidation state profiles is emphasized, rather than the physical interpretation of the profiles. In Chapter 6, Raman spectroscopy is used to probe the physical and chemical origins of cycle life degradation in nickel hexacyanoferrate electrodes subjected to repeated oxidation and reduction cycles.

5.3 Experimental

Nickel hexacyanoferrate derivatized electrodes were created potentiostatically in the manner of Bocarlsy and coworkers,[7-9] namely, the electrochemical oxidation of nickel metal in the presence of ferricyanide ion. Clean 500 μm diameter 99.98% pure nickel wire (Goodfellow) of area ≈0.09 cm^2 was held at +1.0V vs. SCE for 300 seconds in a bath of 100 mM KNO_3 and 5 mM $K_3Fe(CN)_6$ to form a thin surface film. The derivatized wire electrode was then rinsed with 1M $NaNO_3$ to remove any remaining deposition solution. Cyclic voltammograms were performed in 1M $NaNO_3$ at 50 mV/s scan rate using a PAR 273A potentiostat (Princeton Applied Research). All potentials are referenced to a saturated calomel electrode.

For the work presented in this chapter, one f/10 spherical lens and one f/10 cylindrical lens was used for focusing the laser light to a line, rather than two cylindrical lenses. The spectrograph's 1800 groove/mm holographic grating was used in all studies, and the entrance slit width was set at 500 μm. The combination of lenses, slit width, and detector dimensions gave an imaging line approximately 7 x 10^{-4} cm^2 in area from which Raman scattered light was collected. Thus, Raman spectroscopy sampled about 0.8% of the total electrochemically active area of the derivatized electrode.

Preliminary studies were performed using derivatized microelectrodes to analyze the effects of focussed laser light on the behavior of the hexacyanoferrate layer. Microelectrodes were used so that the focussed laser light impinged on the entire electrochemically active region. Illumination with the 514.5 nm argon ion laser line caused photolytic degradation of the derivatized layer for all intensity levels suitable for Raman spectroscopy. This result is consistent with other Raman studies of ferricyanide salts.[83] On the other hand, a 3040 s exposure of 647.1 nm illumination from a krypton ion laser had only modest effects on the electrochemical behavior of the derivatized layer, even at intensities more than 5 times greater than those used during line-imaging. Six replicate experiments performed with high intensity 647.1 nm illumination show that the derivatized layers retained an average of 90.4% of their original electrochemical redox capacity. The 647.1 nm laser light is outside the main optical absorption band of nickel hexacyanoferrate compounds,[11] so it is less damaging. In addition, the low absorption coefficient at this wavelength allows the laser light to readily penetrate the entire thickness of the *ca.* 80 nm derivatized layer, resulting in Raman signal that originates from the entire depth of the film.

An oxidation state calibration set was constructed from four derivatized electrodes and sixty separate Raman spectra. The sixty calibration-set spectra were acquired in 50 mV increments for potentials that ranged from reduced nickel hexacyanoferrate films

(-100 mV) to oxidized films (+801 mV). The films were held at the desired potential for 60 s to let the current response decay to the background level before taking a Raman spectrum for 100 s. Background current levels were generally reached in less than 10 s.

To acquire Raman images, the electrode was set to the potential of interest and allowed to relax to a background current level. The Raman line-images were exposed for 3600 s. All image processing, PCR and univariate calibration, and statistical analysis was performed using custom software written with LabView (National Instruments) or using Matlab and the PLS_ToolBox (Eigenvector Technologies).

5.4 Results and Discussion

Figure 5.1(a) shows the cyclic voltammogram from a nickel hexacyanoferrate derivatized electrode cycled in $NaNO_3$ solution. The current displayed in the reversible voltammogram peaks arises from the electrochemical switching of the iron-centers in the film according to Eq. (5.1). When the film is potentiostatically held at low potentials, the electroactive iron-centers are in the ferrous state, but as the potential becomes more positive, the iron-centers switch to the ferric state following the sigmoidal curve shown in Figure 5.1(b). The electrochemical cation exchange capacity and charge density of the film, q, are calculated by integrating the reversible charge in the voltammogram. The nominal thickness of the film is 80 nm, as determined from the cation exchange capacity and assuming the entire film volume is electroactive.

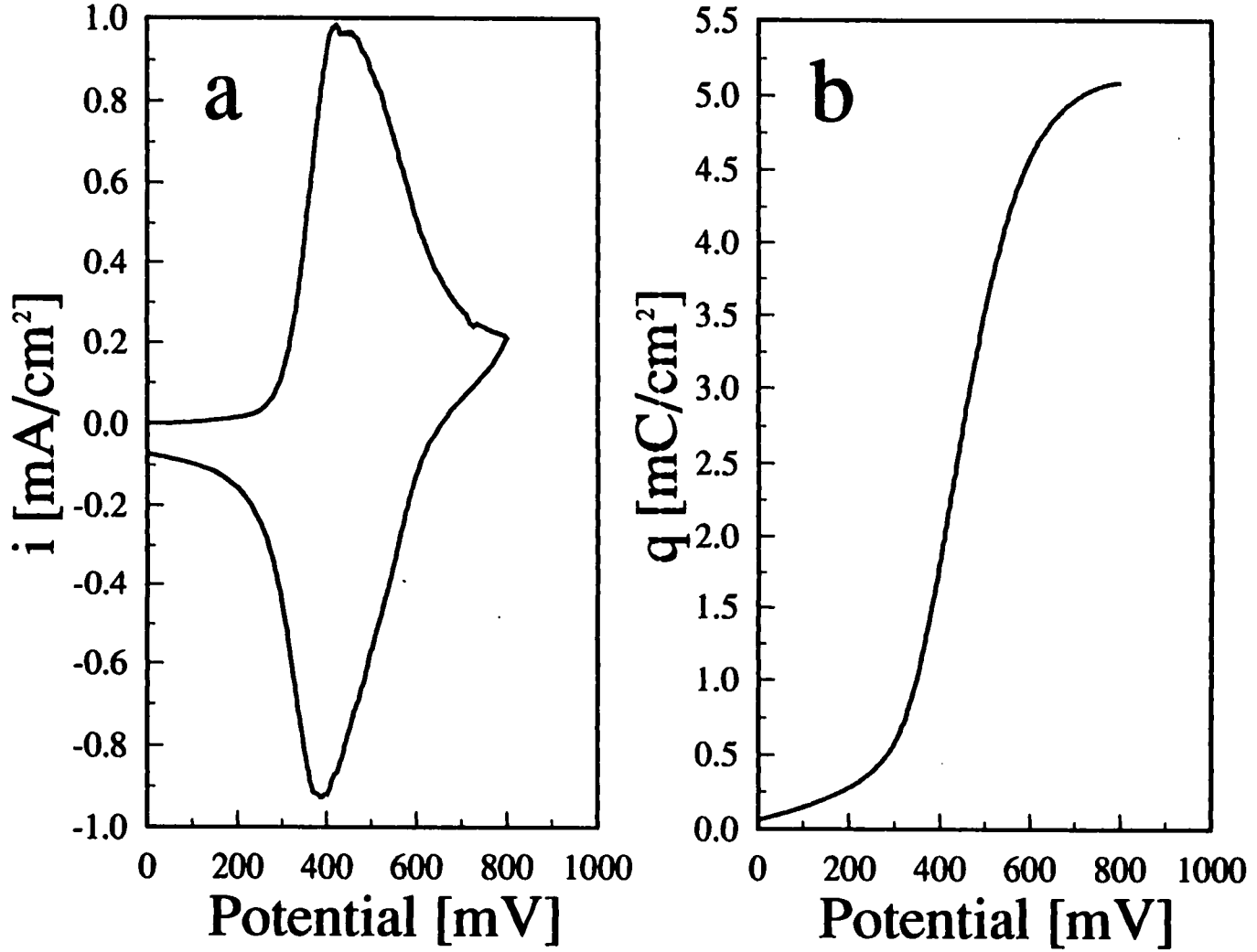

Figure 5.1. a) Cyclic voltammogram of sodium nickel hexacyanoferrate thin film (*ca.* 80 nm) in 1M $NaNO_3$. (scan rate=50 mV/s) b) Integrated voltammogram indicates the cummulative charge density of the film at a given potential.

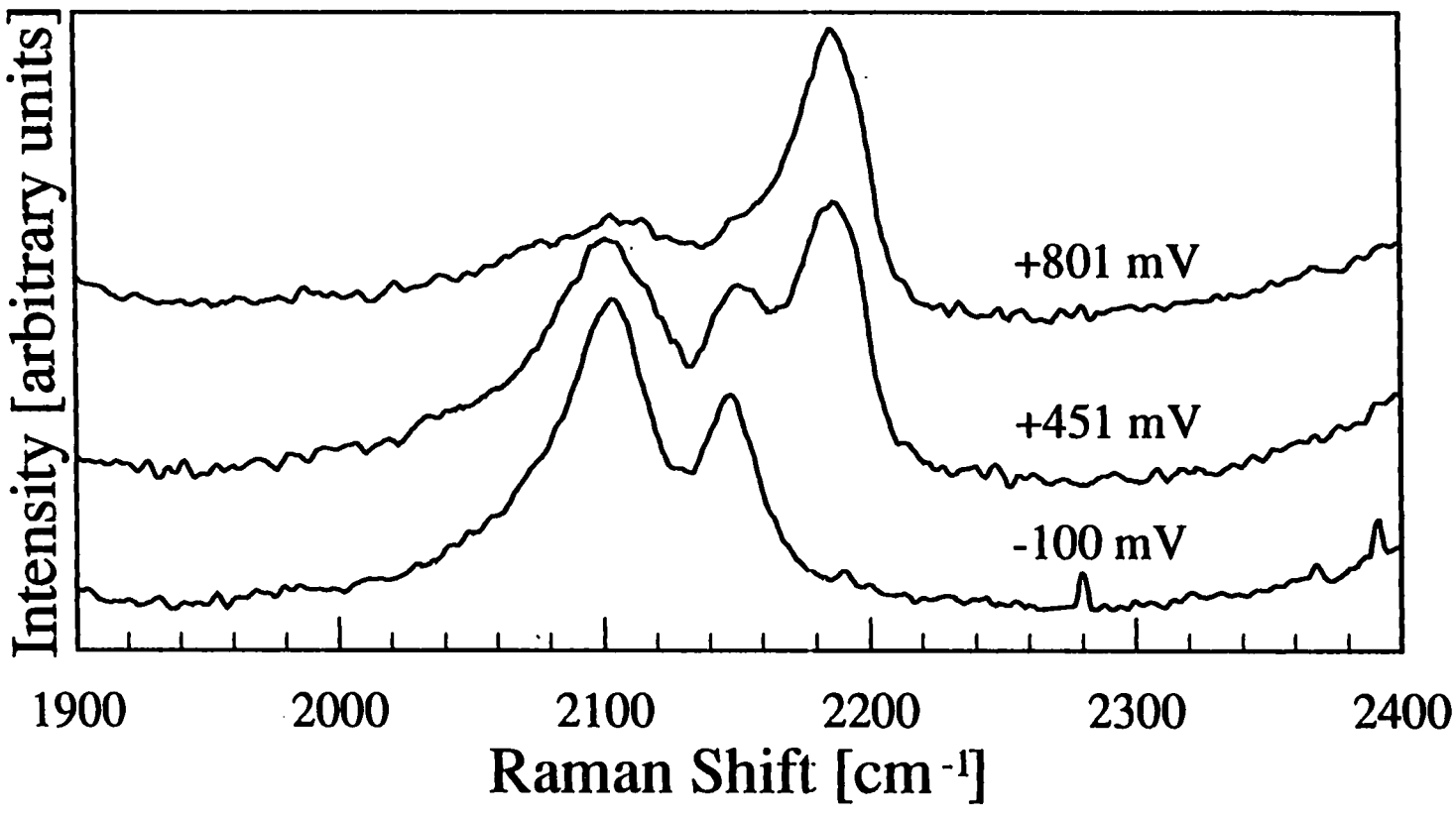

Figure 5.2. Raman spectrum in the CN streching region of sodium nickel hexacyanoferrate thin film as a function of applied potential. Reduced film modes are seen at 2102 cm^{-1} and 2144 cm^{-1}. As the film is oxidized, a mode at 2186 cm^{-1} grows as the other modes diminish. 647.1 nm Kr^{+} excitation wavelength was used.

The Raman spectrum of a derivatized surface is sensitive to the oxidation state of the film, as shown in Figure 5.2. When held at the most reducing potential (–100 mV), the derivatized surface shows two prominent CN stretching modes located at 2102 cm^{-1} and 2144 cm^{-1}. Upon partially oxidizing the surface film at a higher potential (+451 mV), a third CN mode at 2186 cm^{-1} appears, accompanied by a corresponding decrease in intensity of the two lower wavenumber modes. The most highly oxidized film (+801 mV) is characterized by the predominance of the 2186 cm^{-1} CN stretching mode. As noted in the introduction, one expects the CN stretching region from an oxidized film (Fe^{III}) to lie at a higher wavenumber than for a reduced film (Fe^{II}),[75,76] as confirmed by Figure 5.2. Actual and simulated tank wastes from the Hanford Nuclear Reservation that contain colloidal particles of nickel ferrocyanides display comparable Raman spectra to the reduced spectrum for the derivatized surface.[83,84]

From the results in Figure 5.1 and Figure 5.2, it appears that the oxidation state of the film is correlated with spectral features within the CN stretching region of the Raman spectrum. To create a multivariate correlation relating spectral features to the oxidation state of the film, x, one must build a calibration set by collecting spectra from derivatized layers of known oxidation state. Through Raman studies of many different electrodes, we have observed that some nickel hexacyanoferrate derivatized layers, when held at +801 mV, display spectra that look more like the +451 mV spectra in Figure 5.2 (*i.e.*, the 2186 cm^{-1} mode does not dominate the spectrum). This observation suggests that in some cases the entire film is not fully electroactive: all of the iron-centers may not switch from the ferrous to the ferric state when the film is set to an oxidizing potential. If the entire film were fully electroactive, then the charge density of the film (q, as in Figure 5.1b) would be directly related to the fraction of the film oxidized according to the relationship $x=q/q_{max}$, where q_{max} is the maximum electroactive capacity of the film. However, if the entire film is not

electroactive, then there is no straightforward *a priori* method for knowing x from electrochemical measurements alone.

Principal component analysis (PCA) performed on a series of Raman spectra from several derivatized electrodes held at different potentials can help to define the true, absolute value of x. Figure 5.3 shows a comparison between the cumulative charge density and the scores on the second principal component† (PC2) of Raman spectra taken at different potentials. The scores on PC2 from this analysis correlate well with the cumulative charge determined from an integrated cyclic voltammogram. The transition in the cumulative charge curve is not quite as sharp as the PC2 curve derived from Raman spectra. The difference is likely due to the fact that the Raman-based curve originates from steady state Raman spectra, whereas the cumulative charge curve is from the dynamic measurement of a system with a finite response time. When Raman spectra from several films are included in the principal component analysis, the scores on PC2 reveal that the extremes of oxidation or reduction for each film are somewhat different from each other. Thus, PC2 quantitatively shows the same trait we observed qualitatively; some electrodes possess inactive materials that do not switch oxidation states. Using this approach with the Raman calibration set (taken from four independently derivatized electrodes), we defined the most oxidized film in this set (largest PC2 score) as fully oxidized, or x=1, and defined the most reduced film (smallest PC2 score) as fully reduced, or x=0. This places the degree of oxidation values from different films on the same absolute scale.

† The second principal component for data not mean-centered describes the greatest source of independent variation in the spectra. In this case, this variation can be attributed to changes in the Raman spectra as the film oxidation state changes.

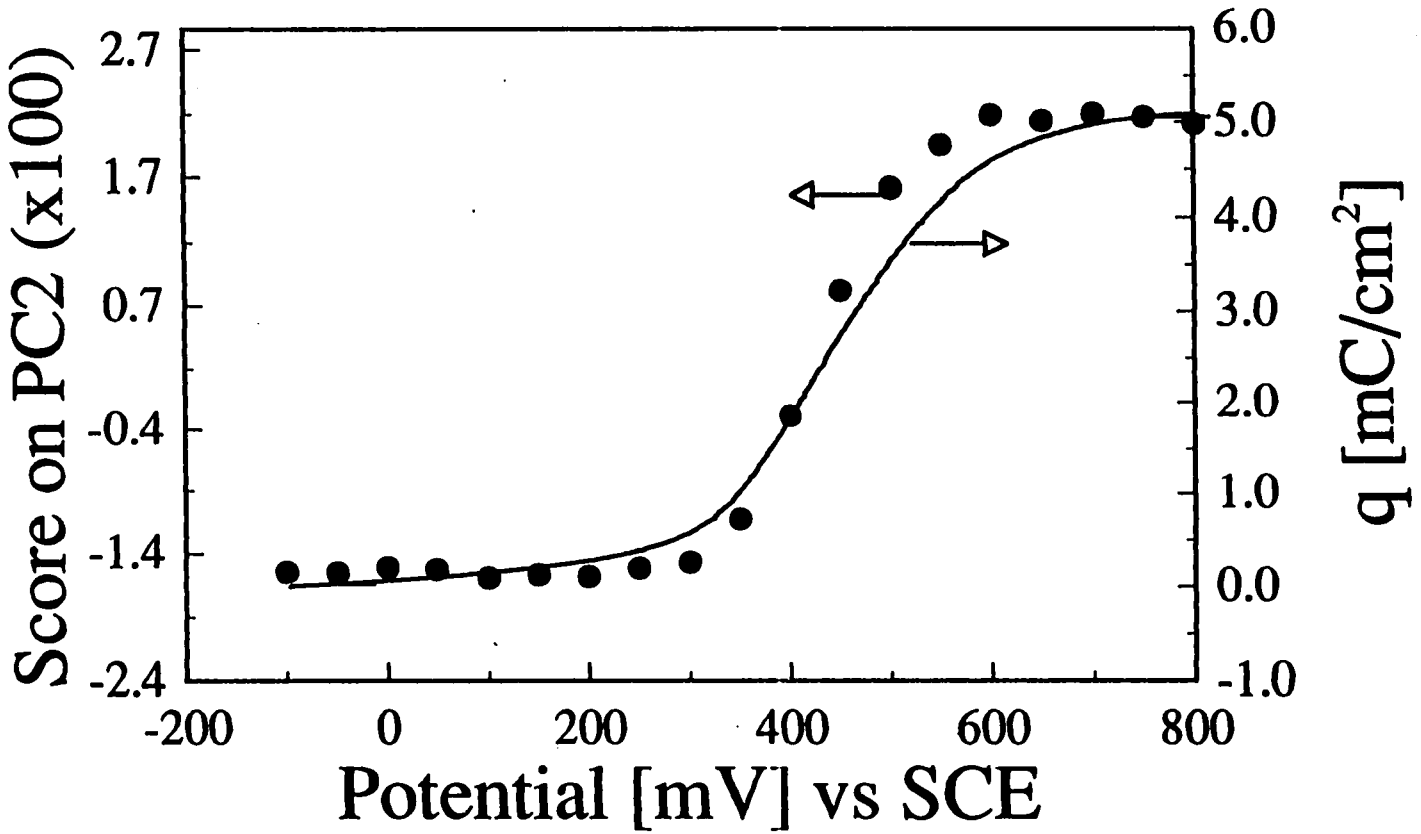

Figure 5.3. Comparision between the cummulative charge in the film determined electrochemically (–) and the score on PC2 taken from a series of Raman spectra (●).

After placing the calibration set on an absolute oxidation state scale, a multivariate principal component regression (PCR) model using one principal component was developed,[85,86] as was a univariate model that uses the ratio of the height of the 2186 cm^{-1} peak to 2102 cm^{-1} peak to linearly predict film oxidation state. Figure 5.4 shows the performance of each model for the sixty member calibration set. The PCR predictions are seen to fit well. The univariate predictions also fit reasonably well, although with much more scatter. Having created two correlations, it is now possible to apply either correlation to independent Raman spectra and determine the oxidation state of the derivatized film.

Three Raman line images were taken of a nickel hexacyanoferrate derivatized electrode under potential control in a reduced (-100 mV), intermediate (+451 mV), and oxidized (+801 mV) state. Figures 5.5(a–c) show images with their backgrounds subtracted using Adapted Pearson's Method.[87] The vertical dimension is distance along the film, and the horizontal dimension is Raman shift. The dark vertical bands in each image are Raman signal from the CN stretching modes of the film (signal intensity is denoted by the gray scale, with black being the most intense and white the least intense). In the reduced film image (Figure 5.5a), the spatial distribution of the two Raman modes at 2102 cm^{-1} and 2144 cm^{-1} is seen. As the film is oxidized at +451 mV to an intermediate value of x (Figure 5.5b), the 2186 cm^{-1} mode begins to appear. As the film is further oxidized at +801 mV (Figure 5.5c), the higher wavenumber mode is seen to dominate. In the center of each image lying between spatial locations 500 and 750 μm, there are two horizontal streaks, and there is also a rather abrupt change in signal at locations >1100 μm. We often observe anomalous streaks of this nature when imaging surface films; they are apparently due to strong Rayleigh scattering in the vicinity of local morphological defects in the sample.

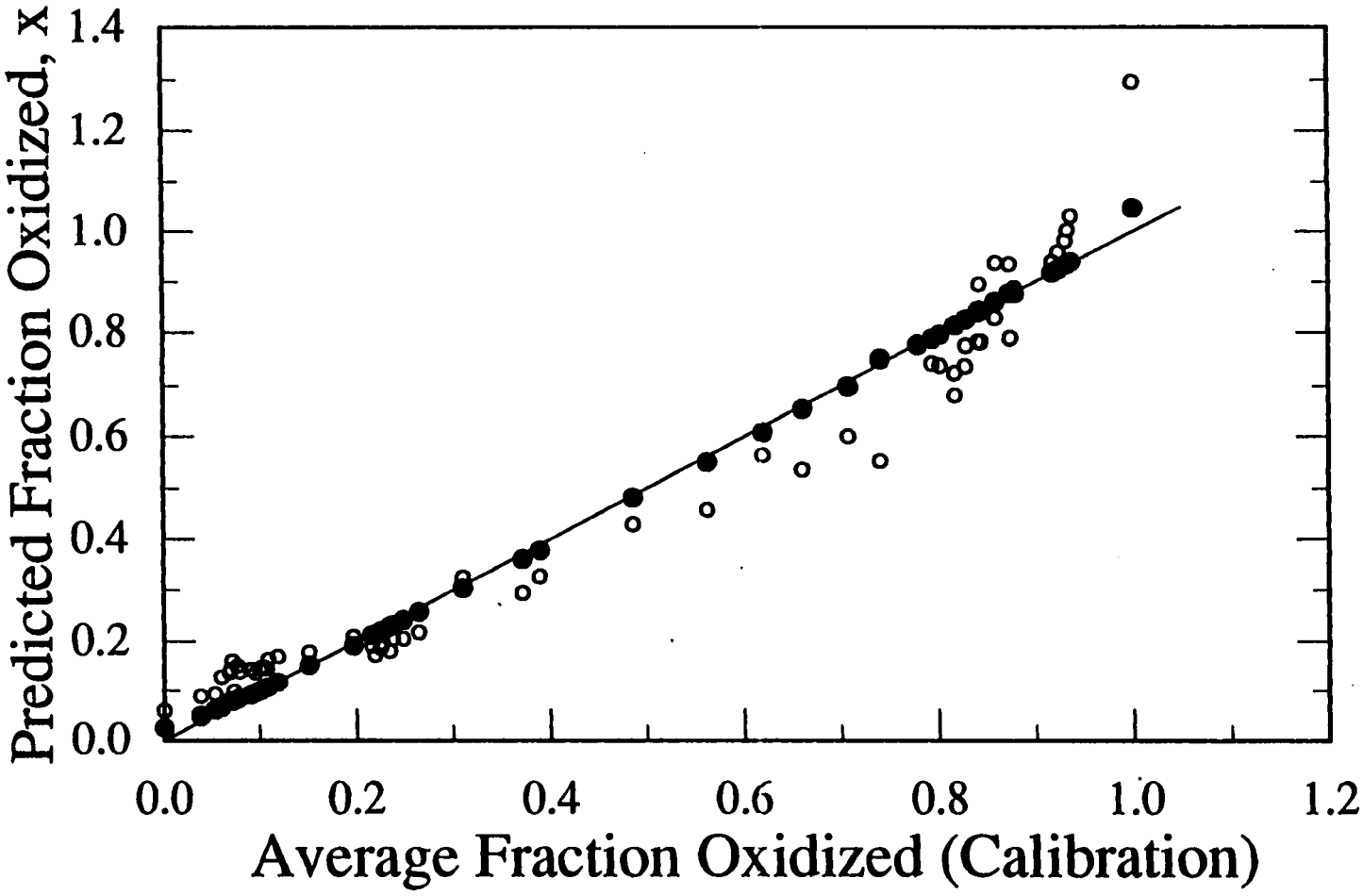

Figure 5.4. Comparison of model fits to the calibration set. The multivariate PCR model(●) uses the entire spectrum to predict the fraction of film oxidation. The univariate model(O) uses the ratio of the height of the 2186 cm^{-1} Raman mode to the 2102 cm^{-1} Raman mode to linearly predict the fraction of film oxidation.

5.4.1 Image preprocessing

It is clear in Figure 5.5(a-c) that the signal intensity is greatest near the middle of the spatial axis, and weakest at the top and bottom. This is due to the Gaussian intensity profile of the focused laser line used to excite the measured Raman signal. Before any of the images in Figure 5.5(a-c) can be used with the PCR correlation to predict an oxidation state profile, the signal intensity must be normalized from the top of the image to the bottom. Using the region containing Raman signal, 2050-2210 cm^{-1}, the images were intensity normalized using the ratio of the vector magnitude of the average spectrum from the PCR calibration set to the vector magnitude of each spectrum that makes up the background subtracted image. The vector magnitude of a spectrum is the square root of the sum-of-squared intensities at each pixel in the spectrum. This intensity normalization factor scales each spectral row in the image so that it most closely matches the intensity of the average spectrum from the PCR calibration set. This intensity normalization procedure is similar to Multiplicative Scatter Correction, which has been used successfully before as a preprocessing step in multivariate correlations.[78,88] Normalizing each spectrum of an image in this manner eliminates the Gaussian laser profile, however the inherent signal-to-noise ratio (S/N) in the image remains unchanged. Figures 5.5(d–f) show the intensity normalized raw images presented in Figure 5.5(a–c), respectively. Notice that the Raman bands now span the entire image spatially, but near the top and bottom of the images, the amount of noise present increases.

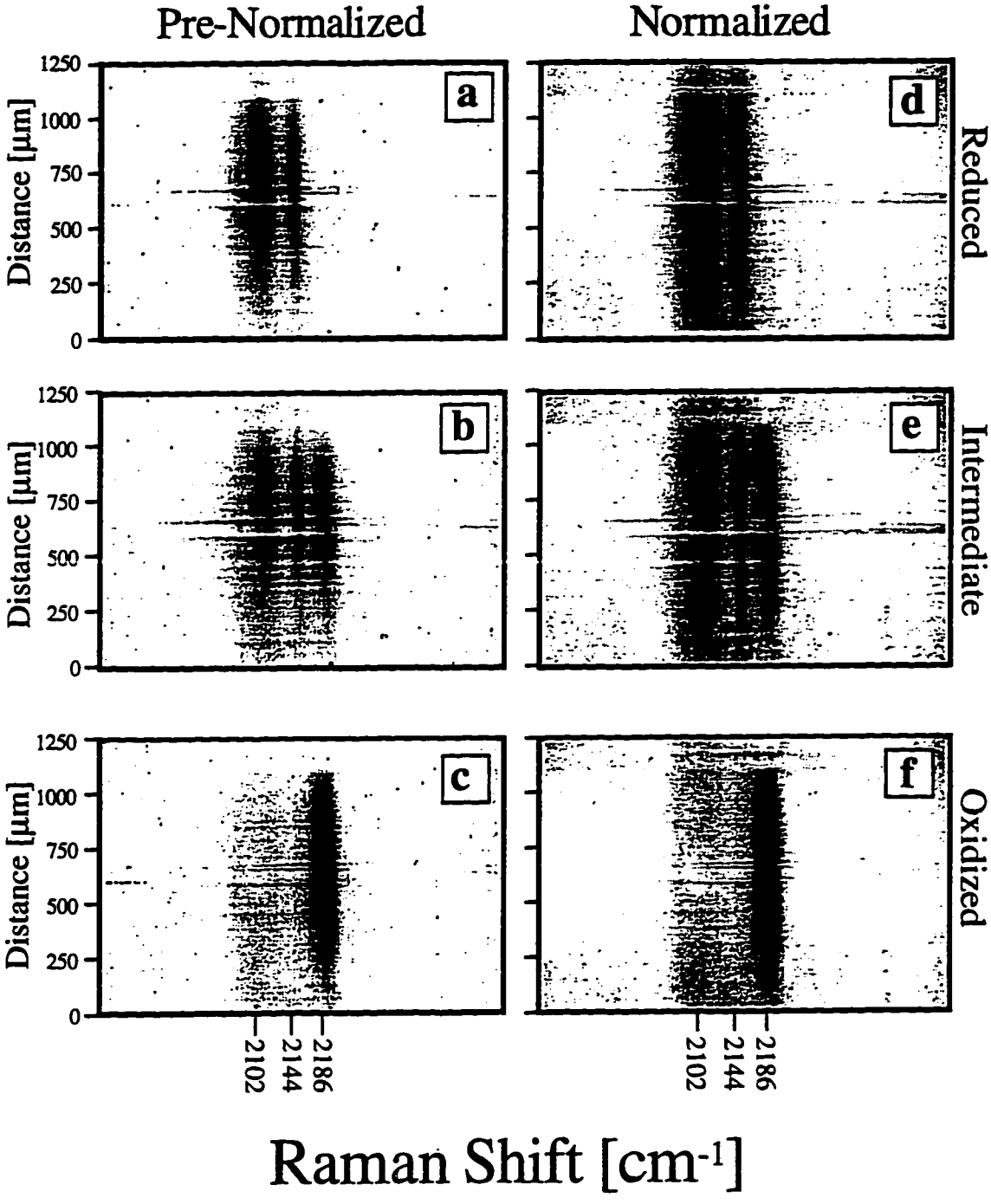

Figure 5.5. Raman line-images of sodium nickel hexacyanoferrate thin film in a reduced (-100 mV, top), intermediate (+451 mV, middle), and oxidized (+801 mV, bottom) state before and after intensity normalization. Spatial resolution is ~5 μm.

Figure 5.6 shows the spatial profile of the intensity normalization factor used to preprocess the images. This factor represents the intensity profile of the collected light from the sample. Since signal strength is predominately determined by the intensity of the excitation beam, this profile has the Gaussian shape of the focused laser line. Other factors affecting the strength of the collected light such as anomalous scattering at the streaks between 500 and 750 μm, and the region >1100 μm are also seen in Figure 5.6 as distortions to the overall Gaussian shape.

Figure 5.7(a) shows representative spectra taken from the centers of Figure 5.5(d–f), at about the 735 μm position. Similarly, Figure 5.7(b) shows spectra taken from near the edges, at about the 60 μm position. The three Raman peaks characteristic of nickel hexacyanoferrate can be identified at 2102, 2144, and 2186 cm^{-1} in both Figure 5.7(a) and 7(b). The spectra from the center of the image resemble those from the edge, but they have better S/N and also appear to be more oxidized than the edge locations. Specifically, one can clearly see that the +801 mV spectrum in Figure 5.7(a) is characteristic of a more oxidized material than the corresponding spectrum in Figure 5.7(b) (noted by the 2186 cm^{-1} Raman peak relative to the two lower wavenumber modes in each figure). By looking at two spectra taken from different locations, we can qualitatively surmise that the these positions have different oxidation states; the purpose of developing univariate or multivariate correlations is to quickly and quantitatively carry out this same oxidation state evaluation hundreds of times in each Raman image. Signal quality ultimately limits the predictive ability of any model, and before either the PCR or univariate model was used, each image was filtered with a 2nd rank median filter to remove intensity spikes from cosmic rays. For PCR predictions, no further filtering was performed. Before the univariate model was used, a 5-point moving average window was applied to each spectral row of the image.

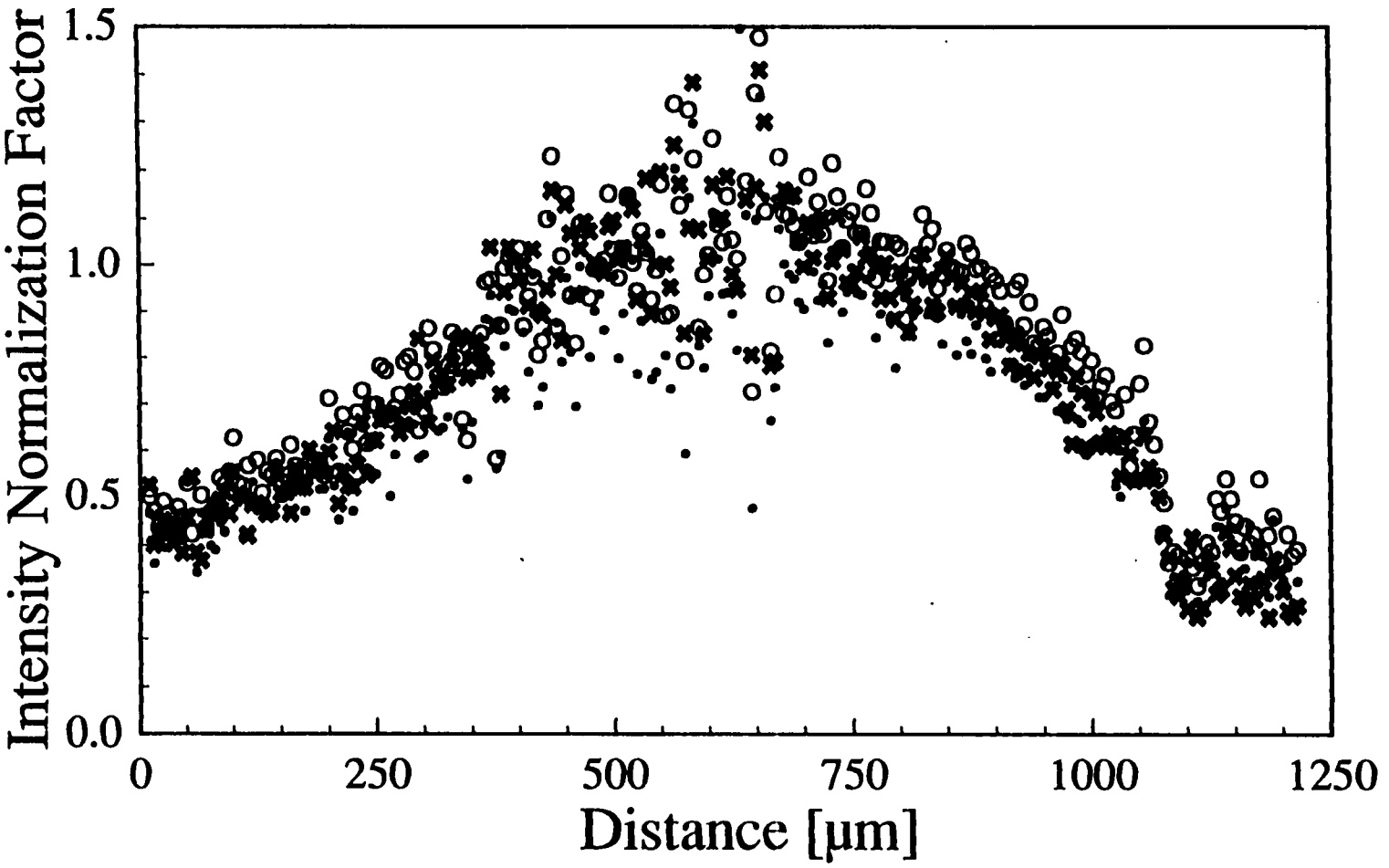

Figure 5.6. Profile of the intensity-normalizing multiplicative factor for the reduced(O), intermediate(●), and oxidized(✖) images shown in Fig. 5.5

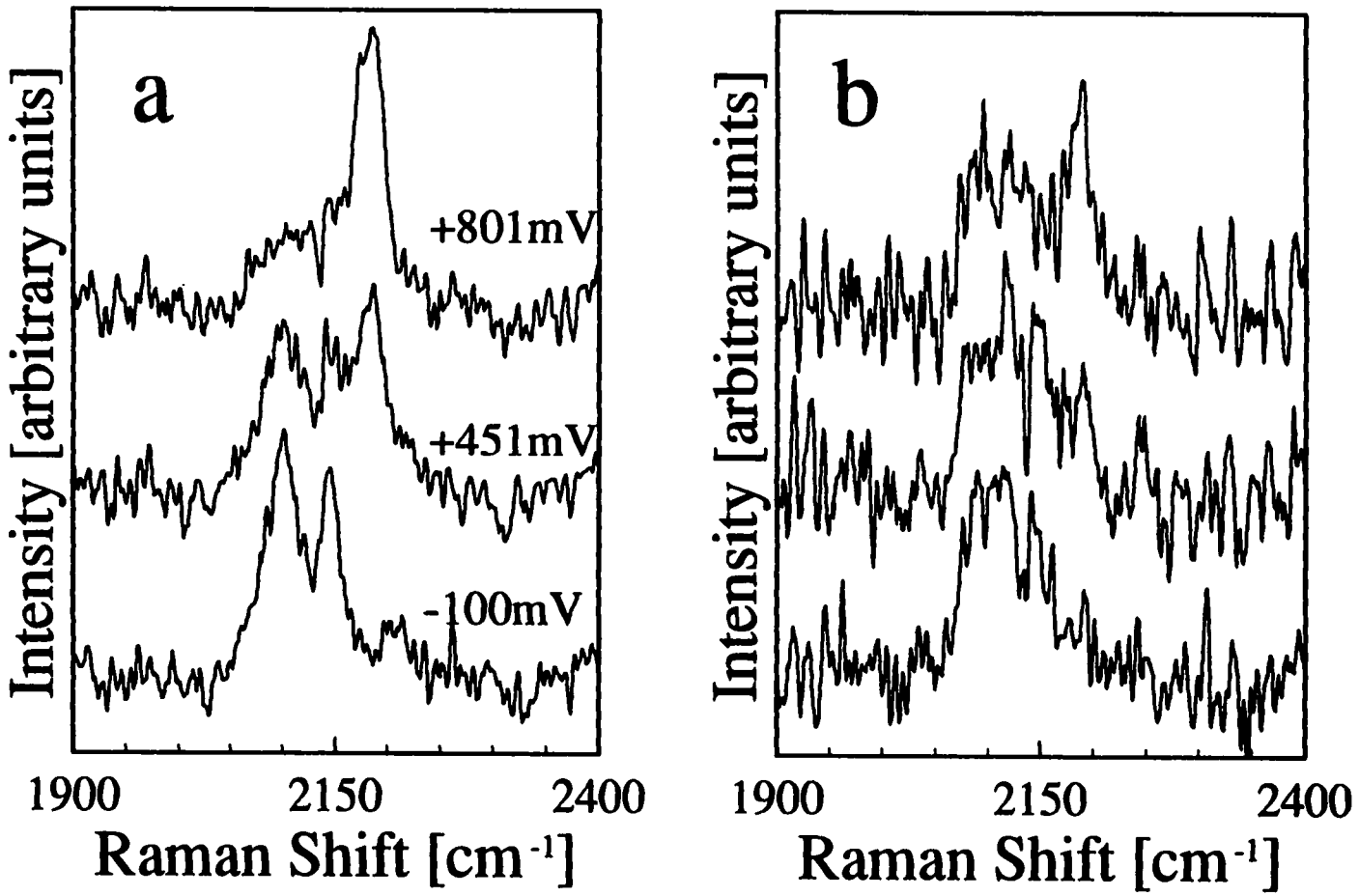

Figure 5.7. Representative spectral slices of the film in reduced (-100 mV), intermediate (+451 mV), and oxidized (+801 mV) states taken from the Raman line-images shown in Fig. 5.5. a) Spectra taken from the centers of the images (735 μm). b) Spectra taken from the bottom edges of the images (60 μm).

5.4.2 Oxidation state profiles

Figure 5.8 shows the oxidation state spatial profiles along the derivatized electrode surface as determined by the PCR and univariate models. An oxidation state profile is shown for each intensity normalized image in Figure 5.5. For each profile shown in Figure 5.8, the univariate correlation is seen to have more scatter than the PCR model. Moreover, the univariate correlation predicts that the fractional oxidation of the film (x) can extend significantly beyond the physical [0,1] range. The PCR model slightly exceeds physical bounds at a few locations in the oxidized profile, but for the most part x lies within the [0,1] range. The PCR model is clearly less sensitive to spectral noise than the univariate model is, demonstrating one advantage of a multivariate approach. Further discussion is limited to the oxidation state profiles derived from the PCR correlation.

Certain traits displayed by the images in Figure 5.5 are clearly reflected in the oxidation state profiles in Figure 5.8(a). For example, the spectral streaks running horizontally through the center of each image in Figure 5.5 show up as spurious points in the middle of the oxidation state profiles (between 500 and 750 μm). Another obvious feature in the normalized images, Figure 5.5(d-f), is the rather abrupt change in S/N near the top of the images (>1100 μm). In this region of Figure 5.8(a), the predicted oxidation state of all three profiles also changes rather abruptly. On the other hand, subtleties not seen in the images of Figure 5.5 can be observed in the oxidation state profiles. For the most highly oxidized state presented in Figure 5.8(a), the PCR correlation predicts a value of x near unity in the center locations, but the predictions gradually decrease to approximately x=0.65 at the 0 μm position. This is exactly the same trend that was observed qualitatively when comparing Figure 5.7(a) and 7(b), namely, that the edge region (near 60 μm) is less oxidized than the center (near 735 μm). PCR allows the quantification of this trend and also shows that the spectra presented in Figure 5.7 are not

unusual in any way, but are part of a general trend towards a less oxidized material at the edges of the image. Similarly, the profile for the reduced film is near x=0.0 for locations right of center, but rises to approximately x=0.2 at the left edge. The intermediate oxidation state profile has a degree of oxidation of x=0.4 at the edges (0 and 1100 μm), and arcs through the center with a maximum of approximately x=0.6.

Two statistical methods are commonly used to assess the confidence that can be placed in multivariate predictions. The first method involves the calculation of the residual Q value for each spectrum used to make a prediction with the PCR model. The residual Q value is the sum of the squares of the residuals, where the residuals are the portion of the original spectrum not described by the multivariate space.[89] Physically, the residual Q describes how closely the spectrum being analyzed resembles the calibration spectra that were used to build the PCR model (*i.e.* how closely do spectra in Figure 5.7 resemble spectra in Figure 5.2). The smaller Q is, the more assured one can be that the spectrum being analyzed is consistent with the PCR correlation. Conversely, a large Q value indicates the spectrum being analyzed somehow deviates from the spectra used to create the model, indicating that the model may not be applicable to this spectrum.

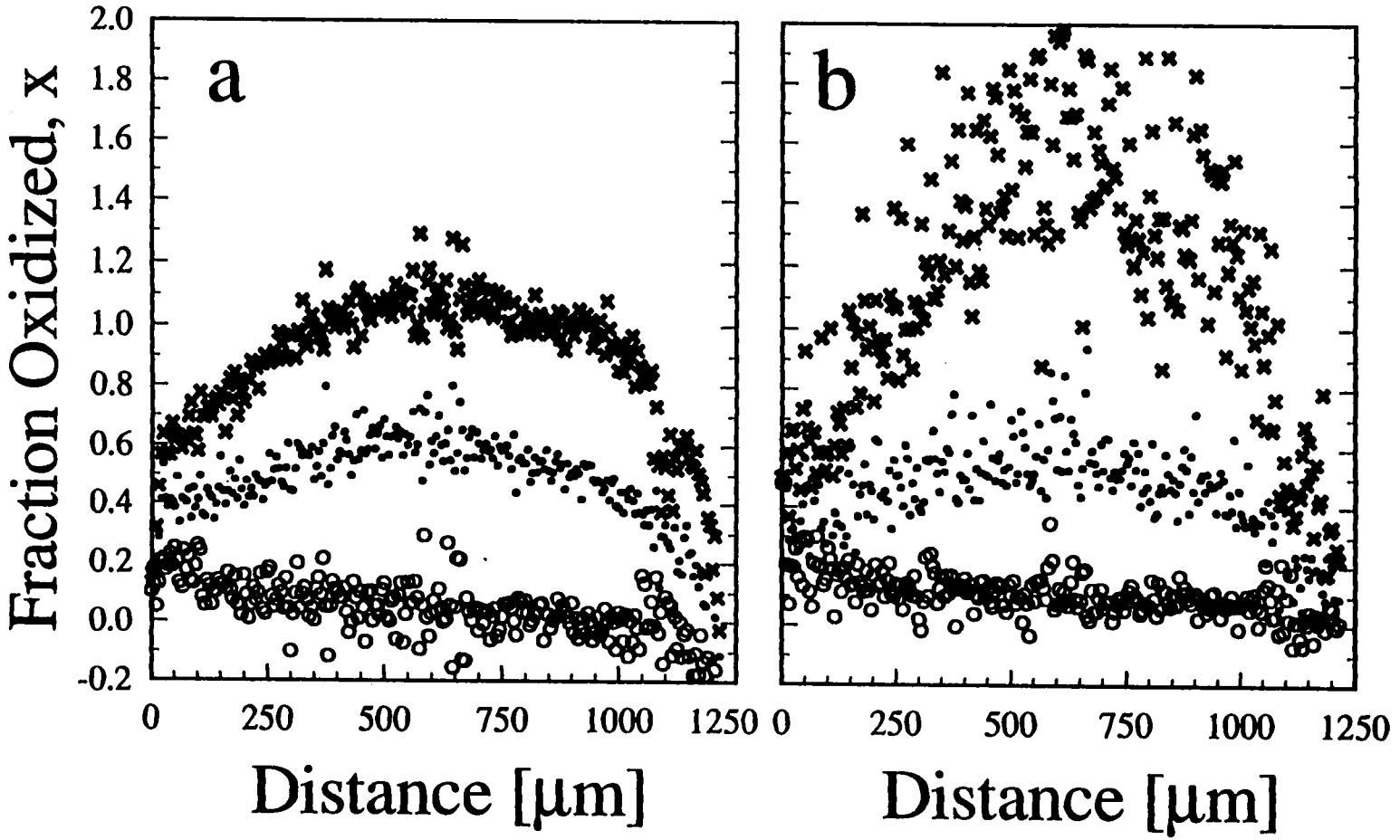

Figure 5.8. Oxidation state spatial profiles in an electroactive sodium nickel hexacyanoferrate thin film held at -100 mV(O), +451 mV(●), and +801 mV(✖). The multivariate PCR model (left) provides much smoother profiles than the univariate model (right). Spatial resolution is ~5 μm..

Figure 5.9 shows the residual Q values for each of the oxidation state profiles given in Figure 5.8(a). The residual Q shows two spatial regions of anomalously high values deviating from the general trend: spurious points between 500 and 750 μm, and points at locations >1100 μm. The horizontal streaks seen in Figure 5.5 fall at the locations of high values of Q (between 500 and 750 μm) in Figure 5.9 for all three potentials. From these high residual Q values, we see that the underlying spectra that make up the streaked region are not especially similar to that of nickel hexacyanoferrate, possibly because they are distorted by a highly scattering surface asperity. The residual Q values also jump to high values at locations >1100 μm, where there is an abrupt change in signal quality observed in the underlying data (*e.g.* see top of images in Figure 5.5). Aside from the regions just discussed, the Q values show the general trend of decreasing signal to noise ratio from the center out to the image edges (Q rises for spectra with lower S/N). Using the residual Q statistics, we have identified the anomalous regions of the image where the spectra do not sufficiently resemble the calibration spectra used to build the PCR correlation to make trustworthy predictions of oxidation state. Moreover, we have seen that the oxidation state profiles tend to display aberrant behavior in regions of anomalously high residual Q. In short, the residual Q statistic identifies all the aberrant "trouble areas" of the Raman image, and does so quantitatively.

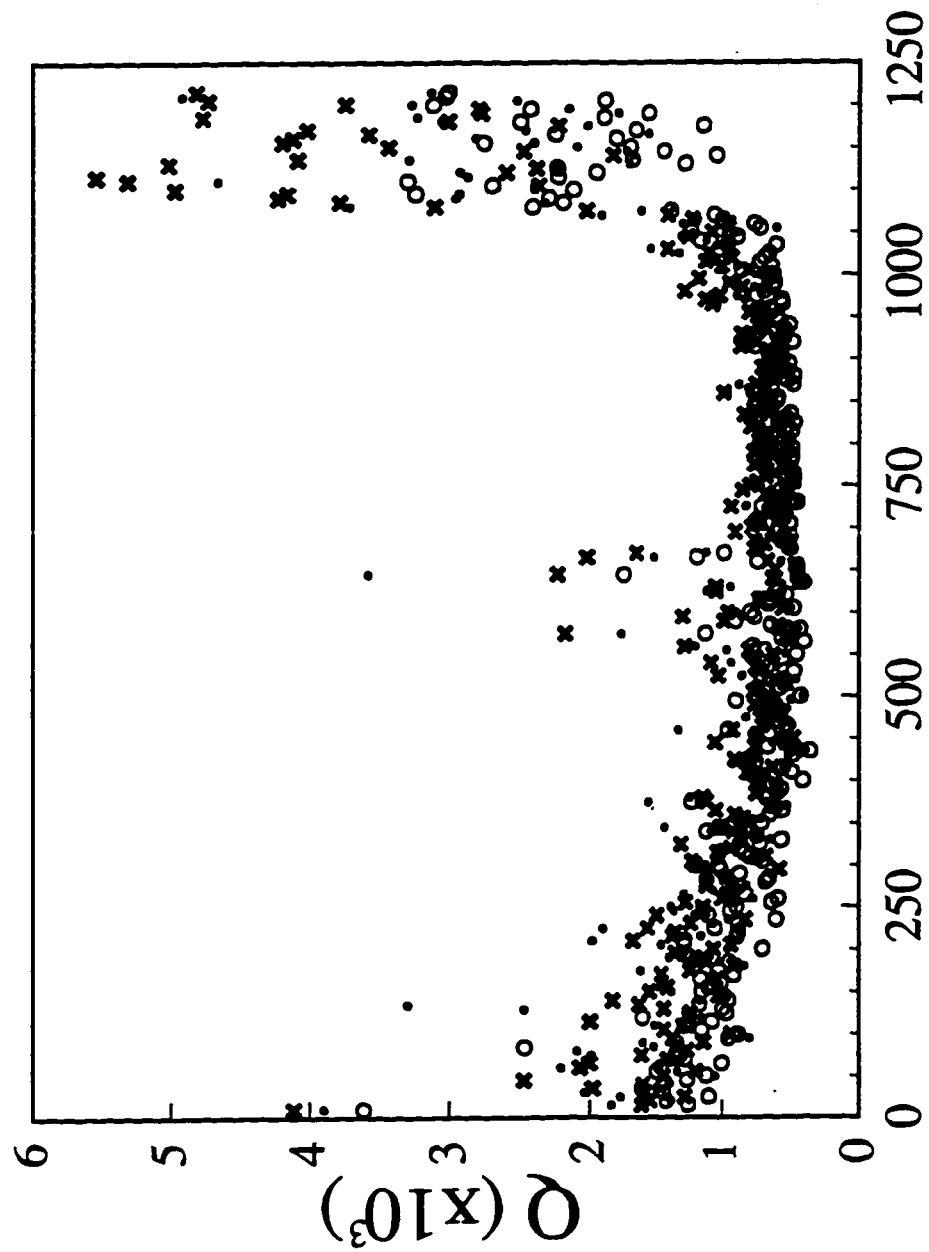

Figure 5.9. Values of the residual Q statistic for the reduced(O), intermediate(●), and oxidized(✖) profiles shown in Fig. 5.7.

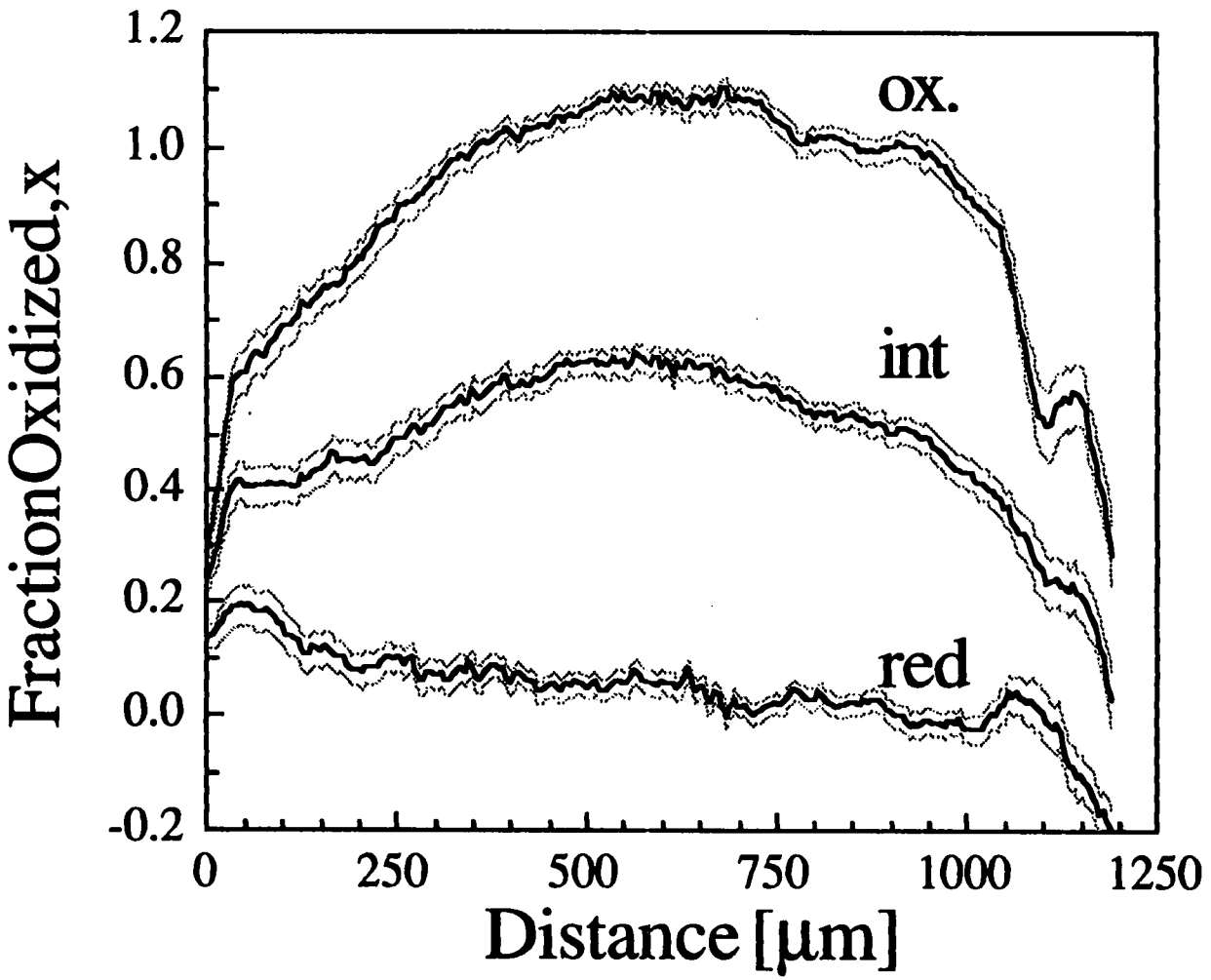

Figure 5.10. Oxidation state spatial profiles of the film in reduced, intermediate, and oxidized states showing 95% confidence limits (gray lines) based on random spectral noise.

The second method used to quantify our certainty in the profiles is to linearly propagate spectral variance through the PCR correlation. The random variance in each spectrum was estimated using 75 pixels taken from a low wavenumber region free of Raman signal. Figure 5.10 shows the oxidation state profiles with associated 95% confidence limits (N=717). These limits describe variation in the prediction due to random (Gaussian) noise in a given spectrum. The profiles in Figure 5.10 have been smoothed with a 10-point moving average filter to enhance readability. This figure shows that random spectral noise contributes less than x±0.1 uncertainty in the oxidation state profiles.

5.5 Conclusions

We have demonstrated the application of line-imaging Raman spectroscopy and multivariate calibration for determining the oxidation state in a thin film of sodium nickel hexacyanoferrate. This technique is nondestructive, and can be used *in situ* in aqueous media. The multivariate calibration is compared to a univariate calibration based on the ratio of Raman peak heights. It is shown that the PCR model is a superior predictive tool due to its relative insensitivity to spectral noise.

Oxidation state profiles are generated from a PCR model and Raman line-images of a derivatized electrode potentiostatically held in a reduced, intermediate, and oxidized state. Two statistical measures of model certainty indicate that the PCR correlation is appropriately modeling the film's oxidation state, and that noise in the spectra are not corrupting the results. It is seen by referring to the spectra in Figure 5.7 and the model predictions in Figure 5.8 and Figure 5.10 that the center of the region being analyzed is more readily oxidized to ferric iron than the edges of the region being analyzed. Comparing the intensity profile of the laser (Figure 5.6) to the oxidation state profiles (Figure 5.8), suggests there may be a connection between them. In Chapter 6, we present

the interpretation of these oxidation state profiles and many more taken from derivatized electrodes cycled until their capacity is degraded.

CHAPTER 6: USING LINE-IMAGING RAMAN SPECTROSCOPY TO STUDY CYCLE LIFE DEGRADATION IN NICKEL HEXACYANOFERRATE DERIVATIZED ELECTRODES

6.1 Chapter Overview

Raman spectroscopy is used to study cycle life degradation in nickel hexacyanoferrate (NiHCF) derivatized electrodes. Derivatized electrodes cycled in 1M $NaNO_3$ are shown to sustain between two and eight thousand oxidation and reduction cycles prior to losing most of their electrochemical ion exchange capacity. The main cause of cycle life degradation is a decline in the ability of the iron-centers in the NiHCF to switch oxidation states, rather than a physical loss of the derivatized layer from the surface. The degradation of the derivatized layer occurs nonuniformly, with some regions of the electrode declining faster than the average electrode, and some regions maintaining redox activity even when most of the electrochemical capacity has been lost. In all cases studied, the derivatized electrodes reach a terminal degraded state where the NiHCF layer has a spatially uniform ratio of ferrous to ferric irons of 4:1. This terminal degraded state does not respond to modulating the potential of the electrode. Electrodes held at constant oxidizing and reducing potentials for an hour or more are found to lose electrochemical ion exchange capacity at a higher rate than when the electrodes are cycled continuously. Preliminary results indicate that the NiHCF matrix is photoconductive and absorbs the 647.1 nm laser light *via* a metal-to-metal charge transfer process.

6.2 Introduction

Metal hexacyanoferrate compounds such as Prussian Blue (iron hexacyanoferrate) and its nickel and cobalt analogs have electrochemically reversible iron-centers that can be switch between the ferrous and ferric oxidation states *via* an applied potential. The electrochemical reduction of iron in the lattice requires the intercalation of a cation into the material to maintain charge neutrality, whereas oxidation of an iron-center requires the ejection of a cation from the lattice. For the specific case of nickel hexacyanoferrate (NiHCF), electrochemical modulation proceeds according to the reaction

$$A_{2-x}Ni^{II}Fe^{II+x}(CN)_6 + xA^+ + xe^- \rightleftharpoons A_2Ni^{II}Fe^{II}(CN)_6 \qquad (6.1)$$

where A denotes a cation and x is the fractional oxidation state of the NiHCF ($0 \leq x \leq 1$).

There are a number of possible technological applications for electrochemically switched metal hexacyanoferrate compounds. Prussian Blue (iron hexacyanoferrate), the most widely studied metal hexacyanoferrate compound,[3,73,90] is electrochromic and has been demonstrated as suitable for display devices.[3] Recently, cobalt hexacyanoferrate has been shown to be a molecular magnet with properties that can be modulated by illumination with red and blue light,[4,5] suggesting possible applications in magneto-optical data storage devices. NiHCF compounds have an affinity for the intercalation of Cs^+ over all other group 1A cations, suggesting possible applications as ion exchange material.[6] This trait may prove to be important for removing radioactive $^{137}Cs^+$ from sodium-containing tank and basin wastes at sites such as the Department of Energy's Hanford Nuclear Reservation in Richland, Washington.

To a great degree, the application of any electrochemically modulated metal hexacyanoferrate rests on the stability of these materials over many potential cycles. Previous work has explored several factors affecting the cycle life degradation and response of Prussian Blue films for use as display devices, including pH and film

deposition protocol.[13,14] It was found that Prussian Blue is much more stable in acidic environments than in neutral baths over many potential cycles. However, electrochromic Prussian Blue films are susceptible to nonuniform response, as indicated by regions that do not change color as the potential is modulated (*i.e.* some regions are not redox active). It has been suggested that regions of the film that lack electrochromic response may have become electronically disconnected or perhaps physically detached from the electrode substrate.[14] The addition of a small amount of ferricyanide ion to the electrolyte has been observed to enhance the cycle life of Prussian Blue.[13] Similarly, the cycle life of NiHCF is greatly enhanced with the addition of ferricyanide ion to the electrolyte.[7] Aside from the addition of ferricyanide, little has been done to understand the mechanisms for cycle life degradation of NiHCF (or other Prussian Blue analogs).

Although the cation exchange properties and general stability of NiHCF have been demonstrated,[8,9] more work is needed to characterize cycle life degradation. The ion exchange capacity of a NiHCF derivatized electrode may decrease due to physical loss (*i.e.* sloughing or dissolution of the film), or it may decrease due to chemical or structural transformations that hinder ion or electron transport through the lattice. Since the ability of iron-centers in NiHCF to be modulated is intimately coupled to ion exchange properties, probing the film's oxidation state may lead to a greater understanding of the cycle life characteristics of NiHCF. As shown in the previous chapter and elsewhere,[47,91] line-imaging Raman spectroscopy has emerged as a valuable *in situ* tool for use in electrochemical systems due to its ability to collect molecularly specific information over macroscopic length scales. In Chapter 5, *in situ* line-imaging Raman spectroscopy was combined with a multivariate PCR model to profile the oxidation state of a nickel electrode that was derivatized with a thin film (*ca.* 80 nm) of NiHCF. The focus of this chapter is

to apply the methods developed in Chapter 5 to better understand the preparation and cycle life behavior of NiHCF derivatized electrodes.

6.3 Experimental

The line-imaging Raman spectroelectrochemical system, and electrode derivatization procedure have been described in previous chapters. The derivatized electrodes have a geometrical area of ≈0.09 cm^2. Raman spectra are acquired from an area of approximately 7 x 10^{-4} cm^2 on the derivatized electrode surface (about 1% of the total electrode area). NiHCF derivatized electrodes were cycled between -100 mV and +800 mV at a potential sweep rate of 50 mV/s for up to 8000 cycles in 1M $NaNO_3$. A cyclic voltammogram (CV) was saved every fifth sweep. The reversible ion exchange capacity of the film was calculated by taking one half of the total charge between the anodic- and cathodic-sweeps of the CV. At intervals of approximately 2000 cycles, the potential cycling was suspended while Raman images were acquired at a reducing (-100 mV), an intermediate (+451 mV), and an oxidizing (+800 mV) potential. All potentials are referenced to a saturated calomel electrode (SCE). The 647.1 nm emission from a krypton ion laser was used to excite the samples, and the spectrograph entrance slitwidth was set to 500 μm in all cases reported. The laser power was nominally 100 mW, and the Raman image exposure time varied from one to four hours. After acquiring Raman images, potential cycling resumed. In all cases, background signal was removed by the Adapted Pearson's Method.[87]

6.4 Results and Discussion

6.4.1 Spectral and electrochemical responses

Figure 6.1 shows the electrochemical response from three freshly prepared NiHCF derivatized electrodes (labeled A, B, and C). All three electrodes were made under

nominally identical conditions. From the voltammograms, one can calculate that electrodes A, B, and C have initial electrochemical ion exchange capacities of 3.69, 2.44, and 3.12 mC/cm^2, respectively. These capacities correspond to films of thickness 58, 38, and 49 nm, assuming the entire film is electroactive. Even though the electrodes were derivatized under the same nominal conditions, the results in Figure 6.1 show that the derivatization procedure can introduce some variability from electrode to electrode.

Figure 6.2 shows the Raman spectra from the freshly prepared electrodes in reduced ($E \leq -100$ mV) and oxidized states ($E \geq +779$ mV). The Raman signal from cyanide (CN) stretching modes in NiHCF is sensitive to applied potential, as shown in Figure 6.2 and Chapter 5. The reduced state of the film (-100 mV) produces two prominent Raman peaks near 2102 cm^{-1} and 2144 cm^{-1}. At intermediate levels of oxidation (+450 mV), a third Raman peak appears near 2186 cm^{-1} while the two lower wavenumber peaks decline in intensity. At highly oxidizing potentials (≥779 mV), the peak at 2186 cm^{-1} reaches its maximum intensity while the two lower wavenumber peaks tend to form a broad, low intensity region.

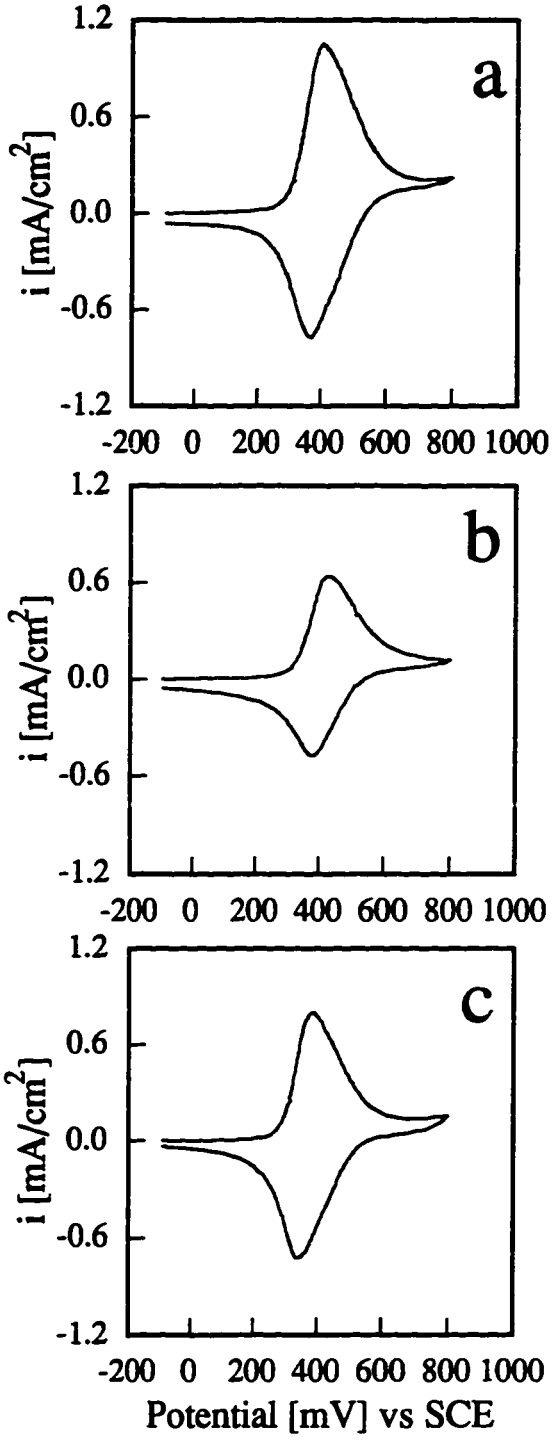

Figure 6.1. Initial cyclic voltammograms from freshly prepared derivatized electrodes a) A, b) B, and c) C.

Spectra from the freshly prepared electrodes (Figure 6.2) show that not all of the NiHCF derivatized electrodes start with the same intrinsic ability to switch from a reduced form to a fully oxidized form. For a fully redox active electrode, switching the potential from -100 mV to +779 mV causes the two low wavenumber peaks to essentially disappear while the signal from the 2186 cm^{-1} becomes the predominant feature of the spectrum.[91] Although all three electrodes shown in Figure 6.2 have similar Raman spectra for the reduced NiHCF film, the prominence of the 2186 cm^{-1} peak at oxidizing potentials is seen to vary considerably. Electrode A achieves a highly oxidized state (a high intensity 2186 cm^{-1} peak), whereas electrode C displays only modest characteristics of an oxidized surface (a small 2186 cm^{-1} peak). This clearly shows the variation in the degree to which different NiHCF derivatized electrodes can be oxidized, even when fabricated under nominally identical conditions.

In the last chapter, a principal component regression (PCR) model was developed to quantify the fractional oxidation state (x) of the derivatized surface film. A value of x=0 corresponds to all the iron-centers in the film being in the reduced (ferrous) state, while a value of x=1 corresponds to a fully oxidized lattice comprised of ferric iron. Applying the PCR model to the spectra in Figure 6.2 allows one to calculate the oxidation state of electrode (x). For example, electrode A switches from x=0.00 at -100 mV to x=0.93 at +779 mV. The difference between the fraction oxidized when held at oxidative and reducing potentials (Δx=0.93-0.00) is the quantity we term the redox activity of the derivatized electrode. The redox activity characterizes the fraction of iron centers that can reversibly switch between Fe^{II} and Fe^{III}. For the freshly prepared electrodes shown in Figure 6.1 and Figure 6.2, Δx is 0.93, 0.77, and 0.43 for films A, B, and C, respectively.

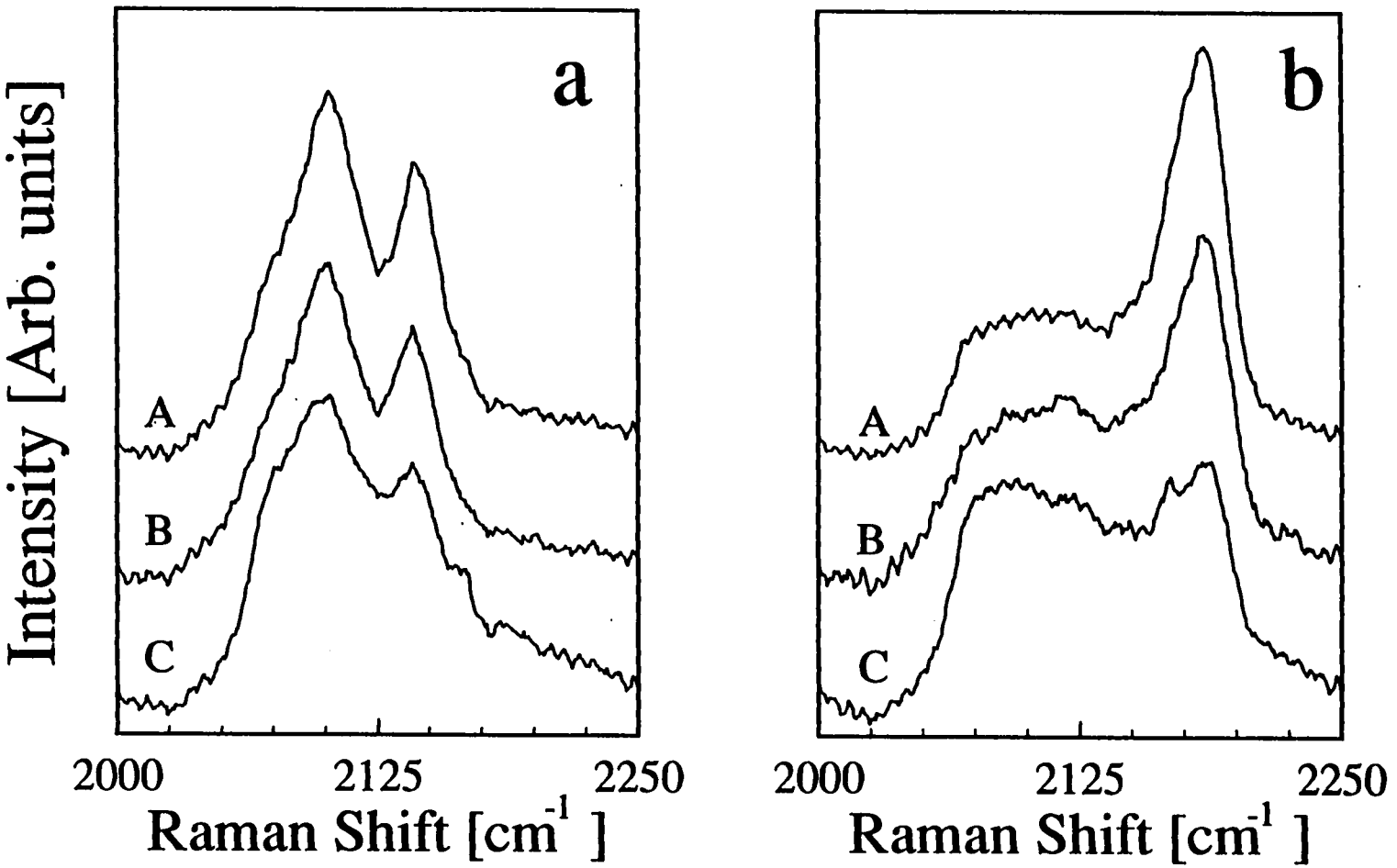

Figure 6.2. Raman spectra from the freshly prepared electrodes shown in Figure 6.1 in a) reduced and b) oxidized states.

The electrochemical ion exchange capacity of a derivatized electrode (q) depends on the total amount of NiHCF on the electrode multiplied by the average redox activity of the derivatized layer, *i.e.*

$$q = F N_{NiHCF} \Delta x_{ave} \qquad (6.2)$$

where F is Faraday's constant, N_{NiHCF} is the number of moles of NiHCF per unit area of electrode, and Δx_{ave} is the average redox activity of the derivatized layer. As one might expect from Eq. (6.2), electrode A has the highest electrochemical capacity and also the largest Δx. Paradoxically, electrode B has the lowest electrochemical capacity but not the lowest redox activity, and electrode C has the lowest redox activity but not the lowest electrochemical capacity. This paradox is either due to electrode B having a thinner derivatized layer than C, or the redox activity of the derivatized layer is spatially nonuniform. If the redox activity is nonuniform, then the area sampled by Raman spectroscopy (about 1% of the total electrode area) may not represent the average redox activity of the entire electrode. In other words, Δx measured by Raman spectroscopy may not be identical to Δx_{ave} if the derivatized layer is nonuniform We will consider the uniformity of the derivatized layer at some length a later in this chapter.

Figure 6.3 shows the electrochemical response of electrodes A, B, and C after many thousands of potential cycles. Film A has been cycled 5800 times; film B has been cycled 2000 times; and film C has been cycled 8000 times. Repeated potential cycling distorts all of the CV's significantly from the initial CV's (shown as dashed curve). The maximum and minimum currents in each sweep have decreased, and the oxidation and reduction peaks have become less clearly defined. Figure 6.3 shows that after repeated redox cycling, these electrodes have undergone some sort of degradation. The electrochemical capacities of electrodes A, B, and C are 25%, 100%, and 17% of their initial values, respectively, after long term cycling. Note that although the electrochemical

capacity of electrode B has apparently not changed, the form of the CV giving rise to this total charge clearly shows that degradation has occured. The calculation of q is not sufficiently descriminating to reveal this change. According to Eq. (6.2), the loss in electrochemical capacity can only be due to two modes of decay: the electrode may physically lose NiHCF from the surface, and/or the NiHCF may lose its redox activity so it no longer switches between reduced and oxidized states. Raman spectra can give insight into these two degradation modes.

Figure 6.4 shows the Raman spectra of electrodes A, B, and C at reducing and oxidizing potentials after long term potential cycling (the spectra are from the same spatial locations as in Figure 6.2). Electrode A's spectra show little change from the fully active film response given in Figure 6.2, even though the electrochemical capacity has declined by 75%. The spectra for electrodes B and C show substantial changes from the spectra in Figure 6.2. Most notably, the spectra at oxidizing potentials in Figure 6.4 do not display as prominent a 2186 cm^{-1} peak as the spectra in Figure 6.2; cycling electrodes B and C apparently causes them to not switch into the oxidized state as easily as they did initially. Using the PCR model, one finds that electrodes A, B, and C attain values of x=0.02, 0.19, and 0.18, respectively, at reducing potentials, while x=0.86, 0.39, and 0.25 at oxidizing potentials. These results yield redox activities of Δx=0.84, 0.20, and 0.07, for electrodes A, B, and C when they have been repeatedly cycled. After cycling, the electrodes retain 90%, 26%, and 15% of their initial redox activity. It is clear that the degradation of the ion exchange capacity of NiHCF derivatized electrodes subjected to repeated potential cycles is due, at least in part, to a loss of redox activity within the derivatized film.

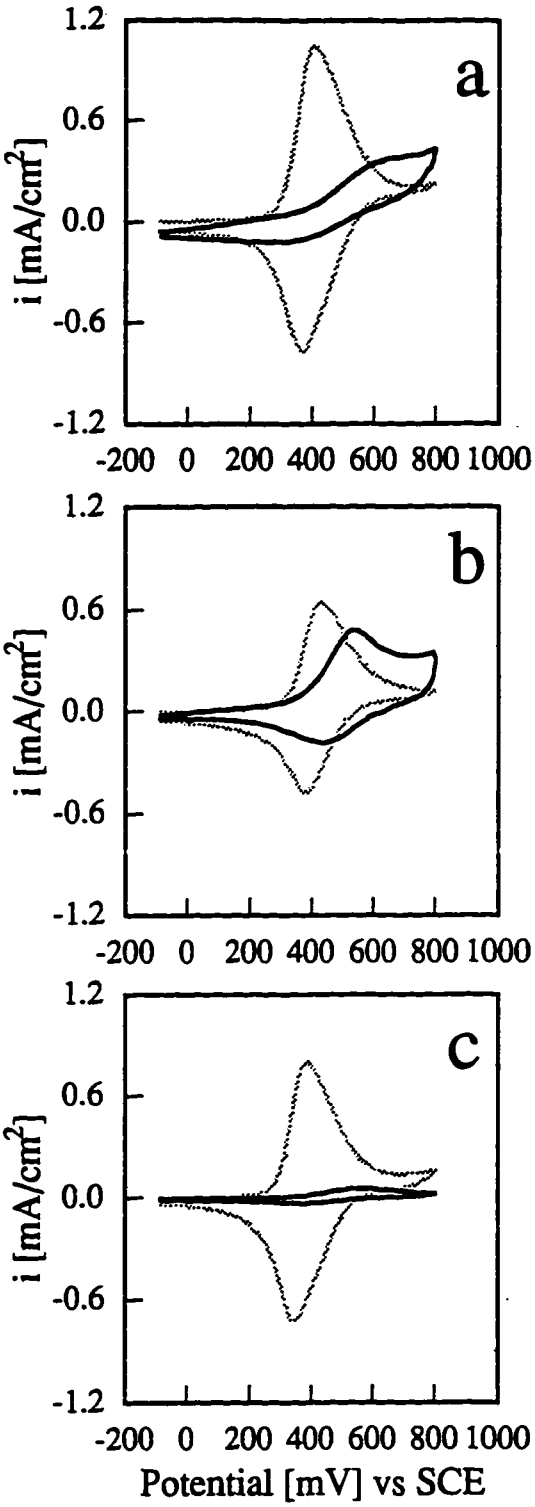

Figure 6.3. Cyclic voltammograms after redox cycling from films a) A (5800 cycles), b) B (2000 cycles), and c) C (8000 cycles). Dotted curves show the fresh film response.

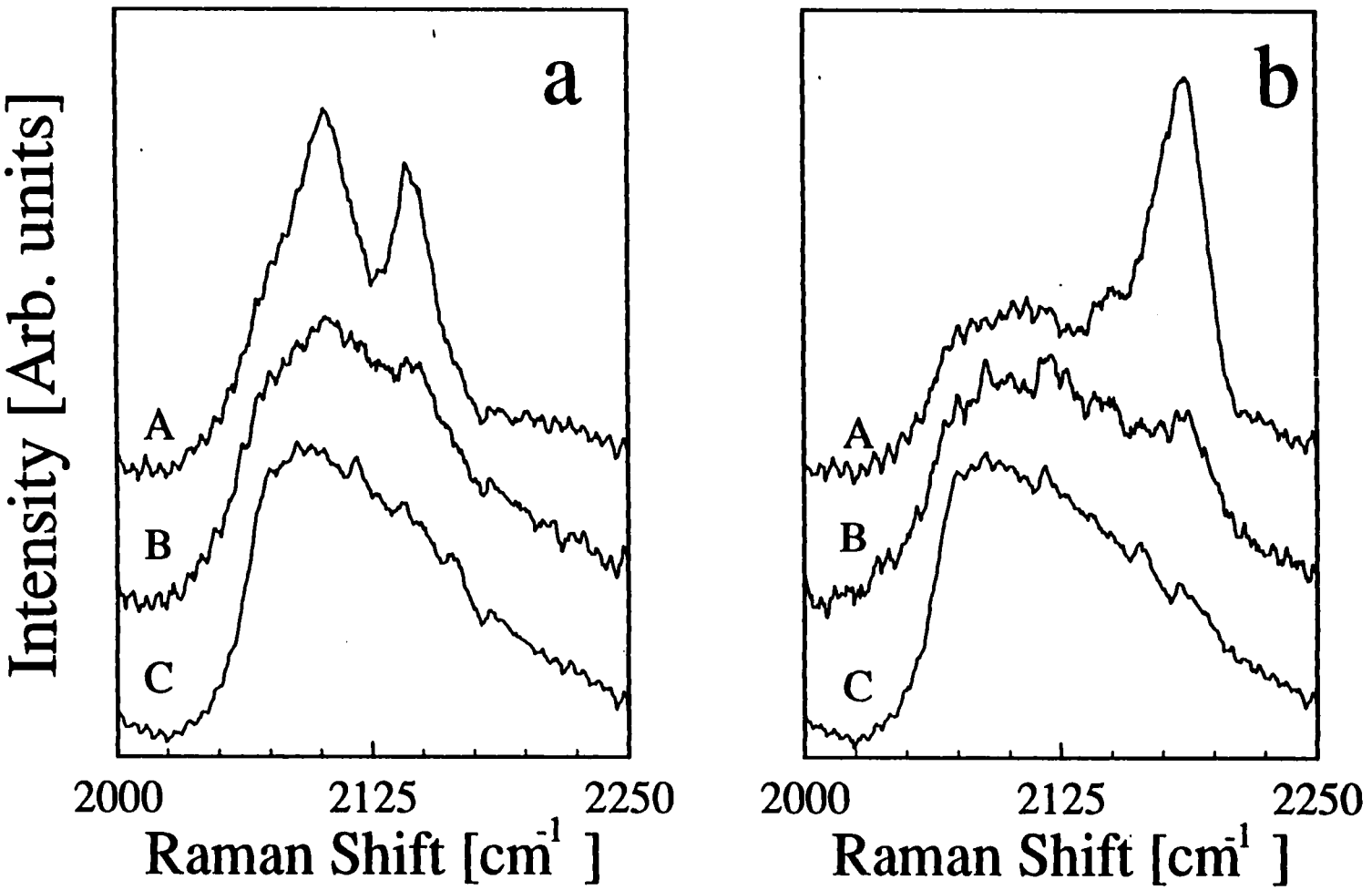

Figure 6.4. Raman spectra from the cycled films shown in Figure 6.3 in a) reduced and b) oxidized states.

The data for electrode B in Figure 6.1 through Figure 6.4 provide strong evidence that the surfaces of NiHCF derivatized electrodes have spatially nonuniform redox activity. The quantity N_{NiHCF} can only become smaller in Eq. (6.2) as the electrode is cycled in $NaNO_3$ electrolyte. Thus, if the *average* redox activity of the NiHCF layer decreases, the electrochemical capacity must also decrease by at least as much. Electrode B is seen to retain essentially 100% of its electrochemical capacity, but only 26% of its redox switching activity (as measured by Raman spectroscopy on 1% of the electrode area). Accordingly, the 1% of the area probed on electrode B cannot represent the average redox activity of the electrode, otherwise the electrode would maintain a maximum of 26% of its initial electrochemical capacity. For electrode B, Raman spectroscopy is measuring a region of the electrode where the redox activity decayed much more quickly than the electrode as a whole.

Analyzing the results from Figure 6.1 through Figure 6.4 for electrodes A is not as straightforward as analyzing electrode B. For electrode A, the difference between the percent of the electrochemical capacity retained (25%) and the percent redox activity retained (90%) can be explained by either a large loss of NiHCF from the electrode or by assuming the film is nonuniform and the measured Δx does not equal Δx_{ave}. To fully account for the differences in electrochemical capacity and redox activity retained, 73% of the NiHCF present on the surface initially would have been removed from the electrode upon cycling. If this much material was removed from the electrode, it is probable that the Raman intensity would have declined appreciably, but it did not. We therefore infer that electrode A also has a nonuniform derivatized layer and the measured 1% of the electrode has a Δx that deviates from the average redox activity. For electrode A, the region measured by Raman spectroscopy retains more redox activity than the electrode as a whole.

Analyzing the data for electrode C shows that the electrochemical capacity declined to 17% of the initial value while the redox activity measured by Raman spectroscopy declined to 15% of the original level. The agreement between the electrochemical and redox activity of electrode C suggests that the region of the electrode being probed by Raman spectroscopy is characteristic of the average electrode response; because of this, we will further consider the electrochemical and cycle life behavior of electrode C.

Figure 6.5 shows the cycle life evolution of electrochemical capacity, redox activity, and Raman signal intensity from electrode C over a total of 8000 potential cycles. Each of these measures of electrode performance are normalized by the initial values obtained from the freshly prepared derivatized electrode. The normalized Raman signal intensity is a measure of the relative amount of material on the electrode surface, since the entire thickness of the NiHCF film is being probed by the 647.1 nm laser light.[91]

The normalized electrochemical capacity (Figure 6.5, solid curve) declines smoothly except at points where Raman spectra are taken (every 2000 cycles). These step losses in electrochemical capacity result from holding the film at fixed potentials for extended periods of time while acquiring Raman data, suggesting that the method used to modulate the potential can significantly impact the degradation rate of the derivatized surface. (*N.B.* We reported in Chapter 5 that laser irradiation with 647.1 nm light does not result in reversible damage to the derivatized layer. Moreover, even if the impinging laser irradiation did destroy the film, the irradiated area is only ≈1% of the total electrode area, and would not be seen in the measure of electrochemical capacity.)

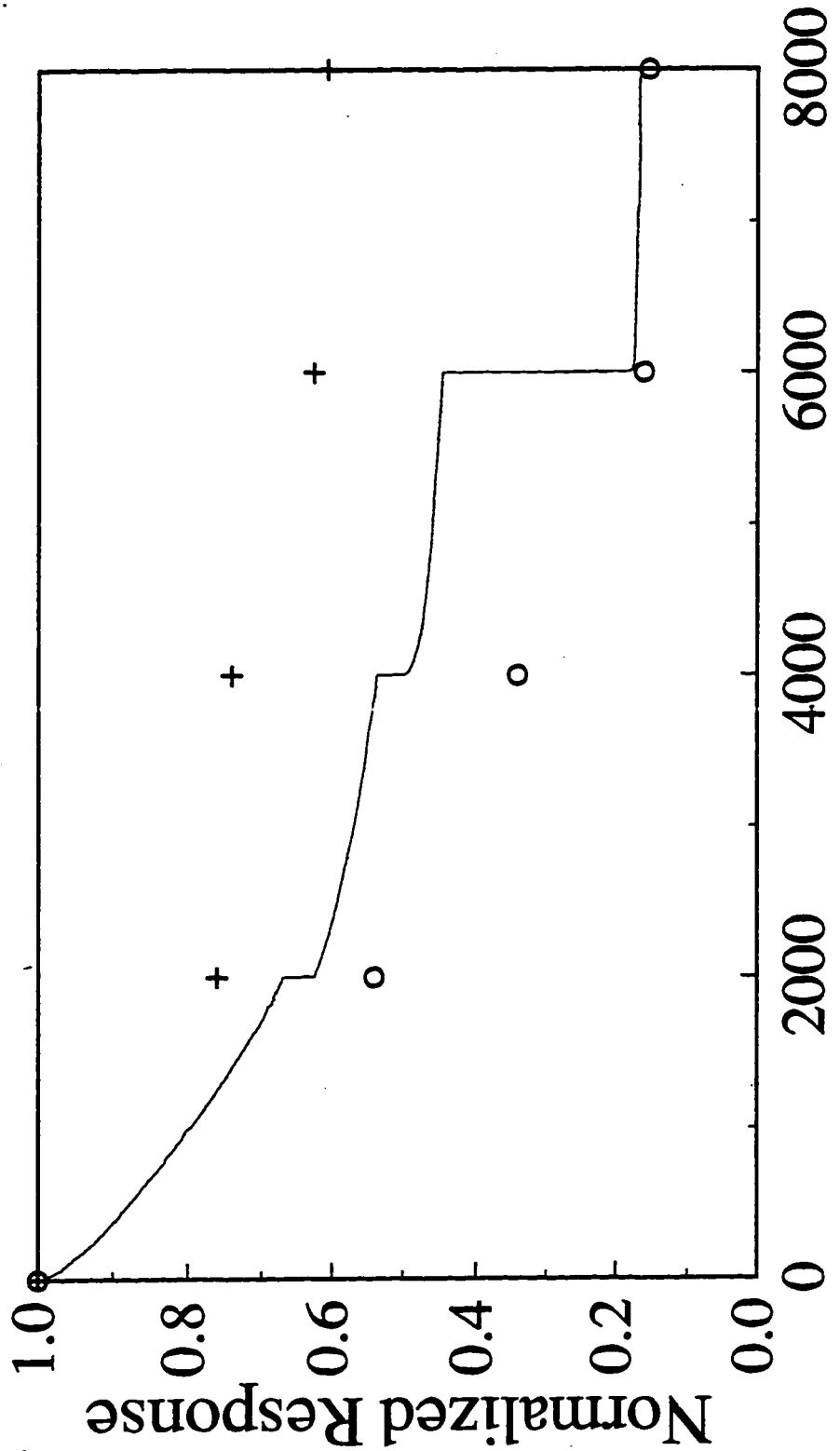

Figure 6.5. Plot of the normalized electrochemical ion exchange capacity (—), redox activity (O), and Raman scattering intensity (+) as a function of cycle for film C.

Figure 6.5 shows that the electrochemical capacity appears to decline mainly due to a drop in redox activity (Figure 6.5, O). The physical loss of film, as measured by the decline in Raman signal strength (Figure 6.5, +), is a smaller part of the degradation mechanism. The main conclusion that can be drawn from Figure 6.1 through Figure 6.5 is that degradation of electrochemical ion exchange capacity is mainly due to a loss in redox activity and not due to film loss. A more quantitative measurement of film loss rates should be performed using a quartz crystal microbalance, but these facilities are not presently available in our laboratory.

6.4.2 Spatially resolved oxidation state profiling.

Figure 6.1 through Figure 6.5 support the notion that derivatized electrodes have nonuniform redox activity over length scales greater than the ≈1 mm long laser excitation line probed by the Raman instrument. The evidence for long range nonuniformity of the derivatized layer is fairly strong, but we have yet to assess the uniformity of redox switching at the micron scale. As described in Chapter 5, line-imaging Raman spectroscopy appears to be an excellent tool for such studies. Using line-imaging Raman spectroscopy, 256 spectra can be acquired simultaneously at adjacent locations every ≈5 μm along the derivatized electrode surface. Applying the PCR model developed previously to these line-images allows spatial profiles of the iron-center oxidation states (x) to be constructed along a ≈1200 μm line traversing the derivatized electrode surface. Figures 6(a-e) show oxidation state profiles collected from electrode C after consecutive sets of 2000 cycles, as well as the intensity profile of the scattered light (Figure 6.6f). Oxidation state profiles are shown for the reduced (light pen), intermediate (medium pen) and oxidized (heavy pen) electrode after each set of 2000 cycles. Many of the general features seen in Figure 6.6 have been discussed in Chapter 5. For example, several spatial locations are seen to have noisy predicted values of x caused by anomalous scattering from

the electrode's surface, and the oxidation state profile has a smooth "hump" when the derivatized layer is oxidized (x is high in the middle and lower at each edge).

Figure 6.6 shows a fairly uniform decline in redox activity as potential cycling progresses. Ultimately, the derivatized layer becomes unresponsive to the applied potential (see Figure 6.6d and Figure 6.6e), reaching a *spatially uniform* terminal oxidation state near x=0.2. Every NiHCF derivatized electrode that we have cycled until degraded has converged to a spatially uniform value of x≈0.2, indicating the population of iron-centers in the lattice tends toward a uniform 4:1 ratio of Fe^{II} to Fe^{III} after repeated cycling. Thus, line-imaging Raman spectroscopy has provided a key new insight into the degradation mechanism; the derivatized layer does not simply degrade in microscopic patches, but instead, reaches a spatially uniform terminal state made up mainly of reduced iron. In this terminal state, the NiHCF lattice is 80% filled with intercalated cations. At present, we do not know precisely what chemical or structural transformation causes derivatized electrodes to universally degrade to the x=0.2 state; this remains a current research topic.

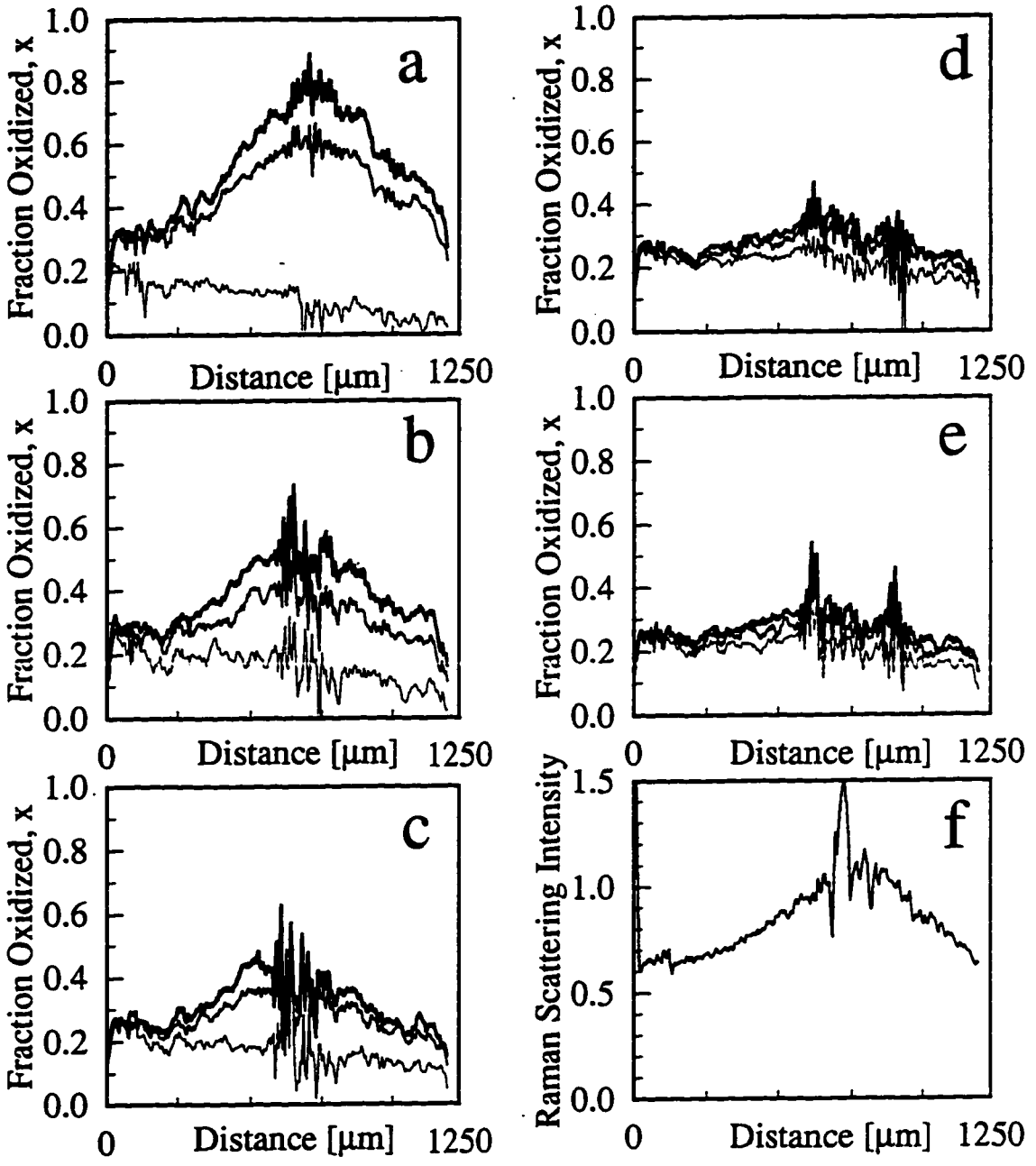

Figure 6.6. Oxidization state profiles for film C in reduced (-100mV), intermediate (+451mV), and oxidized (+801mV) states after a) 0, b) 2000, c) 4000, d) 6000, and e) 8000 redox cycles. f) The Raman scattering intensity for a) at +801 mV.

6.4.3 Preliminary studies of NiHCF photochemistry

In Chapter 5, we demonstrated that the characteristic "hump" in the oxidation state profile of NiHCF held at oxidizing potentials is a real feature of the underlying spectra, not an artifact of the PCR model. Nevertheless, the oxidation state "hump" is observed for essentially all NiHCF derivatized layers that have redox activity, and the shape of the "hump" normally matches the shape of the Raman intensity profile (*cf.* Figure 6.6a and Figure 6.6f, and Figure 5.6 and Figure 5.8). On the other hand, the oxidation state profiles for electrodes that are in a reduced state are flat and do not have the scattering intensity profile superimposed (see Figure 5.6 and Figure 5.8). Since the Raman scattering intensity profile mainly reflects the Gaussian intensity profile of the incident laser excitation, it is worthwhile exploring the role of laser illumination on charge transfer in NiHCF derivatized electrodes to see if photoelectrochemical effects may account for the oxidation state "hump" seen for oxidized electrodes.

We have performed some preliminary studies to assess the role of photochemistry in NiHCF derivatized electrodes. The photoelectrochemical response of NiHCF was investigated using 0.5 Hz chopped laser irradiation at 647.1 nm. For these studies, we derivatized a small electrode of area $\approx 2 \times 10^{-3}$ cm^2 so that the entire derivatized surface could be illuminated. Figures 7a and 7b show the CV of this electrode in the dark and when illuminated with chopped laser irradiation, respectively. The incident laser light obviously perturbs charge transfer in the derivatized film. The photoresponse shown in Figure 6.7b suggests that laser illumination enhances the rate of charge transfer reaction (6.3) *via* a photo-enhancement of the lattice conductivity, since the anodic and cathodic photocurrents are roughly in proportion to the corresponding dark currents. These preliminary results suggest that charge transfer in NiHCF may be limited by electron

transport in the lattice, as has been found for Prussian Blue,[92] rather than by ionic transport.

An alternative explanation for how 647.1 nm laser light may alter the oxidation state of iron-centers in NiHCF involves intramolecular charge transfer across the CN bridge between Fe and Ni. In cobalt hexacyanoferrate (CoHCF) compounds, illumination with red light at 660 nm has been shown to promote intramolecular charge transfer, *i.e.*,[4,5]

$$Fe^{II}\text{-}CN\text{-}Co^{III} + h\nu \rightarrow Fe^{III}\text{-}CN\text{-}Co^{II} \qquad (6.3)$$

It is well known that the CN bridge in hexacyanoferrate compounds are facile charge conductors.[93] Three CN vibrational modes have been reported in CoHCF containing interstitial K^+: 2097, 2116, and 2162 cm^{-1}. In low temperature experiments, exposure to filtered red light caused the 2116 cm^{-1} peak to decrease and the 2162 cm^{-1} peak to increase, indicating that illumination increased the population of Fe^{III} in the CoHCF lattice.[5]

Figure 6.8 shows the room temperature Raman spectra for a NiHCF derivatized electrode exposed to 100%, 50%, and 10% of full laser power. Signal acquisition times were ~100 s, 200 s, and 1000 s for incident intensities of 100%, 50% and 10%, respectively. The Raman spectra from derivatized electrodes held in the reduced state have no apparent dependence on the laser illumination intensity. On the other hand, derivatized electrodes held in the oxidized state display a new peak at 2125 cm^{-1} when the electrode is illuminated at low intensities. Though preliminary in nature, Figure 6.8 seems to show that NiHCF displays an intramolecular charge transfer process that may have some similarity to Eq. (6.3). Although we have identified two ways in which laser illumination may cause NiHCF to become more oxidized in the intense center of the laser beam, more work is needed to confirm whether either of these mechanisms is indeed the origin of the oxidation state "hump" observed in profiles like Figure 6.6.

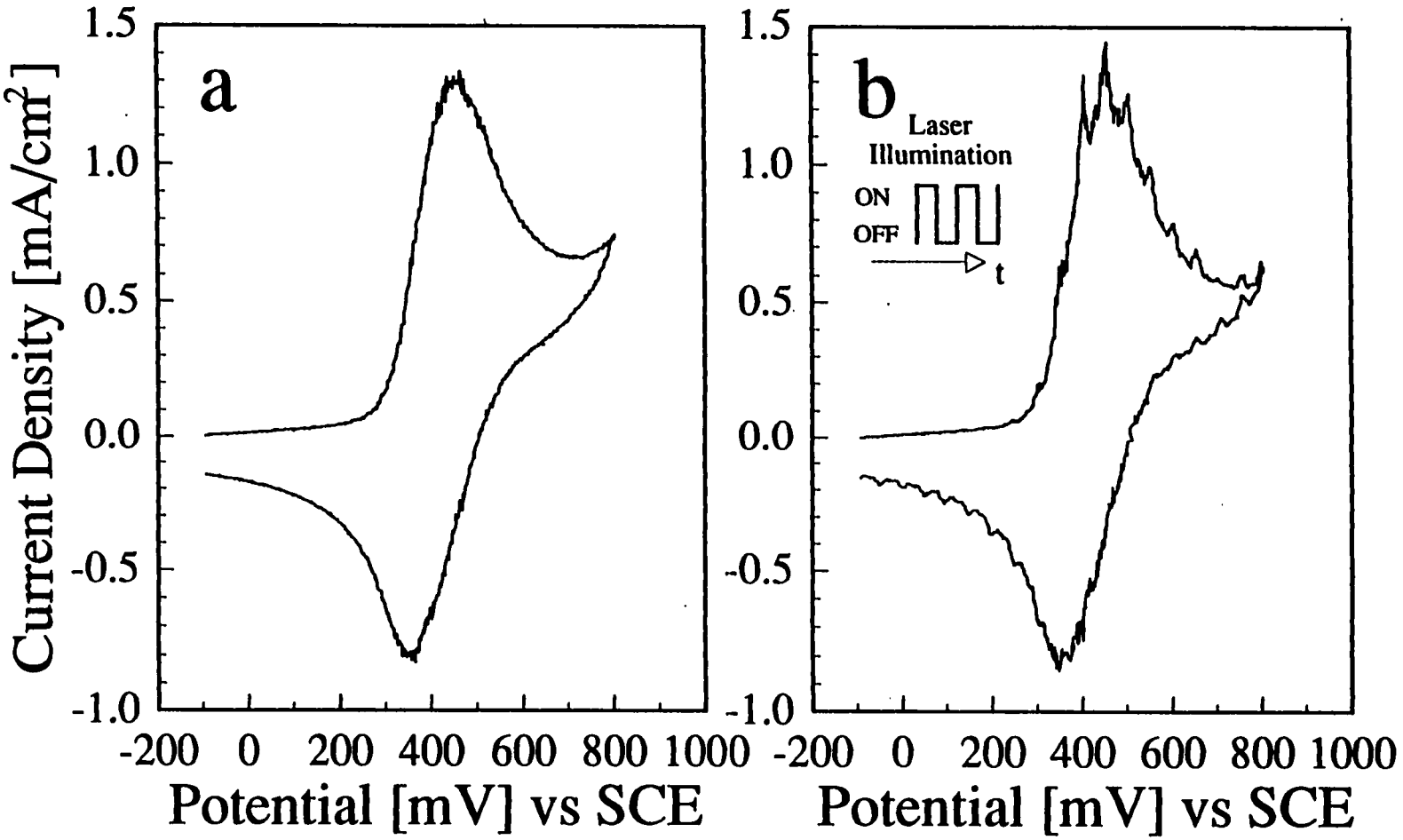

Figure 6.7. Cyclic voltammograms of a microelectrode derivatized with a thin film of nickel hexacyanoferrate a) without laser illumination and b) with laser illumination chopped at ≈0.5 Hz. Sweep rate = 50 mV/s.

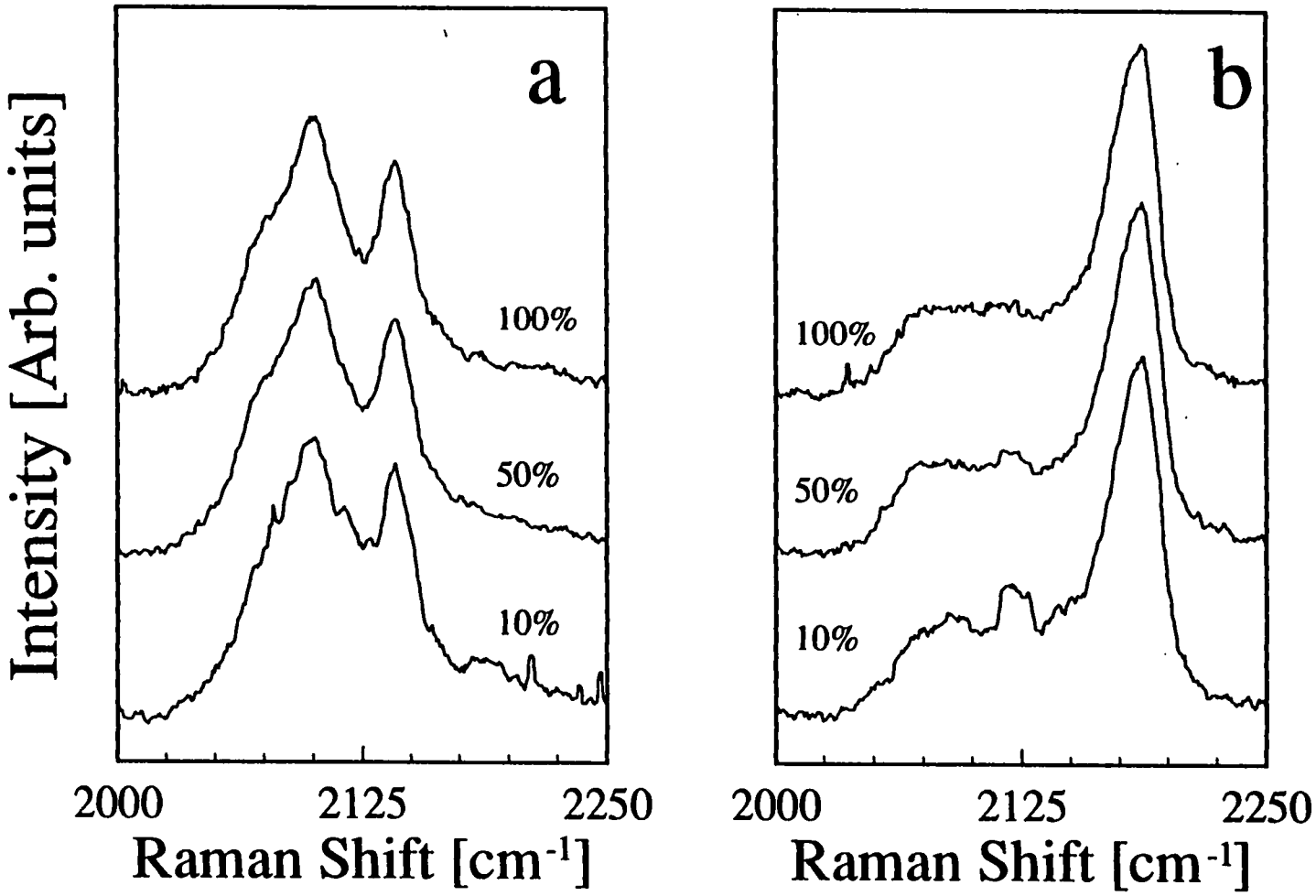

Figure 6.8. Raman spectra from freshly prepared electrodes in a) reduced (-100mV) and b) oxidized (+801mV) states exposed to different laser intensity levels of 100%, 50%, and 10% of full power.

6.5 Conclusions

Raman spectroscopy has been coupled with a multivariate PCR model to show that NiHCF derivatized electrodes degrade mainly *via* a loss of redox activity in the derivatized film when cycled in 1 M $NaNO_3$. As the derivatized electrode loses its ability to modulate between reduced and oxidized states, the NiHCF tends to converge to a spatially uniform reduced state where the ratio of Fe^{II} to Fe^{III} is approximately 4:1. Although not the primary degradation mode, evidence is given that the physical loss of NiHCF from the derivatized electrode also contributes to the degradation of the electrochemical ion exchange capacity. The degradation of the derivatized layer occurs nonuniformly, with some regions of the electrode declining faster than the average electrode, and some regions maintaining redox activity even when most of the electrochemical capacity has been lost. The degradation rate of the derivatized electrode is shown to be accelerated by stepping and holding the potential between oxidizing and reducing values, instead of continuously sweeping the potential. It is also shown that the 647.1 nm incident laser perturbs the NiHCF derivatized layer. Laser illumination promotes a photoconductive response in the NiHCF as well as a spectral change at varying incident intensities.

CHAPTER 7: CONCLUSIONS AND RECOMMENDATIONS

Presented in this dissertation is the construction and use of a line-imaging Raman spectroscopy instrument for electrochemical systems. This instrument is shown to be able to collect spectral information continuously over a macroscopic distance. The region to be imaged can be normal to an electrode surface in order to simultaneously probe from the bulk solution, through the concentration boundary layer, onto a depositing thin film. The imaging region can also collect spectra along a surface to gather chemically specific information over a macroscopic distance.

Two electrochemical systems were presented to demonstrate this technique's applicability to simultaneously probe solution phase and thin film chemistry. It was shown that a thin layer of electrodeposited CuSCN and the surrounding solution could be spatially and spectrally characterized with sufficient resolution for many electrochemical systems. Also, the concentration boundary layers resulting from the electrodeposition of copper at various deposition rates were directly imaged. These images were used to spatially profile a specific chemical species *in situ* during the electrodeposition. The free convective flow resulting from this deposition does not afford the degree of control that is required for long Raman exposures. Future efforts should address the need to establish a stable, known flow when imaging the solution.

For solution phase imaging, the excitation beam was focused to a line perpendicular to the beam propagation direction. A more efficient use of the beam would be to focus the expanded laser light with a high *f*-number spherical lens. Figure 7.1 shows this proposed optical arrangement. At the beam waist would result a long thin line of focused laser light. Raman scattered light could be collected from this portion of the focused beam, which maximizes used photons and provides a uniform intensity profile. This arrangement cannot be used to image along the surface of a sample however.

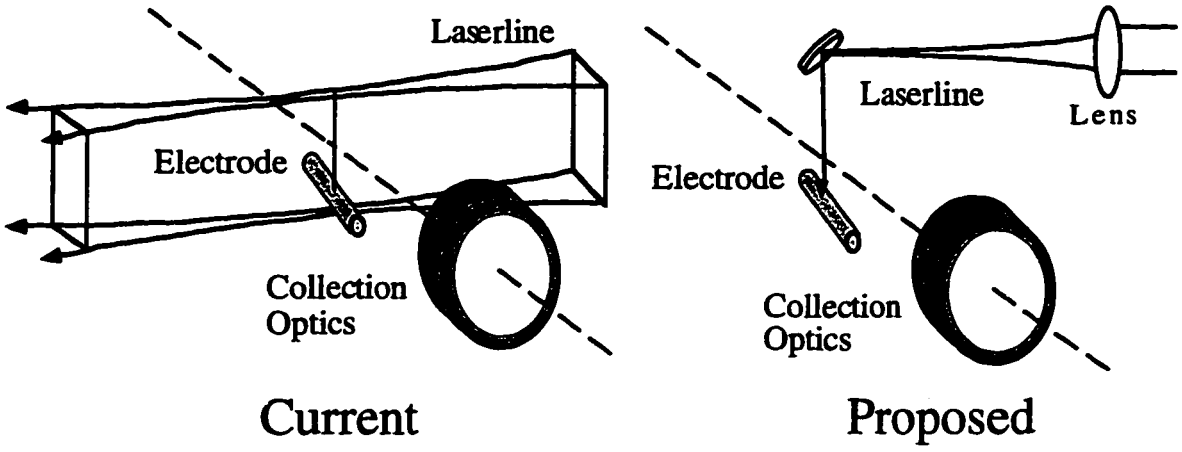

Figure 7.1. Current and proposed beam arrangement for solution phase imaging.

The surface profiling capabilities of the instrument were also demonstrated by imaging along the surface of thin films of nickel hexacyanoferrate. The Raman modes of this electroactive material were shown to be sensitive to the oxidation state, and a multivariate model was developed to correlate a Raman spectrum to the absolute oxidation state. Raman line-images were combined with the multivariate model to show how oxidation state varied across the surface of these thin films as the oxidation state was modulated. This property was spatially probed *in situ* in an electrochemical cell. A tremendous advantage of line-imaging spectroscopy over point spectroscopy was illustrated by showing how the spectral information gathered by this *in situ* nondestructive probe can be used to make predictions of some correlated quantity (*e.g.* oxidation state, internal stress, degree of polymerization, etc.), and used to create spatial profiles of that quantity.

The cycle life decay behavior of nickel hexacyanoferrate derivatized surfaces was also investigated with line-imaging Raman spectroscopy. It was shown that there can be variations in the ability of a derivatized surface to become fully oxidized or reduced. As the surface is repeatedly cycled from a reducing to an oxidizing potential, the derivatized surface's ion exchange capacity decreases. This loss can be attributed to physical loss of

material, and also the loss of ability to fully switch between reduced and oxidized states. Line-imaging Raman spectroscopy was able to show that although the surface responds nonuniformly to the applied potential, ultimately the surface decays to a nonreactive spatially uniform oxidation state.

It was also shown that nickel hexacyanoferrate exhibits a photoresponse when exposed to 647.1 nm laser light. From the oxidation state profiling studies, it was discovered that the Gaussian intensity beam profile is related to the oxidation state of the material. This could be due to a photoinduced intramolecular charge transfer between the iron and nickel centers. Although photoinduced effects have been verified with a point spectroscopy approach, attempts to exactly reproduce the effect seen with line-imaging have not been completely successful.

A few specific areas in need of improvement in the nickel hexacyanoferrate system can be identified. A high degree of variation in film response, electrochemically and spectroscopically, has been noticed. The state or nature of the nickel substrate derivatized by nickel hexacyanoferrate seems to play a crucial role in the final film character. A thorough study of the derivatization process and resulting film character would be beneficial to subsequent studies of cycle life behavior.

Also, the factors resulting from line-image normalization performed prior to application of a multivariate model potentially contain a wealth of information. An understanding of these factors has been developed in this work, but further study may provide key insight into scattering effects from the sample surface, and film thickness variations along the surface.

REFERENCES

(1) M. Matlosz, "Competitive Adsorption Effects in the Electrodeposition of Iron-Nickel Alloys" *Journal of the Electrochemical Society*, ***140***(8), 2272-2279, **1993.**

(2) S. Hessami and C.W. Tobias, "A Mathematical Model for Anomalous Codeposition of Nickel-Iron on a Rotating Disk Electrode" *Journal of the Electrochemical Society*, ***136***(12), 3611-3616, **1989.**

(3) K. Itaya, K. Shibayama, H. Akahoshi and S. Toshima, "Prussian-blue-modified Electrodes: An Application for a Stable Electrochromic Display Device" *Journal of Applied Physics*, ***53***(1), 804-805, **1982.**

(4) O. Sato, Y. Einaga, T. Iyoda, A. Fujishima and K. Hashimoto, "Reversible Photoinduced Magnetization" *Journal of the Electrochemical Society*, ***144***(1), L11-L13, **1997.**

(5) O. Sato, T. Iyoda, A. Fujishima and K. Hashimoto, "Photoinduced Magnetization of a Cobalt-Iron Cyanide" *Science*, ***272***(3 May), 704-705, **1996.**

(6) M.A. Lilga, R.J. Orth, J.H. Sukamto, S.M. Haight and D.T. Schwartz, "Metal ion Separations Using Electrically Switched Ion Exchange" *Separations Technology*, ***submitted.***

(7) S. Sinha, B.D. Humphrey and A.B. Bocarsly, "Reaction of Nickel Electrode Surfaces with Anionic Metal-Cyanide Complexes: Formation of Precipitated Surfaces" *Inorganic Chemistry*, ***23***,203-212, **1984.**

(8) A.B. Bocarsly and S. Sinha, "Chemically Derivatized Nickel Surfaces: Synthesis of a New Class of Stable Electrode Interfaces" *Journal of Electroanalytical Chemistry*, ***137***,157-162, **1982.**

(9) A.B. Bocarsly and S. Sinha, "Effects of Surface Structure on Electrode Charge Transfer Properties: Induction of Ion Selectivity at the Chemically Derivatized Interface" *Journal of Electroanalytical Chemistry*, ***140***,167-172, **1982.**

(10) B.D. Humphrey, S. Sinha and A.B. Bocarsly, "Mechanisms of Charge Transfer at the Chemically Derivatized Interface: The Ni/$[Ni^{II}(CN)Fe^{II/III}(CN)_5]^{2-/1-}$ System as an Electrocatalyst" *Journal of Physical Chemistry*, ***91***,586-593, **1987.**

(11) B.D. Humphrey, S. Sinha and A.B. Bocarsly, "Diffuse Reflectance Spectroelectrochemistry as a Probe of the Chemically Derivatized Electrode Interface. The Derivatized Nickel Electrode" *Journal of Physical Chemistry*, ***88***,736-743, **1984.**

(12) L.F. Schneemeyer, S.E. Spengler and W.D. Murphy, "Ion Selectivity in Nickel Hexacyanoferrate Films on Electrode Surfaces" *Inorganic Chemistry*, ***24***,3044-3046, **1985.**

(13) A. Roig, J. Navarro, J.J. Garcia and F. Vicente, "Voltammetric Study on the Stability of Deposited Prussian Blue Films against Successive Potential Cycling" *Electrochimica Acta*, ***39***(8), 437-442, **1994**.

(14) D.E. Stilwell, K.H. Park and M.H. Miles, "Electrochemical Studies of the Factors Influencing the Cycle Stability of Prussian Blue Films" *Journal of Applied Electrochemistry*, ***22***(4), 325-331, **1992**.

(15) B. O'Regan and D.T. Schwartz, "Efficient Photo-Hole Injection from Adsorbed Cyanine Dyes into Electrodeposited Copper(I) Thiocyanate Thin Films" *Chemistry of Materials*, ***7***(7), 1349-1354, **1995**.

(16) B. O'Regan and D.T. Schwartz, "Efficient Dye-sensitized Charge Separation in a Wide-band-gap *p-n* Heterojunction" *Journal of Applied Physics*, ***80***(8), 4749-4754, **1996**.

(17) H. Dahms and I.M. Croll, "The Anomalous Codeposition of Iron-Nickel Alloys" *Journal of the Electrochemical Society*, ***112***(8), 771-775, **1965**.

(18) S.A. Hendricks, Y.K. Kim and A.J. Bard, "Imaging of the In-Situ Deposition of Lead on Highly Oriented Pyrolytic Graphite by Scanning Tunneling and Atomic Force Microscopies" *Journal of the Electrochemical Society*, ***139***(10), 2818-2824, **1992**.

(19) M.F. Toney, J.G. Gordon, M.G. Samant, G.L. Borges, O.R. Melroy, D. Yee and L.B. Sorensen, " Underpotentially Deposited Thallium on Silver (111) by in situ Surface X-ray Scattering" *Physical Review B*, ***45***(16), 9362-9374, **1992**.

(20) S.T. Mayer and R.H. Muller, "Nucleation of Silver (1) Oxide Investigated by Spectroscopic Ellipsometry" *Journal of the Electrochemical Society*, ***135***(9), 2133-2142, **1988**.

(21) G.R.J. Robertson, J.L. Ord, D.J. de Smet and M.A. Hopper, "An Ellipsometric Study of Polyaniline Film Deposition and Conversion" *Journal of the Electrochemical Society*, ***136***(11), 3380-3384, **1989**.

(22) D.T. Schwartz and R.H. Muller, "Oxidation Films on Copper in Alkaline Media: Intensity Modulated Photoelectrochemical and Raman Spectroscopy Studies" *Surface Science*, ***248***,349-358, **1991**.

(23) R.L. McCreery and R.T. Packard, "Raman Monitoring of Dynamic Electrochemical Events" *Analytical Chemistry*, ***61***(13), 775A-789A, **1989**.

(24) F.R. McLarnon, R.H. Muller and C.W. Tobias, "Interferometric Study of Transient Diffusion Layers" *Electrochimica Acta*, ***21***,101-105, **1976**.

(25) C.C. Jan and R.L. McCreery, "High-Resolution Spatially Resolved Visible Adsorption Spectrometry of the Electrochemical Diffusion Layer" *Analytical Chemistry*, ***58***(13), 2771-2777, **1986**.

(26) R.C. Engstrom, S. Ghaffari and H. Qu, "Fluorescence Imaging of Electrode-Solution Interfacial Processes" *Analytical Chemistry*, ***64***(21), 2525-2529, **1992.**

(27) P. Hopper and G.K. Werner, "Characterization of the Chemical Architechture of Carbon-Fiber Electrodes. 3. Effect of Charge on the Electron-Transfer Properties of ECL Reactions" *Analytical Chemistry*, ***66***(13), 1996-2004, **1994.**

(28) J.W. Ager, D.K. Veirs and G.M. Rosenblatt, "Spatially Resolved Raman Studies of Diamond Films Grown by Chemical Vapor Deposition" *Physical Review B*, ***43***(8), 6491-6499, **1991.**

(29) J.W. Ager, D.K. Veirs, J. Shamir and G.M. Rosenblatt, "Laser Heating Effects in the Characterization of Carbon Fibers by Raman Spectroscopy" *Journal of Applied Physics*, ***68***(7), 3598-3608, **1990.**

(30) R.H. Dauskardt, D.K. Veirs and R.O. Ritchie, "Spatially Resolved Raman Spectroscopy of Transformed Zones in Magnesia-Partially-Stabilized Zirconia" *Journal of the American Ceramic Society*, *72*(7), 1224-1230, **1989.**

(31) W. Reckers, L. Hüwel, G. Grünfeld and P. Andresen, "Spatially Resolved Multispecies and Temperature Analysis in Hydrogen Flames" *Applied Optics*, ***32***(6), 907-1993, **1993.**

(32) S.P. Nandula, T.M. Brown, R.W. Pitz and P.A. DeBarber, "Single-Pulse, Simultaneous Multipoint Multispecies Raman Measurements in Turbulent Nonpremixed Flames" *Optics Letters*, ***19***(6), 414-416, **1994.**

(33) P.A. DeBarber, C.F. Hess, R.W. Pitz, S.P. Nandula, T.M. Brown and P.A. Skaggs, "Practical Applications in UV Raman Line Imaging of Water Vapor", in *Laser Applications in Combustion and Combustion Diagnostics II*, ***2122***, 83-93, SPIE - The International Society for Optical Engineering, **1994.**

(34) R. Vehring, H. Moritz, D. Neikamp, G. Schweiger and P. Heinrich, "Linear Raman Spectroscopy on Droplet Chains: A New Experimental Method for the Analysis of Fast Transport Processes and Reactions on Microparticles" *Applied Spectroscopy*, ***49***(9), 1215-1224, **1995.**

(35) D.K. Veirs, V.K.F. Chia and G.M. Rosenblatt, "Raman Spectroscopy Applications of an Imaging Photomultiplier Tube" *Applied Optics*, ***26***(17), 3530-3535, **1987.**

(36) R.B. Bird, W.E. Stewart and E.N. Lightfoot, Transport Phenomena; John Wiley and Sons: New York, 1960, p. 780.

(37) C.A. Drumm and M.D. Morris, "Microscopic Raman Line-Imaging with Principal Component Analysis" *Applied Spectroscopy*, ***49***(9), 1331-1337, **1995.**

(38) Y. Son, N.R. de Tacconi and K. Rajeshwar, "Photoelectrochemistry and Raman Spectroelectrochemistry of Cuprous Thiocyanate Films on Copper Electrodes in Acidic Media" *Journal of Electroanalytical Chemistry*, ***345***,135-146, **1993.**

(39) D.L. Smith and V.I. Saunders, "The Structure and Polytypism of the ß Modification of Copper(I) Thiocyanate" *Acta crystallographica. Section B, Structural crystallography and crystal chemistry*, ***B37***,1807-1812, **1981.**

(40) M. Kabesová, J. Kohout and J. Gazo, "Effect of the Bridging Mode of the Thiocyanate Group in Compounds on Infared Spectra" *Inorganica Chimica Acta*, ***31***,L435-L436, **1978.**

(41) J. Rannou and M. Chabanel, "Vibrational Study of Ionic Association in Aprotic Solvents. 8. Copper(I) Thiocyanate in Soft Donor Solvents" *Inorganic Chemistry*, ***24***,2319-2320, **1985.**

(42) S. Kakaç, W. Aung and R. Viskanta, Natural Convection, Fundamentals and Applications; Hemisphere Publishing Corporation: New York, 1985, p. 1181.

(43) F.R. McLarnon, R.H. Muller and C.W. Tobias, "Light-Deflection Errors in the Interferometry of Electrochemical Mass Transfer Boundary Layers" *Journal of the Electrochemical Society*, ***122***(1), 59-64, **1975.**

(44) J.K. Weaver, F.R. McLarnon and E.J. Cairns, "Experimental and Theoretical Study of Concentration Distributions in a Model Pore Electrode" *Journal of the Electrochemical Society*, ***138***(9), 2572-2579, **1991.**

(45) R.H. Muller, Double Beam Interferometry for Electrochemical Studies; John Wiley and Sons: New York, 1973; Vol. 9, p. 542.

(46) R.H. Muller and C.G. Smith, "Ellipsometry of Mass-Transport Boundary Layers" *Surface Science*, ***56***,440-448, **1976.**

(47) S.M. Haight and D.T. Schwartz, "*In Situ* Imaging Raman Spectroscopy of Electrochemically Deposited CuSCN" *Journal of the Electrochemical Society*, ***142***(9), L156-L158, **1995.**

(48) I.R. Barkshire, J.M. Walton and M. Prutton, "Testing the Success of Analytical Image Correction Routines: Surface Images" *Surface and Interface Analysis*, ***20***,583-588, **1993.**

(49) M. Prutton, I.R. Barkshire, M.M. El Gomati, J.C. Greenwood, P.G. Kenny and R.H. Roberts, "The Use of Metal/Semiconductor Structures to Develop MULSAM Analytical Techniques" *Surface and Interface Analysis*, ***18***,295-302, **1992.**

(50) A.L.D. Beckers, W.C. De Bruijn, E.S. Geselma, M.I. Cleton-Soeteman and H.G. Van Eijk, "Quantitative Electron Spectroscopic Imaging in Bio-medicine: Methods for Image Acquisition, Correction and Analysis" *Journal of Microscopy*, ***174***(3), 171-182, **1994.**

(51) W.D. Erwin, M.W. Groch, A. Ali and E.W. Fordham, "Image Normalization and Background Subtraction in Tl-201/Tc-99m Parathyroid Subtraction Scintigraphy Effect on Lesion Detection" *Clinical Nuclear Medicine*, ***17***(2), 81-89, **1992.**

(52) J.Q. Luo and K.F. Koral, "Background-adaptive Dual-energy-window Correction for Compton Scattering in SPECT" *Nuclear Instruments and Methods in Physics Research, Section A, **353**,340-343, **1994**.*

(53) D.L. Wilson, K.S. Kump, S.J. Eppell and R.E. Marchant, "Morphological Restoration of Atomic-Force Microscopy Images" *Langmuir, **11**(1), 265-272, **1995**.*

(54) V.Y. Yurov and A.N. Klimov, "Correction of Drift and Slope Distortions in STM Image and Scanner Calibration" *Surface and Interface Analysis, **22**,84-88, **1994**.*

(55) N. Bonnet, S. Dongmo, P. Vautrot and M. Troyon, "A Mathemetical Morphology Approach to Image-Formation and Image-Restoration in Scanning Tunneling and Atomic-Force Microscopies" *Microscopy Microanalysis Microstructures, **5**(4-6), 477-487, **1994**.*

(56) Z. Zolnai, S. Macura and J.L. Markley, "Spline Method for Correctiong Baseplane Distortions in Two-Dimensional NMR Spectra" *Journal of Magnetic Resonance, **82**,496-504, **1989**.*

(57) W. Dietrich, C.H. Rüdel and M. Neumann, "Fast and Precise Automatic Baseline Correction of One- and Two-Dimensional NMR Spectra" *Journal of Magnetic Resonance, **91**,1-11, **1991**.*

(58) P. Güntert and K. Wüthrich, "FLATT - A New Procedure for High-Quality Baseline Correction of Multidimensional NMR Spectra" *Journal of Magnetic Resonance, **96**,403-407, **1992**.*

(59) F. Bridges, C.H. Booth and G.G. Li, "An Iterative Approach to "Atomic Background" Removal in XAFS Data Analysis" *Physica B, **208&209**,121-124, **1995**.*

(60) M. Newville, P. Livins, Y. Yacoby, J.J. Rehr and E.A. Stern, "An Improved Background Removal Method for XAFS" *Japanese Journal of Applied Physics, **Suppl. 32-2**,125-127, **1993**.*

(61) P.A. Mosier-Boss, S.H. Leibermann and R. Newberry, "Fluorescence Rejection in Raman Spectroscopy by Shifted-Spectra, Edge Detection, and FFT Filtering Techniques" *Applied Spectroscopy, **49**(5), 630-638, **1995**.*

(62) K.L. Aminov and J.B. Pedersen, "Analytical Background Correction in Numerical Fourier Transform Proceedures. Application to Electron Spectroscopy" *Surface and Interface Analysis, **23**,717-722, **1995**.*

(63) A.W.J. Moore and J.W. Jorgenson, "Median Filtering for Removal of Low-Frequency Background Drift" *Analytical Chemistry, **65**(2), 188-191, **1993**.*

(64) A. Rouh, M.-A. Delsuc, G. Bertrand and J.-Y. Lallemand, "The Use of Classification in Baseline Correction of FT NMR Spectra" *Journal of Magnetic Resonance, **Series A, 102**,357-359, **1993**.*

(65) S.R. Sternberg, "Biomedical Image Processing" *Computer*, ***16***(22), 22-34, **1983**.

(66) G.A. Pearson, "A General Baseline-Recognition and Baseline-Flattening Algorithm" *Journal of Magnetic Resonance*, ***27***,265-272, **1977**.

(67) C.A. Hayden and M.D. Morris, "Effects of Sampling Parameters on Principal Components Analysis of Raman Line Images" *Applied Spectroscopy*, ***50***(6), 708-714, **1996**.

(68) J.C. Russ, The Image Processing Handbook; CRC Press: London, 1992, p. 445.

(69) C. Loos-Neskovic and M. Fedoroff, "Decontamination of Nuclear Wastes by Fixation of Radioactive Elements on Ferrocyanides" *Radioactive Waste Management and the Nuclear Fuel Cycle*, ***11***(4), 347-364, **1989**.

(70) A. Hugot-Le Goff and M.C. Bernard, "Protonation and Oxidation Processes in Polyaniline Thin Films Studied by Optical Multichannel Analysis and *in situ* Raman Spectroscopy" *Synthetic Metals*, ***60***,115-131, **1993**.

(71) H. Oshio, T. Ama, T. Watanabe, J. Kincaid and K. Nakamoto, "Structure Sensitive Bands in the Vibrational Spectra of Metal Complexes of Tetraphenylporphine" *Spectrochimica Acta Part A*, ***40***(9), 863-870, **1984**.

(72) S. Kuwabata, K. Mitsui and H. Yoneyama, "Preparation of Polyaniline Films Doped with Methylene Blue-Bound Nafion and the Electrochromic Properties of the Resulting Films" *Journal of Electroanalytical Chemistry*, ***281***,97-107, **1990**.

(73) D. Ellis, M. Eckhoff and V.D. Neff, "Electrochromism in the Mixed-Valence Hexacyanides. 1. Voltammetric and Spectral Studies of the Oxidation and Reduction of Thin Films of Prussian Blue" *Journal of Physical Chemistry*, ***85***(9), 1225-1231, **1981**.

(74) W.E. O'Grady, K.I. Pandya, K.E. Swider and D.A. Corrigan, "*In Situ* X-ray Absorption Near-Edge Structure Evidence for Quadrivalent Nickel in Nickel Battery Electrodes" *Journal of the Electrochemical Society*, ***143***(5), 1613-1616, **1996**.

(75) K. Nakamoto, Infared and Raman Spectra of Inorganic and Coordination Compounds; 4th ed.; John Wiley & Sons: New York, 1986, p. 273.

(76) L.H. Jones, Inorganic Vibrational Spectroscopy; Marcel Dekker, Inc.: 1971; Vol. 1, p. 127.

(77) C.M. Stellman, K.S. Booksh and M.L. Myrick, "Multivariate Raman Imaging of Simulated and "Real World" Glass-Reinforced Composites" *Applied Spectroscopy*, ***50***(5), 552-557, **1996**.

(78) T.M. Hancewicz and C. Petty, "Quantitative Analysis of Vitamin A using Fourier Transform Raman Spectroscopy" *Spectrochimica Acta Part A*, ***51***,2193-2198, **1995**.

(79) N. Everall, P. Tayler, J.M. Chalmers, D. MacKerron, R. Ferwerda and J.H. van der Maas, "Study of Density and Orientation in Poly(ethylene terephthalate) using Fourier Transform Raman Spectroscopy and Multivariate Data Analysis" *Polymer*, ***35***(15), 3184-3192, **1994**.

(80) K.P.J. Williams and N.J. Everall, "Use of Micro Raman Spectroscopy for the Quantitative Determination of Polyethylene Density using Partial Least Squares Calibration" *Journal of Raman Spectroscopy*, ***26***(6), 427-433, **1995**.

(81) M.B. Seaholtz, D.D. Archibald, A. Lorber and B.R. Kowalski, "Quantitative Analysis of Liquid Fuel Mixtures with the use of Fourier Transform Near-IR Raman Spectroscopy" *Applied Spectroscopy*, ***43***(6), 1067-1072, **1989**.

(82) J.F. Aust, K.S. Booksh and M.L. Myrick, "Novel *In Situ* Probe for Monitoring Polymer Curing" *Applied Spectroscopy*, ***50***(3), 382-387, **1996**.

(83) D.R. Lombardi, C. Wang, B. Sun, A.W. Fountain III, T.J. Vickers, C.K. Mann, F.R. Reich, J.G. Douglas, B.A. Crawford and F.J. Kohlash, "Quantitative and Qualitative Analysis of Some Inorganic Compounds by Raman Spectroscopy" *Applied Spectroscopy*, ***48***(7), 875-883, **1994**.

(84) B.A. Crawford, D.A. Dodd, F.L. Kohlash and G.L. Troyer "Evaluation of Dispersive Raman Spectroscopy for Characterization of High-Level Waste Tank Samples in the Laboratory," Westinghouse Hanford Company, WHC-SD-WN-TI-580, **1993**.

(85) S.D. Brown, "Chemical Systems under Indirect Observation: Latent Properties and Chemometrics" *Applied Spectroscopy*, ***49***(12), 14A-31A, **1995**.

(86) P. Geladi and B.R. Kowalski, "Partial Least-Squares Regression: A Tutorial" *Analytica Chimica Acta*, ***185***(1), 1-17, **1986**.

(87) S.M. Haight and D.T. Schwartz, "Automated Background Removal in Line-Imaging Raman Spectroscopy" *Applied Spectroscopy*, ***51***(7), *to appear*, **1997**.

(88) T. Isaksson and B.R. Kowalski, "Piece-Wise Mulitiplicative Scatter Correction Applied to Near-Infared Diffuse Transmittance Data from Meat Products" *Applied Spectroscopy*, ***47***(6), 702-709, **1993**.

(89) J.E. Jackson and G.S. Mudholkar, "Control Proceedures for Residuals Associated with Principal Components Analysis" *Technometrics*, ***21***(3), 341-349, **1979**.

(90) R.J. Mortimer, D.R. Rosseinsky and A. Glidle, "Polyelectrochromic Prussian Blue: a Chronoamperometric Study of the Electrodeposition" *Solar Energy Materials and Solar Cells*, ***25***,211-223, **1992**.

(91) S.M. Haight and D.T. Schwartz, "*In Situ* Oxidation State Profiling of Nickel Hexacyanoferrate Derivatized Electrodes using Line-Imaging Raman Spectroscopy: I. Multivariate Calibration" *Journal of the Electrochemical Society*, ***submitted***.

(92) S. Ochs, E.W. Grabner and E. Mohler, "Optical Detection of Electron Transport in Thin Films of Prussian Blue" *Berichte der Bunsengesellschaft für Physicalische Chemie*, ***100***(5), 594-598, **1996**.

(93) D.M. Roundhill, Photochemistry and Photophysics of Metal Complexes; Plenum Press: New York, 1994, p. 72.

APPENDIX A: LINE-IMAGING RAMAN INSTRUMENT CONTROL AND IMAGE PROCESSING SOFTWARE

In this appendix a synopsis of the key software modules for control of the line-imaging Raman instrument and image processing is given. The spectroscopic and electrochemical instrumentation is controlled by a Macintosh Centris 650 computer running LabView over a GPIB interface. All software was custom written, including simultaneous multiple instrument control, data acquisition, post-collection spectral, spatial and full-image display, calibrated spectral axis, automated baseline removal, flat-field correction, image notation, noise and cosmic spike filtering, and file compression. Extensive error handling and reporting has been included in all levels of the system. Although the body of controlling and processing software is extensive, it is written in a very modular fashion to allow powerful, experiment-specific routines to be easily interfaced with the instrument in a short amount of time. All instruments are GPIB (general purpose interface bus) devices, which allow for fast, reliable data and command transfer, and are platform independent giving the instrument an additional degree of modularity. This appendix leads the reader through a typical image acquisition, highlighting the main software modules called by the user and instrument system in a top-down manner.

All Labview programs are referred to as Virtual Instruments, or VI's. They can be used interchangeably as main VI's or sub-VI's, and consist of graphical user interface (GUI) objects that either send or receive data. These GUI objects are arranged on the "front panel" of the Virtual Instrument. The main VI used to control the line-imaging Raman system is **Raman Ctrl**, and its front panel is shown in Figure A.1. All aspects of controlling the system can be accessed from this panel. The basic CCD chip definition and acquisition parameters are set by controls on the left side of the panel. The user selects the

degree of on-chip binning with the Vertical and Horizontal Line Width controls. These must be a multiple of two. Also the spectrograph entrance slitwidth, exposure time, grating, shutter enabling, laserline in use, and spectral positioning controls are located here. The system can be spectrally positioned by defining either the bluest edge, reddest edge, or center wavenumber or wavelength to be collected. Definitions composed of multiple combinations of wavelength and wavenumber settings are allowed.

On the right side of the front panel are controls and indicators concerned with other aspects of image collection. Here are found controls specifying whether the collected image should be saved, whether the spectrograph should be manually initialized, and whether image collection should be repeated continuously (useful for sample alignment). The system knows if the spectrograph has already been initialized or not and prompts the user for verification if this manual setting is does not reflect current conditions. The number of desired accumulations is set with a control in this area also. If more than one is desired, and a single spectrum has been defined on the CCD, the user has the option of storing each spectrum in the form of an image where each row is a separate accumulation. This option is activated by checking "Save as Sequence." Otherwise the sum of the accumulations is reported as a single image. For long accumulations frequently the user would like to operate the system unattended. In order to allow time to leave the imaging area before exposure begins, an initial delay timer can be set in increments of 5 seconds. After the system has been configured to collect an image, the user runs the **Raman Ctrl** VI.

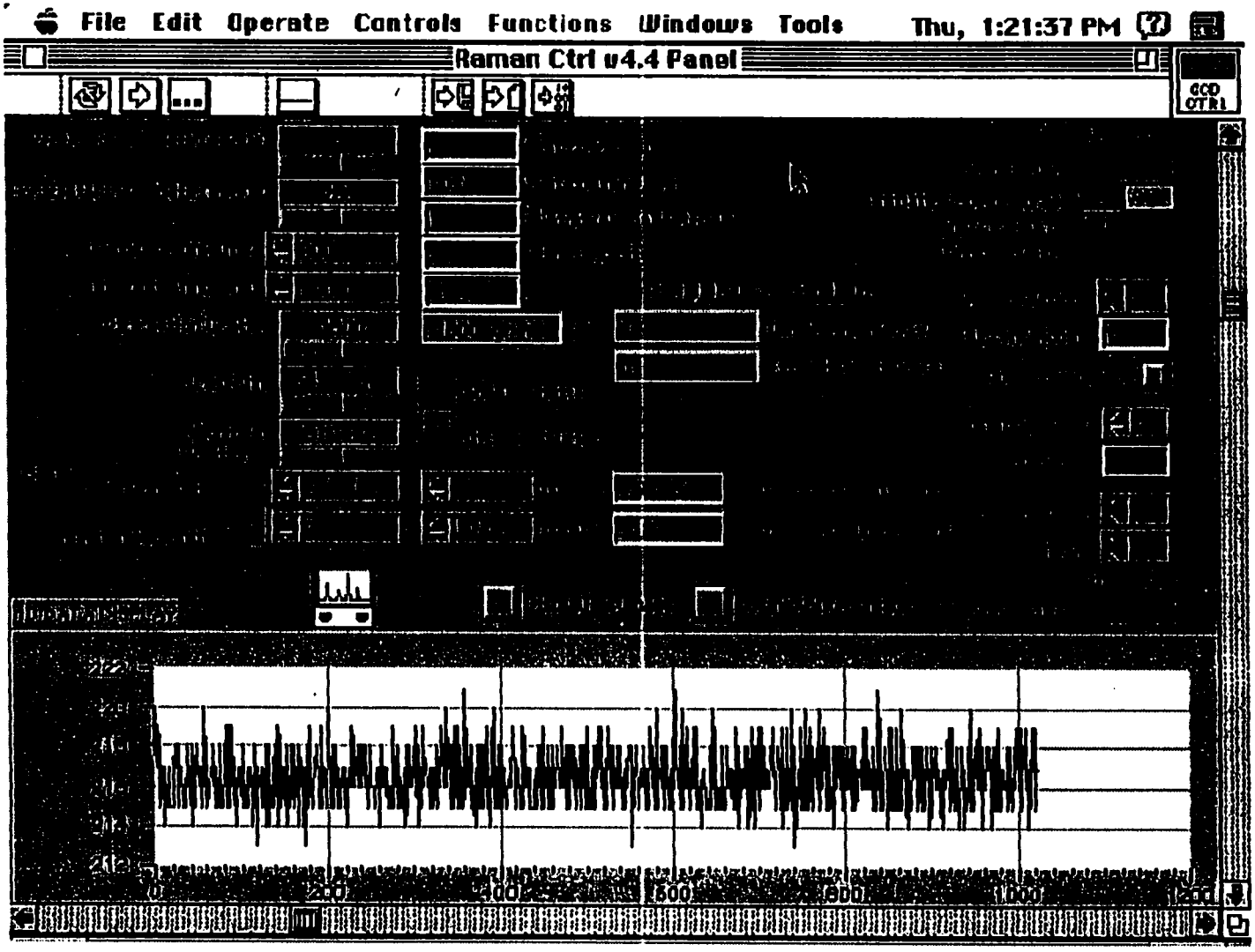

Figure A.1. Raman Ctrl VI

After **Raman Ctrl** has been launched, the system proceeds to check if anything has been altered since the last accumulation. If it has, it determines what needs to be changed. Commonly something in the spectrograph needs to be repositioned. Figure A.2 shows the VI used to control the spectrograph, **270M Controller**. this VI controls all the movements of the spectrograph. Each of the four movement options are selected to be either activated or not. If a movement is desired, the slider control is set to "yes", and the desired position or action is indicated on a nearby control. As the spectrograph performs each selected action, progress windows appear and display real-time motor positions such as shown in Figure A.3. After each selection is completed, indicator lights show that the operation has completed successfully, and control is passed back to the calling VI.

After the system has been adjusted to the selected acquisition parameters, **Raman Ctrl** communicates with the CCD controller and instructs it to acquire the image. After the image has been passed by the CCD controller to **Raman Ctrl**, a cluster of information about the image is associated with it. Figure A.4 shows this cluster data structure, which records the center wavelength, calibration number, slitwidth, laserline, grating, number of accumulations, length of exposure, date, time, image size, and space for text comments from the user or the system. There is also space allocated for future use. This information is associated with the image, so that when an image is passed to, or called from a software module, the image "identifies" itself to that module and can immediately supply the information required to process it appropriately. For example, when the user wishes to view an image, the image notifies the viewing software what the appropriate calibration is, what laserline was used, and how the spectrograph was positioned.

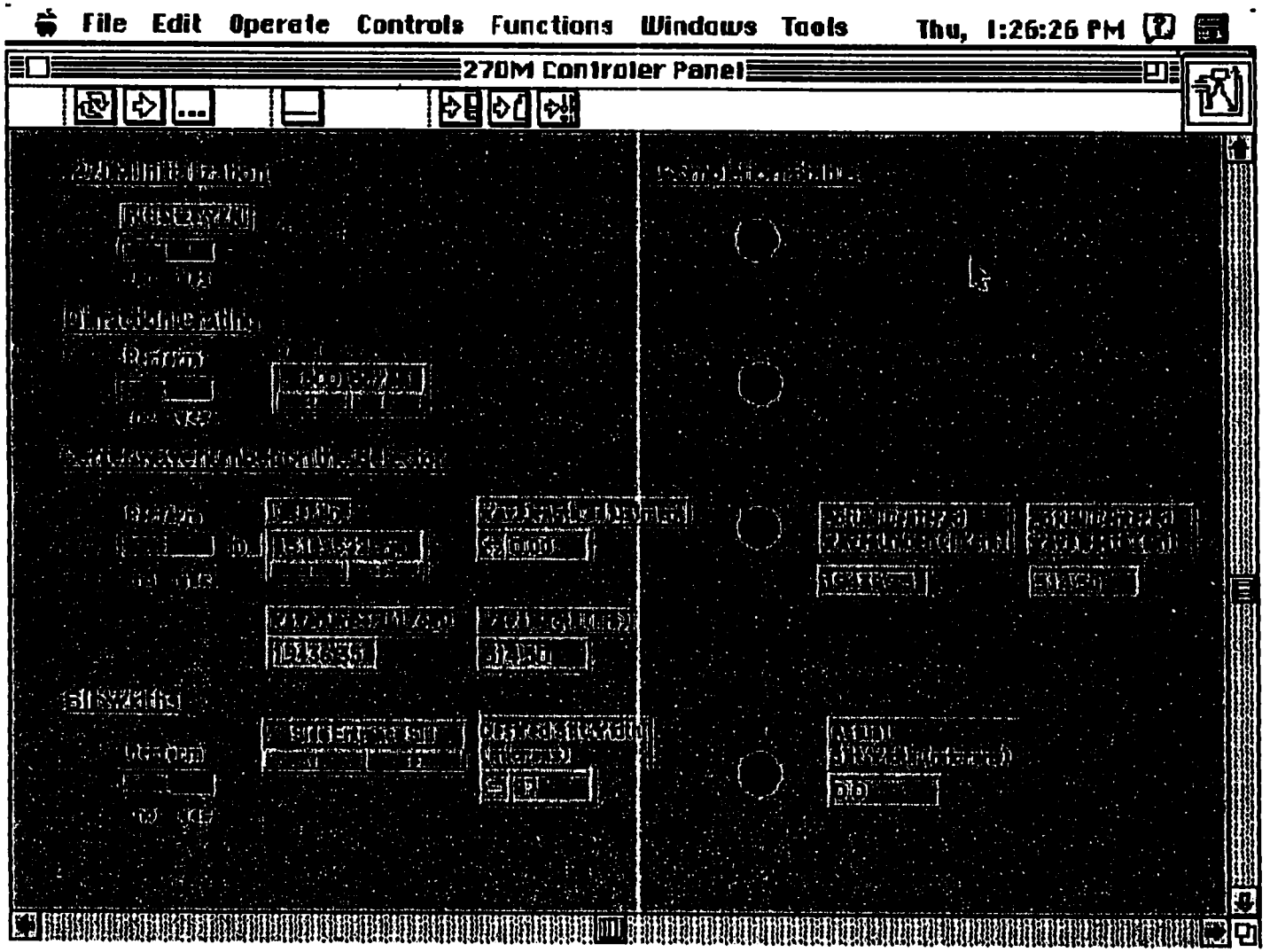

Figure A.2. 270M Controller VI

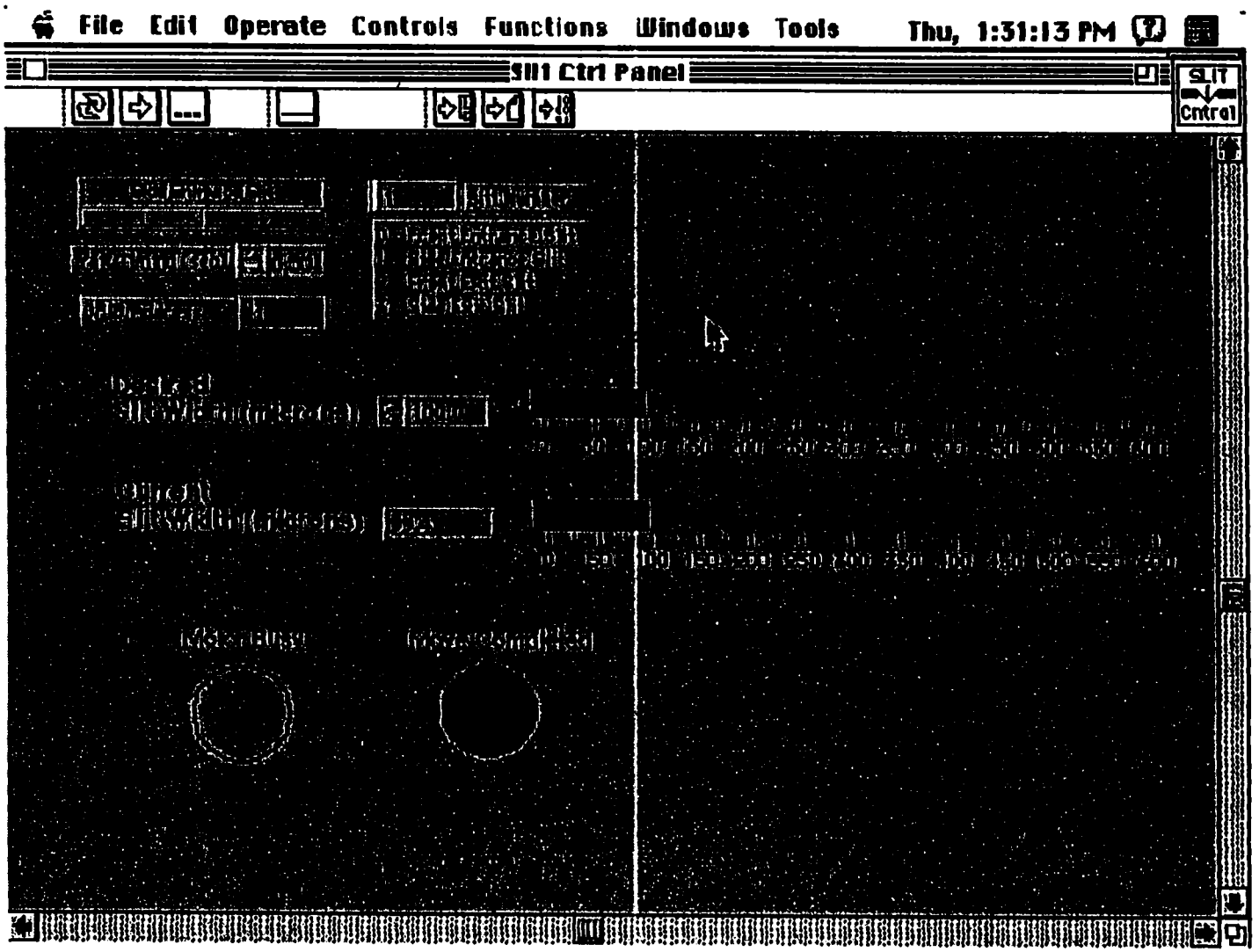

Figure A.3. Slit Ctrl VI

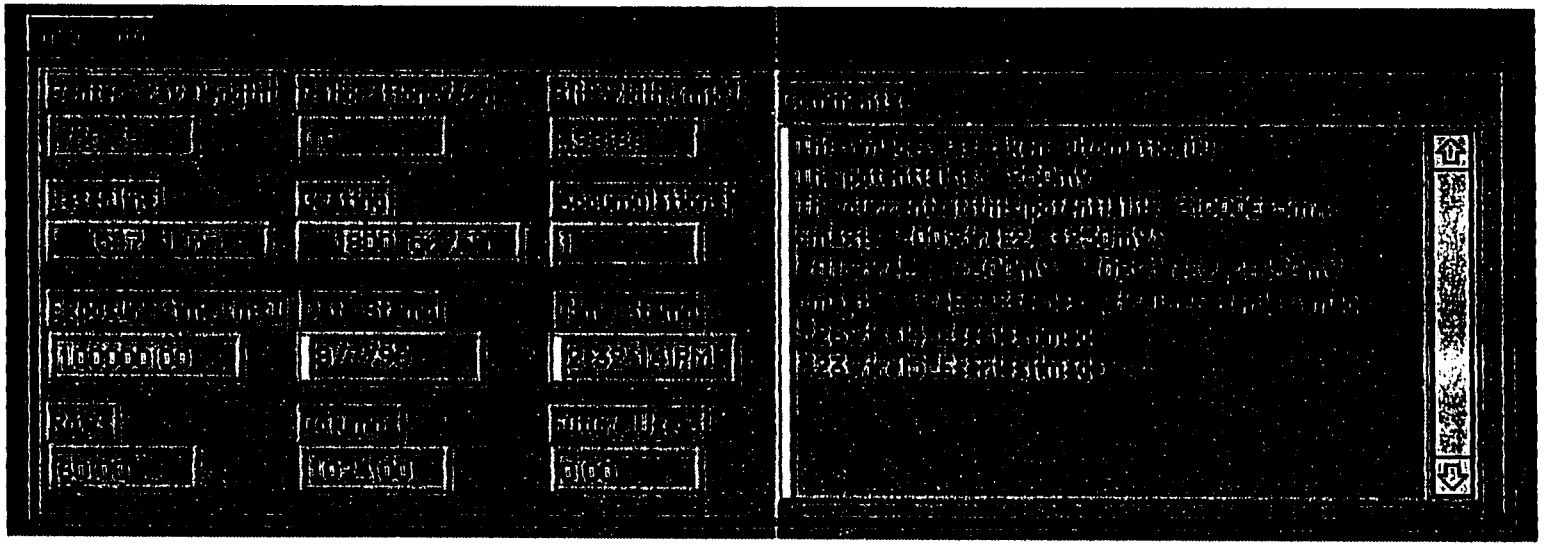

Figure A.4. File Information Cluster

After an image has been acquired and associated with its information, it is passed to the **Image Viewer** for display. This VI is shown in Figure A.5. Like most VI's in this system, **Image Viewer** can be called as a stand-alone module. In that case, rather than being passed an image, the user is prompted to select an image file through a standard dialog box. If the option is selected (control off-screen), **Image Viewer** displays a grayscale rendition of the image in a separate window. On the front panel, a spectral slice of user-defined width is displayed. The user has the option of displaying single spectral rows, or displaying the average spectrum of several rows by adjusting the binning control. The center row of the bin is selected with the nearby control. In this way, the user can opt to view an image in any manner ranging from spectrum by spectrum, to the average spectrum of the entire image.

Other controls select which axis is to be used (nm or cm^{-1}), if the displayed spectrum is to be saved to a separate tab-delimited file, and whether or not to filter out cosmic rays. Filtering is performed by a nonlinear median filter, whose rank is also directly adjustable from the front panel. Two other controls can pass the displayed spectrum to an automated background removal module, or pass the image to a module that allows the user to view spatial slices of the image.

If the spatial slice module is called, the user is taken to the front panel of **Spatial Viewer**, shown in Figure A.6. This module is very similar to **Image Viewer** in functionality. The user may view a spatial slice of an image with adjustable position and width. When fully binned (average of all spectral rows), this display shows the spatial intensity profile over the entire image. When no binning is performed, this displays the spatial intensity variation at a particular wavenumber. The displayed profile can be saved to a tab-delimited text file by pressing the "save" button.

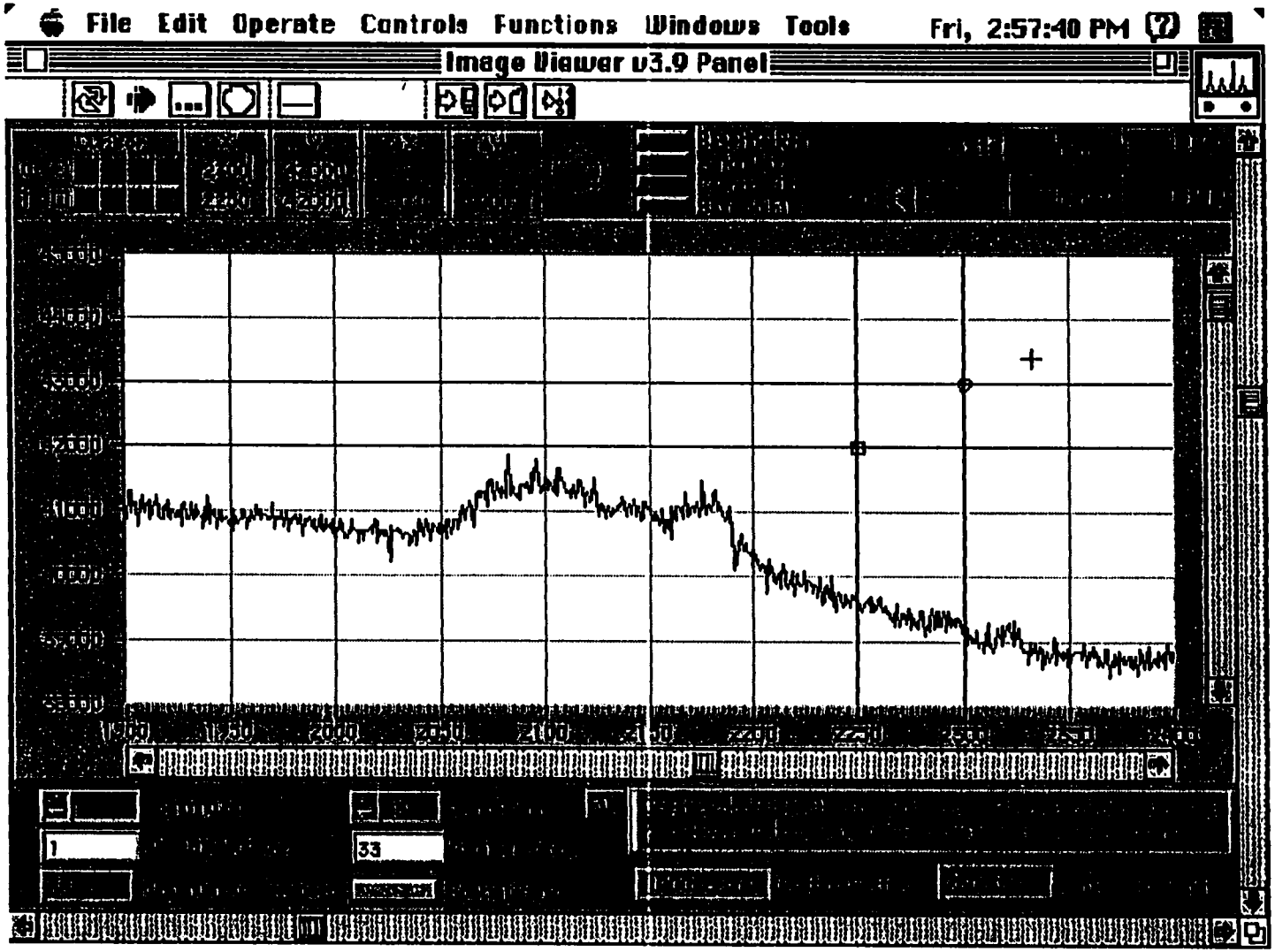

Figure A.5. Image Viewer VI

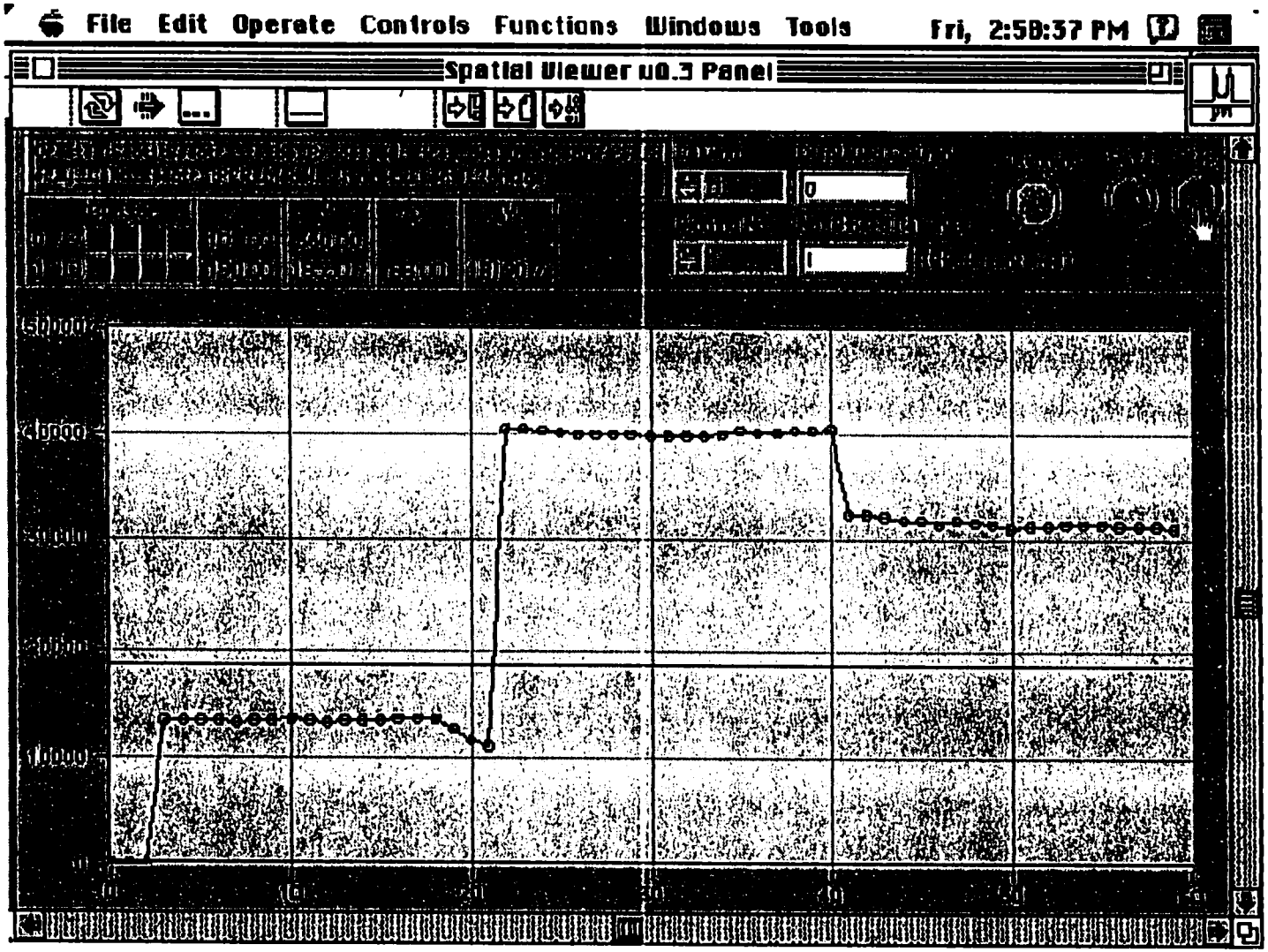

Figure A.6. Spatial Viewer VI

If the spectral background removal module is selected from the front panel of **Image Viewer**, the user is taken to a version of the **Pearson Baseline** VI, shown in Figure A.7. This routine performs background subtraction on the spectrum passed to it. It can also be used as a stand-alone module to process an entire image. After the background has been subtracted, the user may elect to accept the removal, or modify the routine parameters and run the routine again. When the user is finished using the background subtraction module, the user is taken back to **Image Viewer**. Particular background removal statistics (*e.g.* time to complete, number of iterations, number of iteration failures, etc.) are reported back to the calling VI, although **Image Viewer** does not use them.

After being returned to **Image Viewer** and viewing the image, the Run/Stop slider is pressed, which stops the VI and passes control back to the calling VI. When an image has been passed to **Image Viewer** from **Raman Ctrl**, **Raman Ctrl** regains control and prompts the user to save the image if that option has been selected. If saved, the image and the information cluster is stored to disk in a compact binary file format. At this point the process of acquiring and saving a line-image is complete.

Many other VI's exist to perform specific functions such as conversion of images to other file formats (*e.g.* unsigned 16 bit raster, Matlab workspace, SDS, tab-delimited text), running experiment specific "scripts" to automate multiple image acquisitions and control electrochemical instrumentation, and unattended post-processing of image stacks.

The front panel from the main VI used to control the PAR 273/273A potentiostat (the main electrochemical instrument used for this work) is shown in Figure A.8. This VI performs a potentiostatic sweep as defined in the "Source Curve Definition" table. Many other controllable features of the PAR 273/273A can be accessed with this VI including: choice of voltage and current ranges, IR compensation method and parameters, and types

of input to be sampled. Other features are due to the VI itself including: building/accessing a source curve library, spectral analysis, filtering, anodic-, cathodic-, and reversible-charge calculation, multiple x-axis options, and dummy cell and busy communication awareness. The sampled curves can be saved to a tab-delimited text file with or without a rich header containing all of the information shown on the front panel.

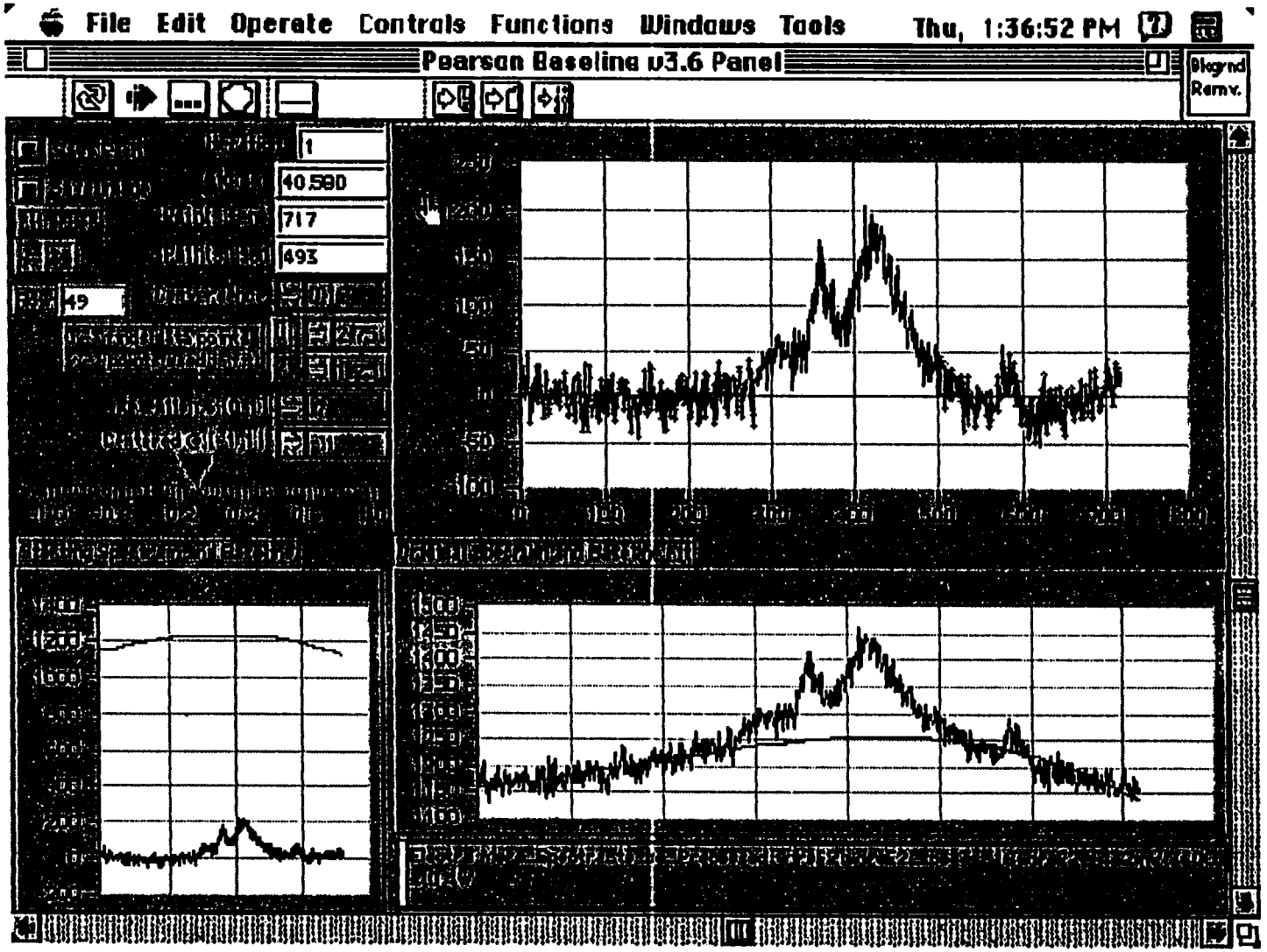

Figure A.7. Pearson Baseline VI

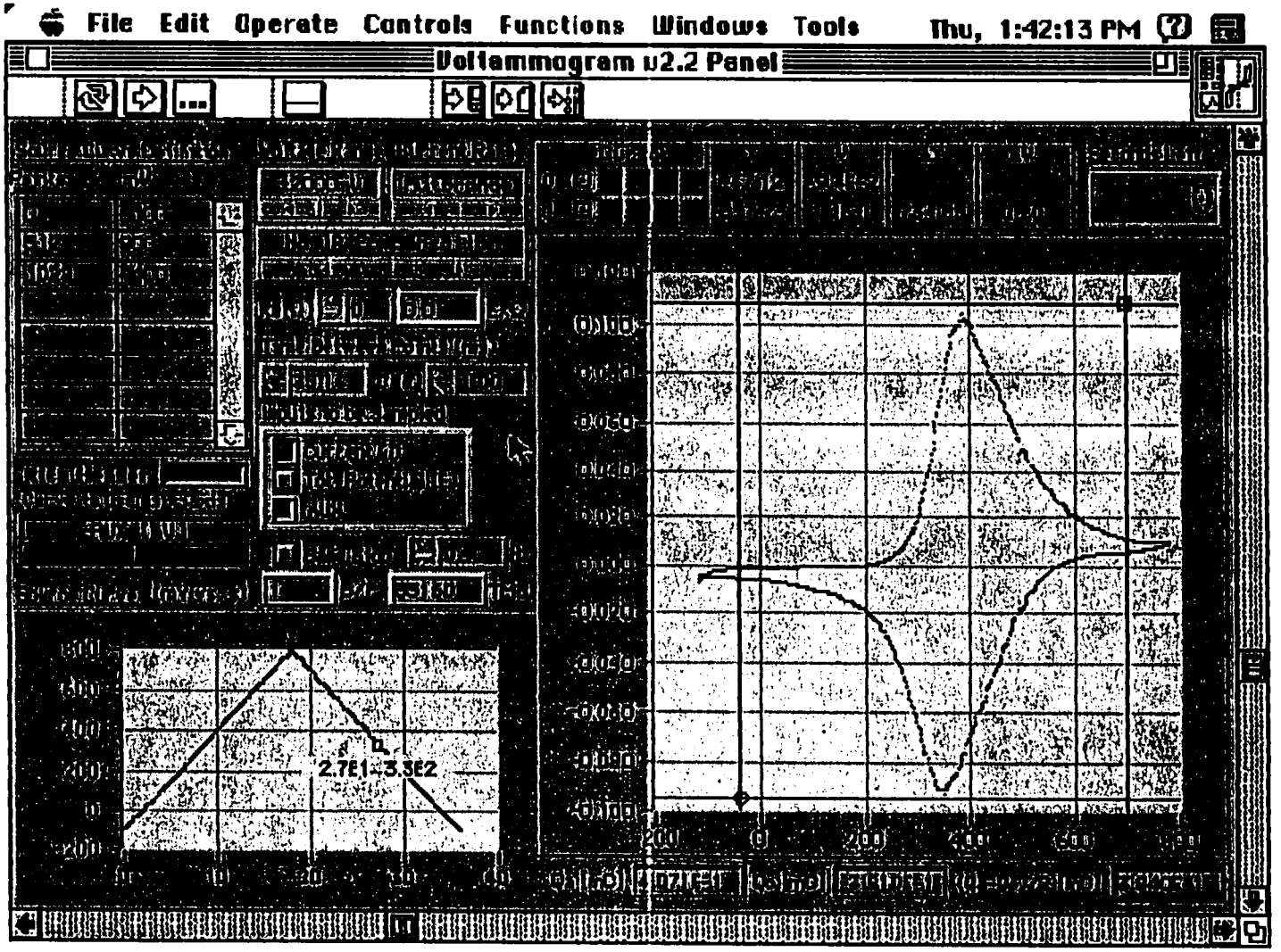

Figure A.8. Voltammogram VI

APPENDIX B: EFFECTS OF NOISE AND SPECTRAL MISALIGNMENT ON MULTIVARIATE PREDICTIONS FROM LINE-IMAGES

B.1 Introduction

Before quantitative predictions can be made from a spectrum, generally the spectrum must be preprocessed in some manner. This can include operations such as filtering, shifting, background subtraction, and scaling. Many times a collection of spectra, such as a Raman line-image, or a series of spectra resulting from experimental perturbations to a system, is to be analyzed by multivariate means. In this case, each spectrum in the collection must be preprocessed to adjust it to most resemble a common basis. This common basis can be internal, (*e.g.* the mean spectrum of the collection), or can be external (*e.g.* the mean spectrum of the calibration set). Two important features of a spectrum can affect the prediction of a multivariate model: the signal to noise ratio (S/N), and the degree of spectral misalignment. The S/N affects the prediction by influencing the ability of the spectrum to be properly scaled during preprocessing. Spectral misalignment affects the prediction by improperly matching the multivariate calibration vector (weighting coefficients) to the spectrum intensity values. This appendix explores the sensitivity of each of these factors on the multivariate PCR model described in Chapters 5 and 6.

B.2 The effect of noise on spectral preprocessing

Figure B.1 shows a representative "perfect" spectrum with various degrees of Gaussian noise added to produce spectra with various signal to noise ratios. During the preprocessing step, these typical spectra are scaled so that the signal level in each is the same. Weak, low intensity, signals are magnified so that the signal portion of their intensity levels resemble strong, clean signals, but as a consequence the noise is also

magnified. To multiply by the appropriate amount becomes increasingly difficult as the underlying signal is masked by noise.

A successful method of spectral scaling used for multivariate models suggested by Kowalski is multiplicative scatter correction (msc).[78,88] This scaling method involves a multiplicative and additive term applied to the spectrum so that it best resembles the basis spectrum in a least-squares sense. We attempted using msc with the Raman line-images described in Chapters 5 and 6, but found that the noise level in these images adversely affected msc's ability to properly scale the spectra. Predictions of fraction oxidized were consistently lower than expected. To see why this was so, an image constructed entirely of Gaussian noise with a varying rms of 1 to 10 was processed by the PCR model. (Since there is no signal, the S/N is always 0, but noise still varies by an order of magnitude). Figure B.2 shows the results of this processing. It is seen that the prediction is insensitive to these levels of noise with a constant value of x=0.6. The Q statistic is also basically constant. The multiplicative and additive factors reveal how msc is affected by the noise level. As the noise level increases, the scatter in the multiplicative factor converges to a value of 0, while the additive factor remains at a value of 1.4×10^{-3}, which is the mean intensity value of the basis spectrum. This indicates that as noise increases, msc transforms the processed spectrum into a flat line with the average intensity value of the basis spectrum.

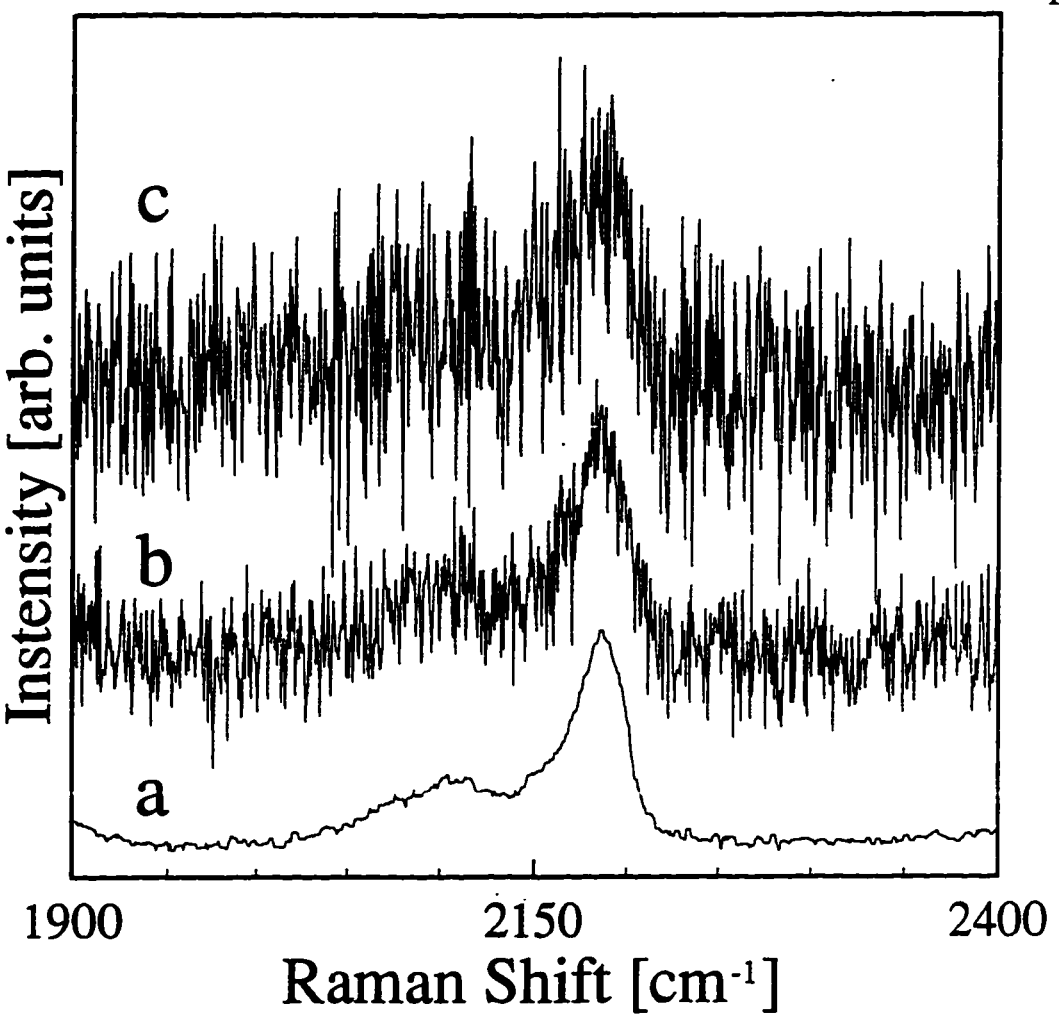

Figure B.1. Representative spectra at various signal to noise ratios. a) S/N=∞, b) S/N=2, c) S/N=1.

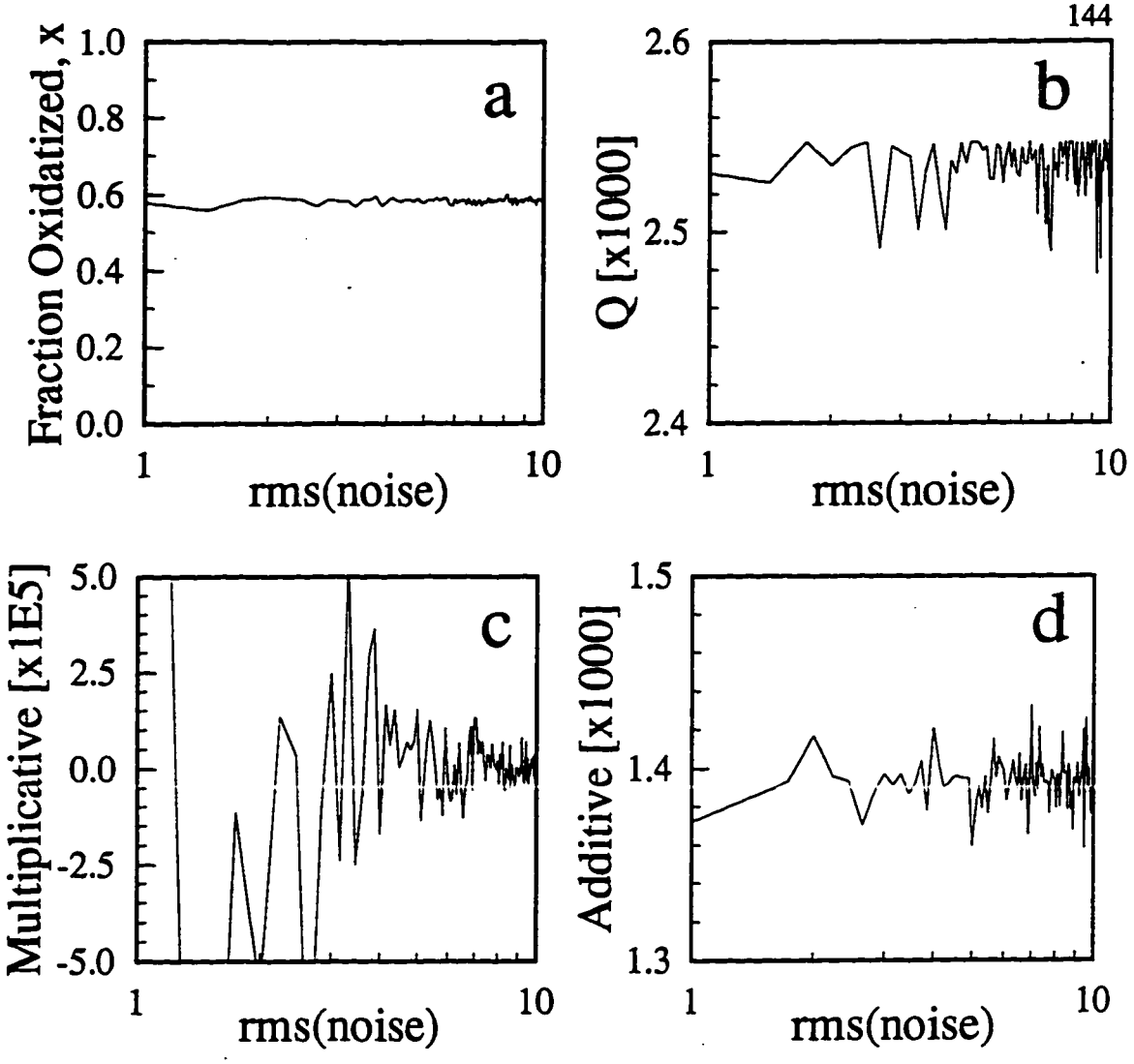

Figure B.2. PCR predictions and statistics from an image with increasing Gaussian noise using msc preprocessing.

Figure B.3 shows how this affects the prediction and statistics when a "perfect"[†] spectrum with decreasing S/N is processed using msc. The true value of the prediction is x=1.06. As the S/N decreases from 10 to 1, the prediction of the fraction oxidized falls 26%. This is due to the diminishing multiplicative factor, which falls from 1.0 to 0.4 over the same S/N range. Since only the level of noise is increasing (the signal level has not changed), the ideal response would be to maintain a multiplicative factor of 1.0 regardless of noise level. This figure clearly shows how noise masks the ability to properly scale a spectrum.

After scaling with msc, a spectrum devoid of all signal is a flat line. This flat line has a certain predicted value, and a certain Q statistic value determined by the specific multivariate model. Because of this, msc essentially puts an upper limit on the value of Q. Since the Q statistic is an important parameter in assessing the applicability of a spectrum to the model, it is desired to have Q very sensitive to deviations from the multivariate space. We see here that msc somewhat hinders this by placing an upper bound on Q.

[†] A "perfect" spectrum was contructed by taking a spectrum from the PCR model calibration set and projecting it onto the PCR space. This completely filters out all sources of variation not accounted for by the model, leaving a "perfect" spectrum. This perfect spectrum has a Q statistic of identically zero. Since the spectrum came from the calibration set, this step mostly removes noise.

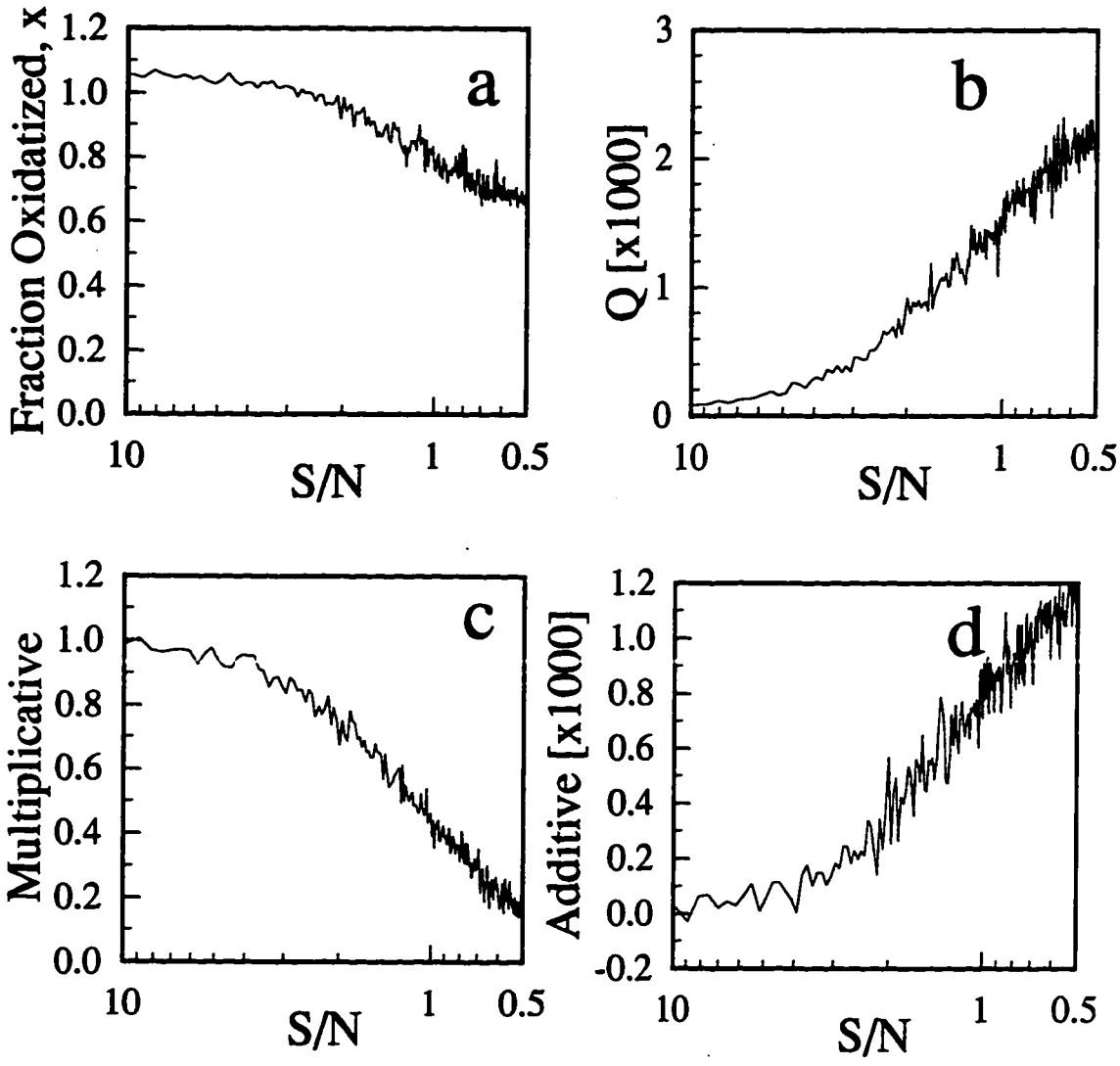

Figure B.3. PCR predictions and statistics from a "perfect" image with increasing Gaussian noise using msc preprocessing.

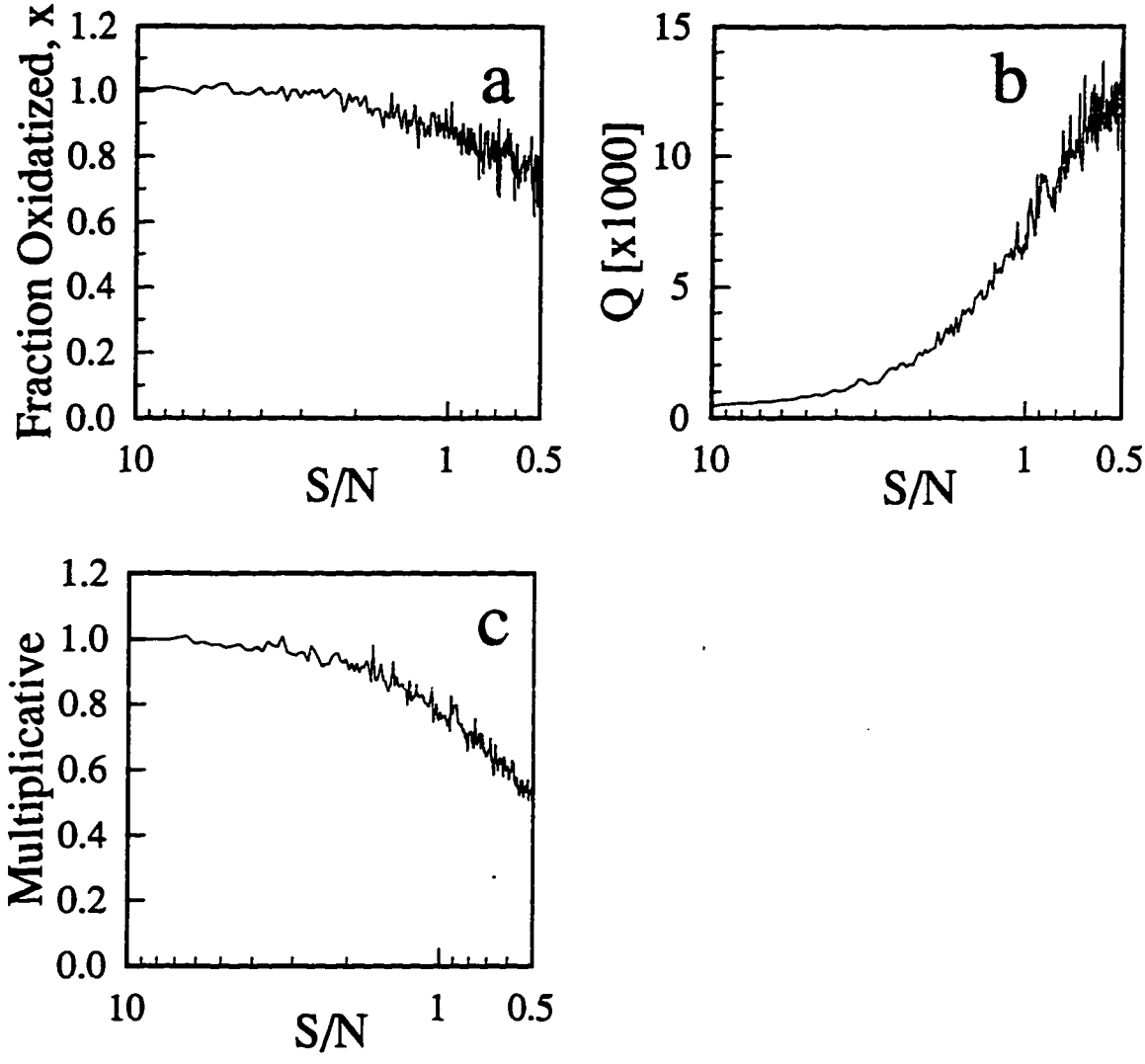

Figure B.4. PCR predictions and statistics from a "perfect" image with increasing Gaussian noise using magnitude preprocessing.

We have found that magnitude scaling is better able to properly scale the spectra from line-images presented in Chapters 5 and 6 than msc. Rather than scaling by an additive and multiplicative term, magnitude scaling scales a raw spectrum by the ratio of the vector magnitudes of the basis spectrum to the raw spectrum. Figure B.4 shows the performance of this type of scaling on a "perfect" spectrum with decreasing signal to noise. The true value of the prediction is x=1.0. Here, the fraction oxidized only falls 10% as the noise increases tenfold, much less sensitive to noise than msc. This indicates that the predictions made from spectra similar to the best and worst spectra in Figure B.1 would only differ by approximately 10% rather than 26% when scaled by msc. The multiplicative factor is also seen to fall to 0.75 for a change in S/N of 10 to 1 rather than to 0.4 when msc is used. In addition, we see that the Q statistic is much more sensitive to noise, rising well beyond the upper limit placed on it by msc.

B.3 The effect of spectral misalignment on image preprocessing.

The sensitivity of the PCR model to spectral misalignment was also investigated. Misalignment is due predominately to CCD detector array rotation relative to the spectrograph entrance slit. The entrance slit defines the spatial direction, and the grating disperses the collected light orthogonally to this direction. If the pixel grid of the CCD array is not perfectly aligned with these axes, the spectra acquired on the top edge of the array will be spectrally shifted relative to the spectra acquired on the bottom edge of the array. We are able to align the CCD array to within 4° of the spectrograph axes. This is a maximum offset of 18 pixels out of 1024 (1.7%) between the top and bottom rows.

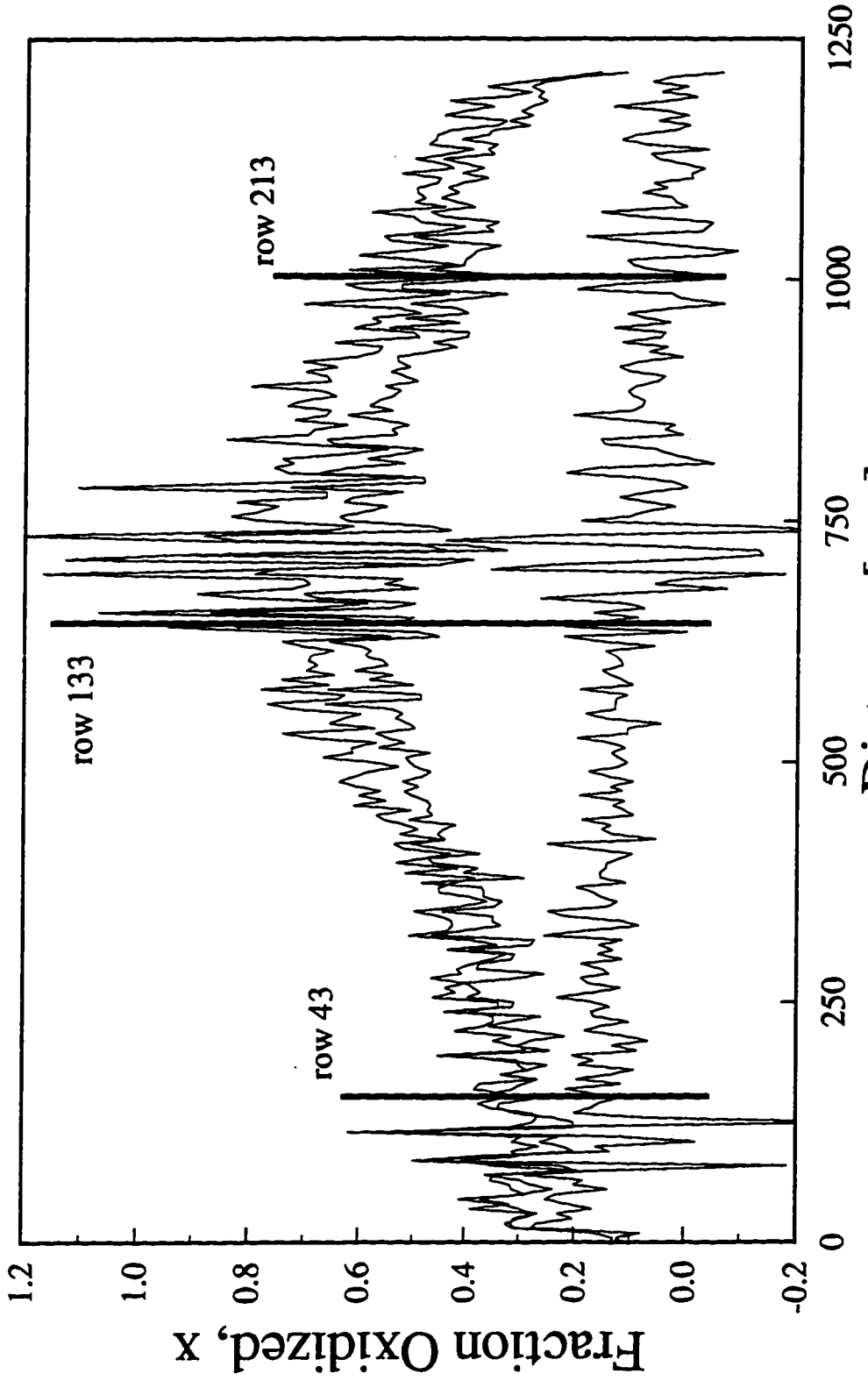

Figure B.5. Fraction oxidized profiles showing the locations of the representative spectra.

Three spectra each were taken from the line-images used to produce the fraction oxidized profiles of fresh film C shown in Chapter 6. A clean spectrum was chosen from each side of each image (rows 43 and 213), and one from the center (row 133) to produce nine spectra representing all combinations of image location (left, right, center) and oxidation state (reduced, intermediate, oxidized). Figure B.5 shows the locations of each spectral row on the fraction oxidized profiles. These profiles are not smoothed as in Chapter 6. As can be seen, these rows contain spectra from a low redox activity region (row 43), a high redox activity region (row 133), and a moderate redox activity region (row 213).

Figure B.6 shows the spectra from the oxidized film image. Similar to spectra shown in Chapter 5, the spectrum from row 43 is clearly less oxidized than the spectra from rows 133 and 213 even though the film is being held at an oxidizing potential (+801 mV). This figure also shows that the spectra have a S/N≈2, indicating that noise does not appreciably affect the scaling preprocessing. Figure B.7 shows the intermediate potential (+451 mV) image spectra. Here also row 43 appears less oxidized than the other rows, and the spectra have comparable S/N to the spectra shown in Figure B.6. Figure B.8 shows the spectra from the reduced film image (-100 mV).

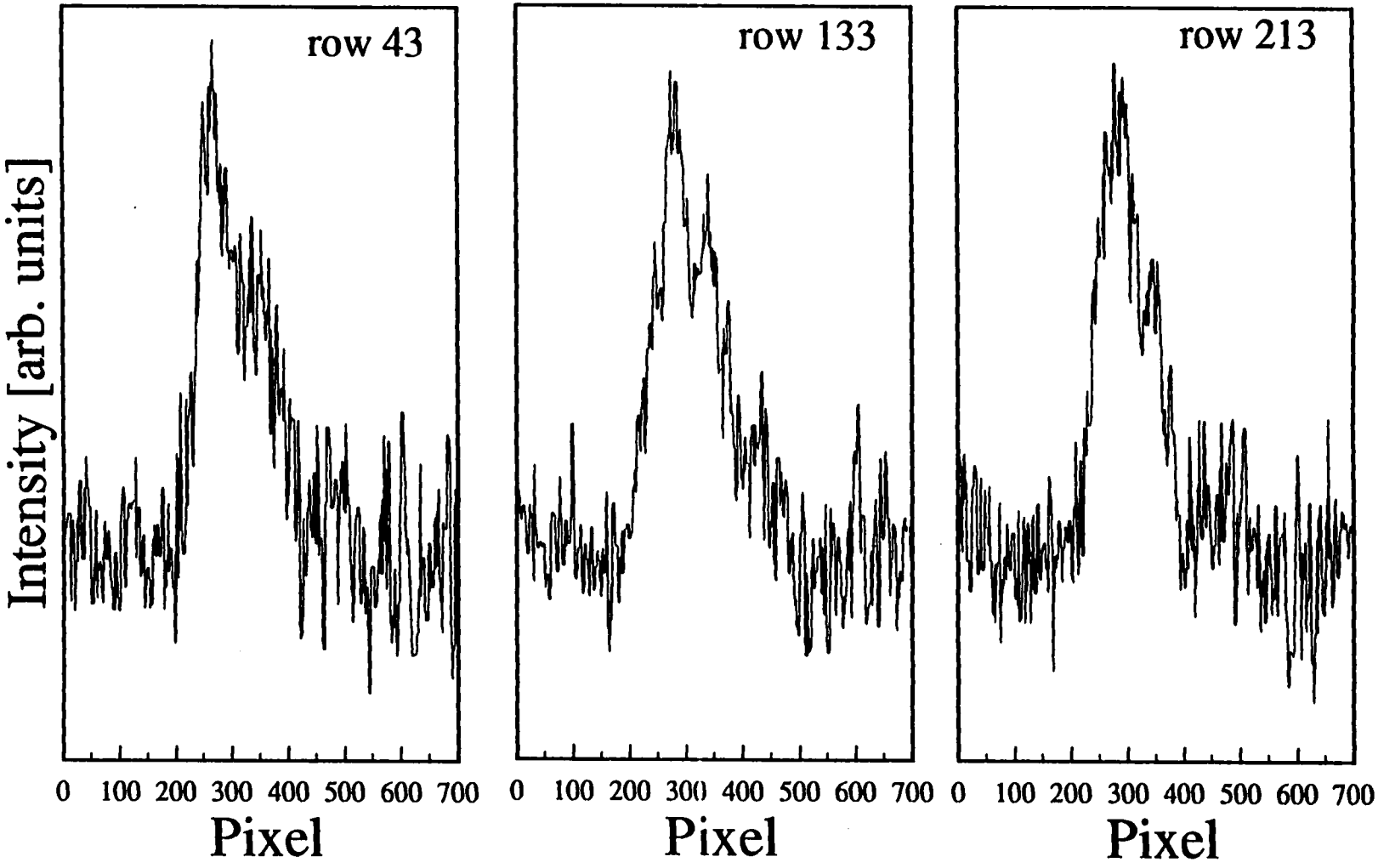

Figure B.6. Representative spectra from rows 43, 133, and 213 for the reduced film image.

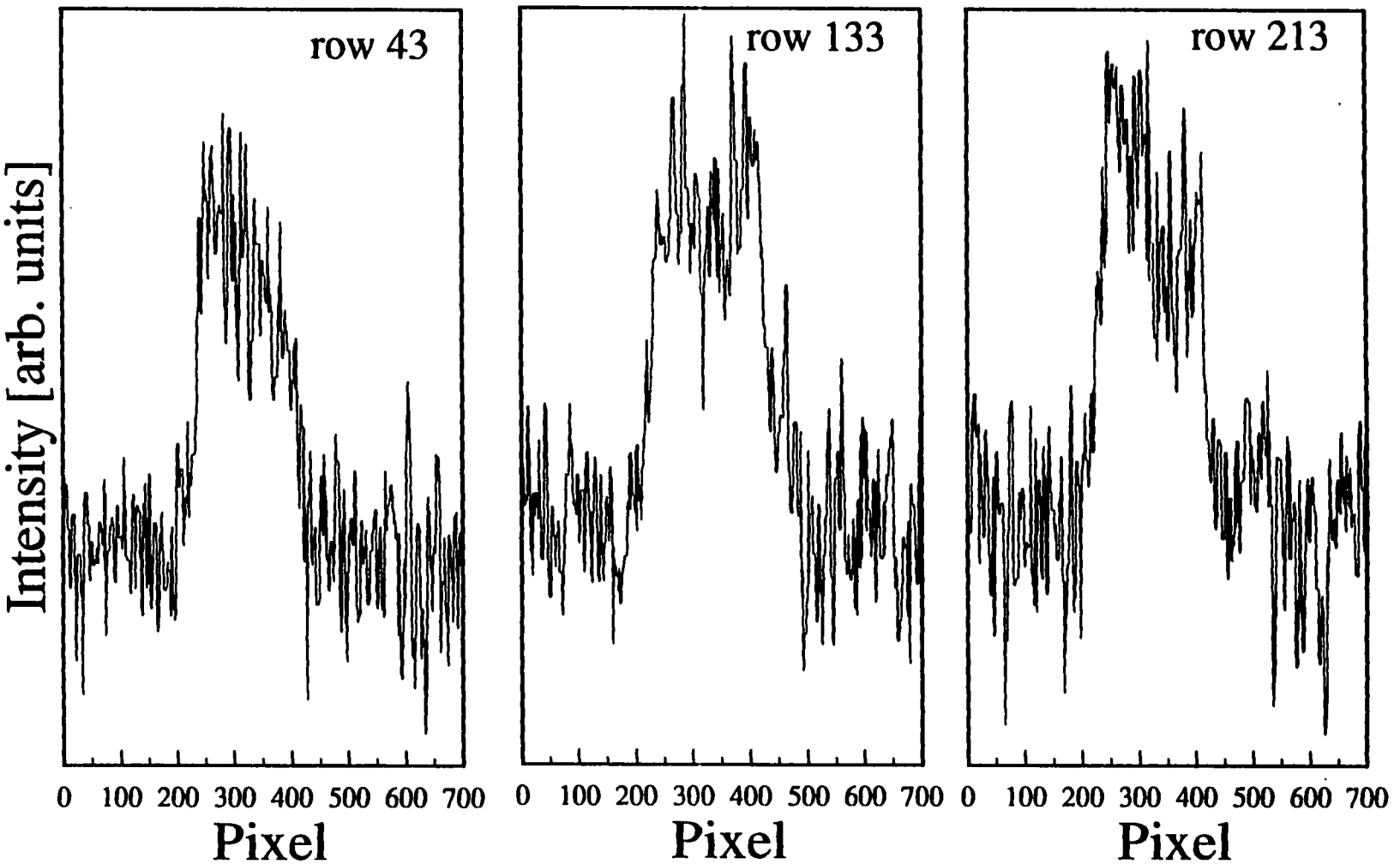

Figure B.7. Representative spectra from rows 43, 133, and 213 for the intermediate film image.

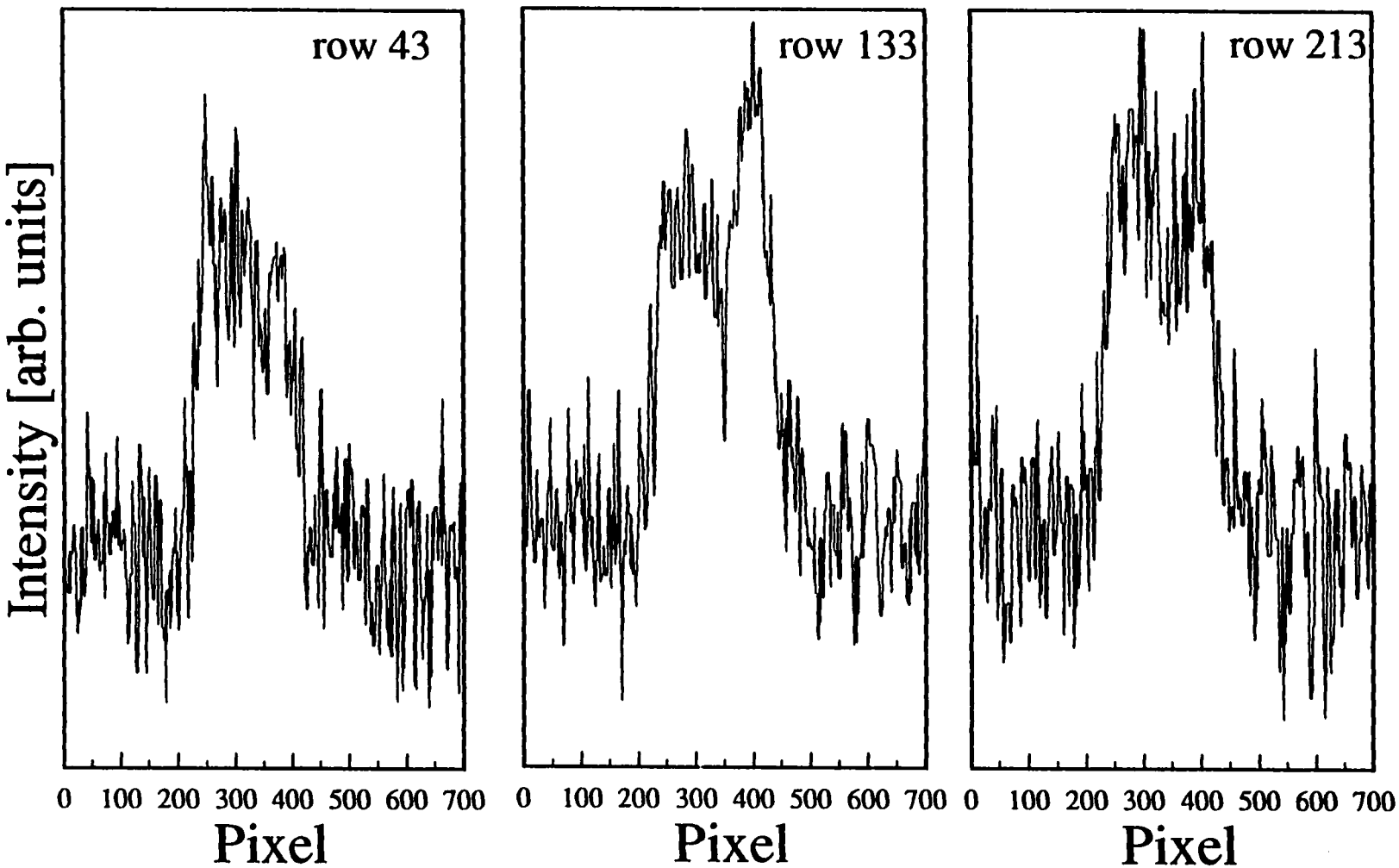

Figure B.8. Representative spectra from rows 43, 133, and 213 for the oxidized film image.

To investigate the sensitivity of spectral misalignment, each of the nine spectra was shifted ±50 pixels, and the fraction oxidized calculated with the PCR model. For a 100 pixel misalignment between row 43 and row 213 to occur, the CCD detector would have to be rotated more than 30° relative to the spectrograph axes. Therefore, this experimental pixel shift range more than encompasses any practical detector misalignment. Figure B.9 shows the predictions for each row for the reduced, intermediate, and oxidized film as a function of pixel offset. The PCR predictions are sensitive to spectral misalignment, but appreciable deviations in the predicted value do not occur until the misalignment is severe. For example, since an image will always pivot about its center, the center row (row 133) will be least affected by any CCD misalignment. From Figure B.9 it is clear that when the image is pivoted around its center (*i.e.* row 133), in both the oxidized and intermediate cases the prediction from row 213 will never match the prediction from row 133. In other words, the prediction for row 133 at zero pixel offset never equals the prediction for row 213 at any offset in both the intermediate and oxidized cases. Similarly the prediction for row 133 at zero offset never equals the prediction for row 43 at any offset in the oxidized case. In the intermediate case, row 43 must be offset by at least -35 pixels, or 21° rotation before the two predictions match.

The reduced case shows that the predictions from these spectral shapes are less sensitive to spectral misalignment in a positive direction than in the negative direction. At positive pixel displacements, the prediction of fraction oxidized is relatively constant, but at negative displacements, the sensitivity is similar to the predictions of the intermediate and oxidized images.

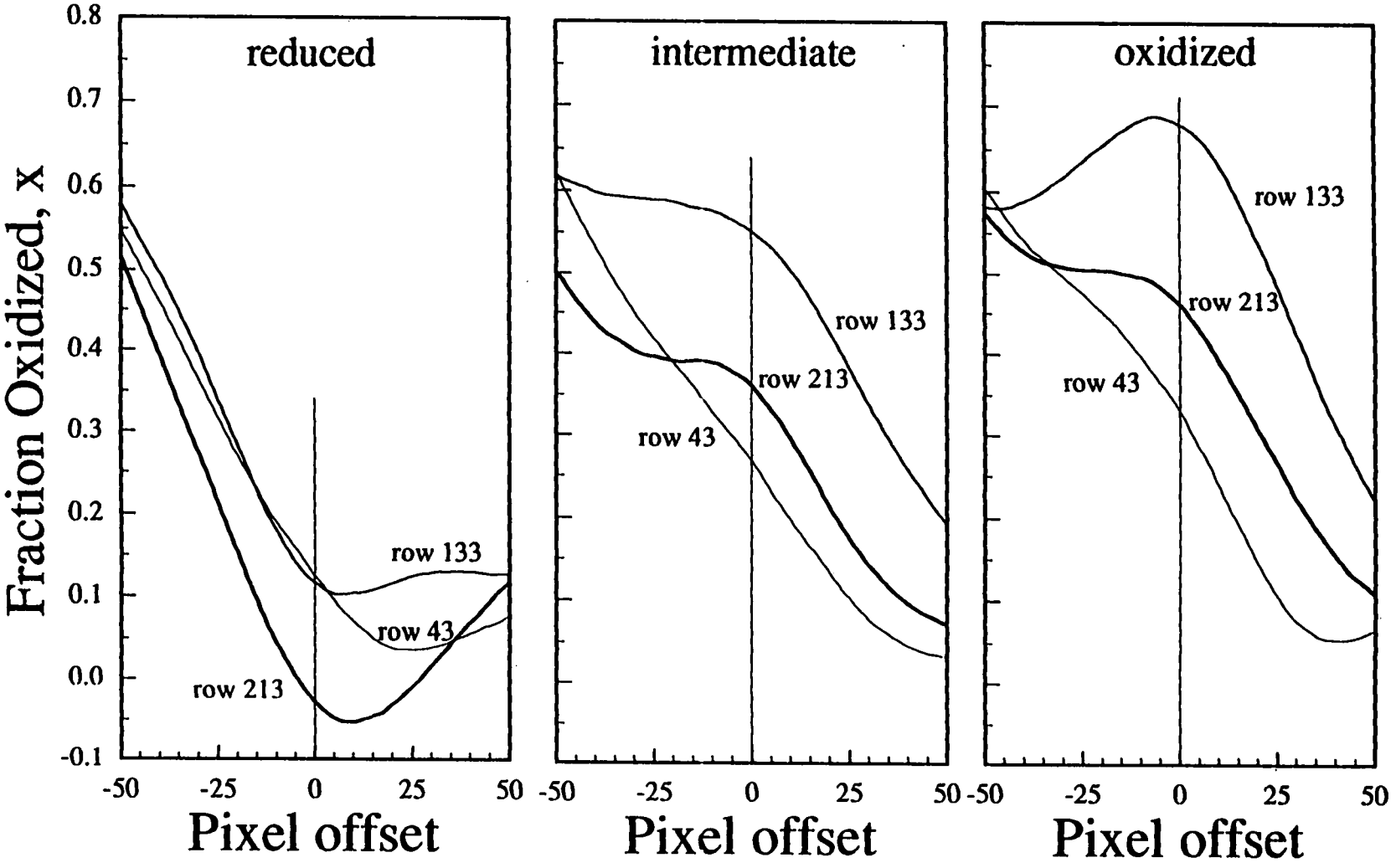

Figure B.9. Predictions of the fraction oxidized as a function of spectral pixel misalignment.

The Q statistic measures how applicable each spectrum is to the PCR model. A value of 0.0 would indicate a perfect match to the PCR model space, or that all the variation in the spectrum can be described by the PCR model. Noise, spectral misalignment, and other factors cause Q to be nonzero for real spectra. Figure B.10 shows how the Q statistic is influenced by pixel offset. The Q value for row 133 is seen to conform best (lowest Q) in all three images. Row 133 will be least affected by spectral misalignment (because it is in the center), and also has the strongest signal (because laser intensity is strongest here). The other rows have lower S/N ratios, and are seen to have larger Q values than row 133 for moderate pixel offsets. Also, Q for each row in each image goes through a minimum near zero pixel offset indicating that large pixel offsets cause the spectra to become less and less applicable to the PCR model, and that CCD misalignment is minimal.

From the above two figures, spectral misalignment as determined by Q is no more than approximately 5 pixels, which correlates to at most approximately 2% PCR prediction error due to CCD rotation.

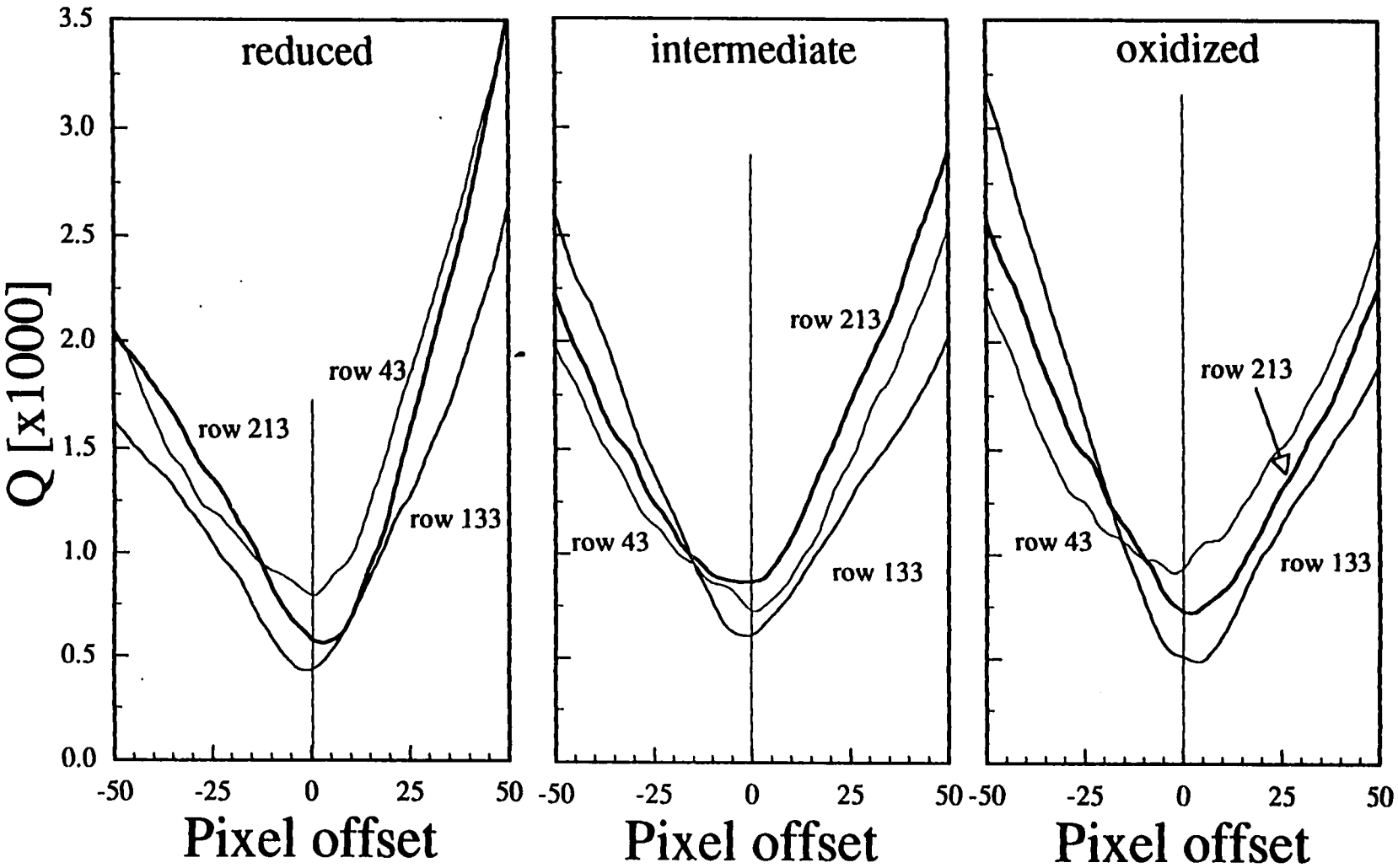

Figure B.10. Q statistic as a function of spectral pixel misalignment.

VITA

NAME Scott Michael Haight

BIRTHDATE February 15, 1969

EDUCATION

University of California, Davis
B.S., Chemical Engineering, June 1992
Minor in Philosophy

University of Washington, Seattle
Ph.D., Chemical Engineering, March 1997

PUBLICATIONS

S.M. Haight and D.T. Schwartz, "*In Situ* Oxidation State Profiling of Nickel Hexacyanoferrate Derivatized Electrodes using Line-Imaging Raman Spectroscopy: I. Multivariate Calibration" *J. Electrochem. Soc., submitted*

S.M. Haight and D.T. Schwartz, "*In Situ* Oxidation State Profiling of Nickel Hexacyanoferrate Derivatized Electrodes using Line-Imaging Raman Spectroscopy: II. Cycle Life Degradation" *J. Electrochem. Soc., submitted*

S.M. Haight and D.T. Schwartz, "Using Line-Imaging Raman Spectroscopy to Characterize Electrodeposited Materials" *J. Electrochem. Soc., submitted*

S.M. Haight and D.T. Schwartz, "Automated Image Background Removal in Line-Imaging Raman Spectroscopy" *Appl. Spec.*, **51**(7), *to appear* (1997)

S.M. Haight and D.T. Schwartz, "Design of an Imaging Raman Spectroelectrochemistry System using LabVIEW" *Intrumentation Newsletter*™, **8**(4), 1 (1996).

S.M. Haight and D.T. Schwartz, "In-Situ Imaging Raman Spectroscopy of Electrochemically-Deposited CuSCN" *J. Electrochem. Soc.*, **142**(9), L156 (1995).

M.A. Lilga, R.J. Orth, J.H. Sukamto, S.M. Haight and D.T. Schwartz, "Metal Ion Separations Using Electrically Switched Ion Exchange" *Sep. Tech., submitted*

R.S. Schwartz, S.M. Haight, D.T. Schwartz and D.C.N. Chan, "Analysis of Raman Spectroscopy for Dental Applications" *J. Dent. Res.*, **73 SI**, 223 (1994).